Università degli Studi di Udine

Dottorato di Ricerca in
Scienze dell'Ingegneria Energetica e Ambientale
XXIX Ciclo - 2017

Convection in porous media

Dr. Marco De Paoli

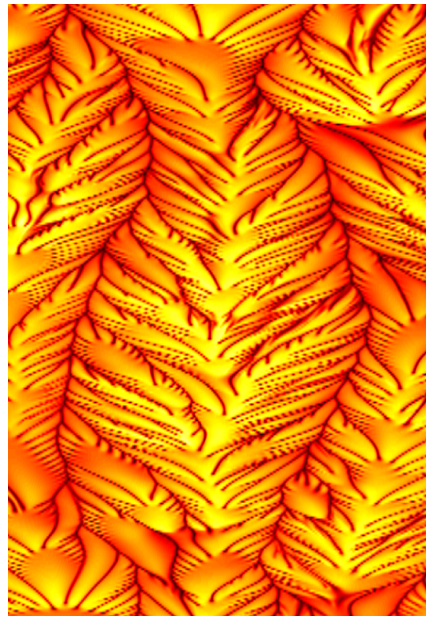

BOARD MEMBERS

Prof. Serafim KALLIADASIS	Reviewer
Prof. Matteo ICARDI	Reviewer
Prof. Cristian MARCHIOLI	Committee member
Prof. Berend VAN WACHEM	Committee member
Prof. Giuseppe PASCAZIO	Committee member
Prof. Alfredo SOLDATI	Supervisor
Dr. Francesco ZONTA	Co-Supervisor
Prof. Alessandro TROVARELLI	Doctorate Chair

Author's Web Page:
http://158.110.32.35/PEOPLE/DePaoli.html

Author's e-mail:
depaoli.marco@spes.uniud.it
marcodepaoli89@gmail.com

Author's address:
Dipartimento Politecnico di Ingegneria e Architettura
Università degli Studi di Udine
Via delle Scienze, 206
33100 Udine – Italia
mobile: +39 347 9599476
web: www2.diegm.uniud.it/diegm/

Cover picture:
Convection in porous medium at high Rayleigh number ($Ra = 5 \times 10^4$).
World lines map of the concentration field along a horizontal slice
located in the nearby of the wall, just outside of the boundary layer.

Last update:
Udine, February 2, 2017

Acknowledgments

I would like to thank my supervisor, Alfredo Soldati, for the opportunity he gave me and my co-supervisor, Francesco Zonta, for his constant support and ideas over the last three years. I will always be grateful to Cristian, Marina, Giuseppe, Luca and all my colleagues of the Lab, for their continual support and the many useful discussions.

Last (but by no means least) I would particularly like to thank my family and Anna, for their invaluable help and support. This thesis is dedicated to them.

Abstract

Convection in porous media occurs in a number of industrial and geological applications, and has important fundamental features related to the physics of buoyancy drive flows. In recent years, this phenomenon has received renovated attention for the implications it can bear in carbon dioxide sequestration strategies. In this work convective flows in fluid satured porous layers are investigated. With the aid of direct numerical simulations, the effects of anisotropic permeability and fluids miscibility are studied. Rayleigh-Bénard and Rayleigh-Taylor instabilities, which represent the archetypal problems for buoyancy driven flows, have been chosen as conceptual configurations for these investigations.

First, the influence of anisotropic porous media on solute dissolution is considered. It is shown here that modifications of the flow topology in a Rayleigh-Bénard configuration are linked to the dissolution rate (Nusselt number). Based on these findings, a generalization of a theoretical model, originally developed to describe the shutdown of convection in isotropic porous media, has been proposed. Results obtained applying this model show a remarkable enhancement of the dissolution rate due to anisotropy. Then a domain closed with respect to outgoing fluxes has been considered and the effect of the porous layer anisotropy on the flow evolution is studied, from onset to shutdown. Moreover, a theoretical model for the prediction of the shutdown time and a parametrization for the dissolution flux are proposed. These analyses, supported by their application to multiscale models, confirm the positive effect of anisotropy on carbon dioxide dissolution in saline aquifers.

Second, the influence of fluid miscibility has been considered by investigating Rayleigh-Taylor instability in isotropic porous media. The flow is mainly analysed examining two observables: mixing length and Nusselt number. Initially governed by diffusion, the system soon becomes nonlinear, and makes prediction on the plume dynamics hard to obtain. Based on the observations of the flow features, a regime classification is provided, in which the Rayleigh number effect on the flow evolution is accounted for. Moreover, for the first time the role of boundaries on the plume dynamics is taken into account: this is an important aspect since present results show that the averaged vertical plume velocity depends on the domain height. Finally, the behaviour of two immiscible fluids in a Rayleigh-Taylor configuration in considered, provided that carbon dioxide is only partially miscible into the surrounding fluid. To mimic the behaviour of such a complex system, a new model based on a diffuse interface approach (Cahn-Hilliard) is derived. The pattern of activity of these immiscible fluids is compared with

the results obtained for the miscible counterpart. Surprisingly, the asymptotic scalings found for the evolution of some relevant quantities are the same.

Contents

List of Figures

Introduction

1 Introduction

Solute convection in porous media has important fundamental features and may also bear implications for geological Carbon Dioxide (CO_2) sequestration processes. With the aid of direct numerical simulations, we examine the role of convection on CO_2 dissolution in a fluid satured porous layer.

1.1 Motivation

Global energy consumption has doubled in the last forty years, and there is no trend to drop. A major proportion of this consumption (80%) comes from the combustion of fossil fuels, with 32 GT per year of carbon dioxide (Huppert and Neufeld, 2014). Such emissions have led to a corresponding increase of CO_2 concentration in the atmosphere, likely responsible for the concomitant global average temperature rise (greenhouse effect). With this trend showing no sign of change, remedy to this global problem is still a debated question, and large-scale injection and storage is proposed to offset anthropogenic emissions and mitigate climate change.

Many aspects of the consequent flow cause fundamental fluid mechanical problems. The rise and spread of the buoyant CO_2 plume beneath an overlying impermeable layer is a problem know as gravity current, with the unwanted possibility of leakage through fractures of this impermeable layer. Leakage is very undesirable for efficient long term storage and also for public perception of risk, even though no accidents have been registered at existing sites. Fortunately, long term trapping mechanisms exist.

1.2 Trapping mechanisms

Carbon dioxide is captured from a point source, e.g. a power plant, and piped into a depth of approximately 1000 m below the surface of the earth. CO_2 injection should take place at a depth of at least 750-800 m to ensure that the carbon dioxide enters the formation in supercritical or liquid state of

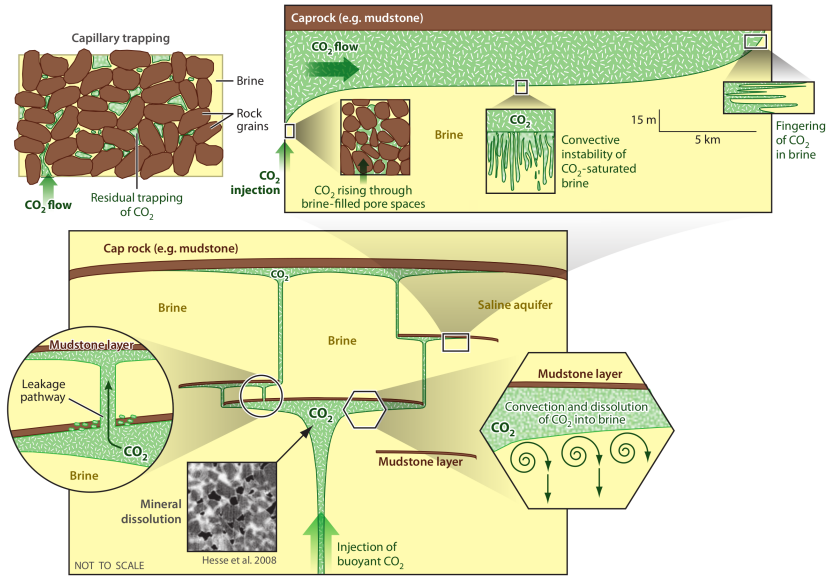

FIGURE 1.1 – Schematic representation of the trapping mechanisms occurring in a saline aquifer. Several trapping mechanisms are represented: capillary trapping (top left panel), mineral dissolution (main panel) and convective dissolution (main and top right panels). The leackage through a fractured layer is also represented (main panel). Courtesy of Huppert and Neufeld (2014).

aggregation. The maximum injection depth is usually dictated by economic considerations: the deeper the injection, the higher the drilling costs.

When CO_2 enters the storage formation, at pressure and temperature conditions there, the carbon dioxide is supercritical, i.e. it has a very high density compared with gaseous CO_2. Nevertheless, the density of the saline formation fluid (brine) is higher, causing the CO_2 to migrate upwards. For this reason, it is necessary to have a confining layer above the storage formation to stop the CO_2 from this upward migration. This layer, usually called cap-rock, needs to have a significantly lower permeability than the storage formation. Moreover, it should not have open fractures or faults which might provide vertical pathways for the carbon dioxide. If the CO_2 migrates through the cap-rock it will rise further towards the surface and finally encounter conditions in which it will turn into gaseous CO_2. Then, the density difference to the resident brine is much higher and the gaseous CO_2 will reach the surface of the earth quickly. The injection process and the subsequent dynamics are represented in Fig. 1.1. The storage formation for long-term CO_2 sequestration should have a large amount of available pore space and, as mentioned above, a sealing cap-rock. Geological formation suitable to this purpose are exploited gas and oil reservoirs or brine

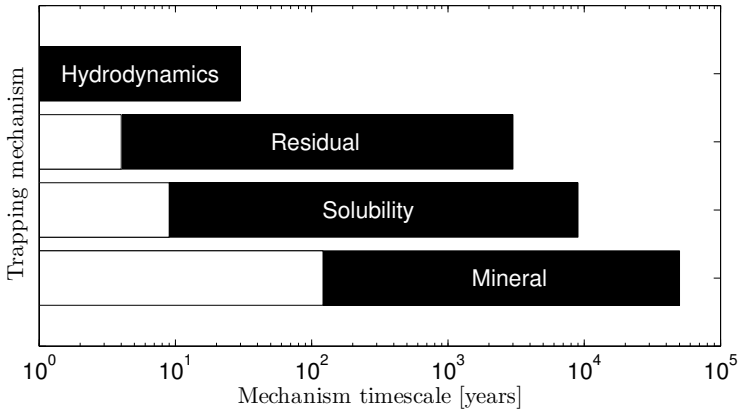

FIGURE 1.2 – Predominant trapping mechanisms (black bars) and their estimated time scales. Data from Bielinski (2007).

acquifers, and in this work we focused on latter. When carbon dioxide is sequestered in saline aquifers, several trapping mechanisms may lead to a secure long-term storage:

- hydrodynamic trapping: as mentioned above, the low-permeability layer avoids the CO_2 from rising upwards. This leads to the storage mechanism called hydrodynamic or stratigraphic trapping. Note that the cap-rock should lie horizontally or even form an inclined wall to ensure that the CO_2 cannot escape laterally, and both the configurations can be found in literature. In this configuration, the rising CO_2-current is analysed, and this flow is named *gravity currents*, because driven by the buoyancy due to the existing density difference between CO_2 and pure brine.

- Residual fluid trapping: migrating in the subsurface, the CO_2 plume leaves a trace of residual saturation, i.e. a certain portion of the pore is filled with CO_2 that no longer moves. Therefore, CO_2 that is stored by residual fluid trapping will stay in the formation for long periods of time.

- Solubility trapping: as the carbon dioxide flows in the subsurface, it dissolves in the brine which initially fills the pores of the storage formation. Dissolved CO_2 does not flow upwards because of density differences and it can remain in the formation for very long times.

- Mineral trapping: depending on the properties of brine and rock, the CO_2 reacts with the formation and forms minerals. Most of these geochemical reactions take place slowly within a time frame of decades or centuries. If minerals have formed and the system CO_2-brine-rock

has equilibrated, CO_2 is bounded for long periods of time in mineral trapping.

The variety and the time scales of the dissolution processes involved make overall predictions hard to obtain. The estimated lifetimes of the trapping mechanisms are summed up in Fig. 1.2, where the difference between the hydrodynamic and the mineral dissolution trapping mechanism is, for instance, of four orders of magnitude. A possible solution consists in to split the trapping process in sub-problems, easier to study and that can be modelled and incorporated in large-scale models. Such large-scale models can be implemented and adapted to the geometry of each reservoir. In order to do this, a clear understanding of each single process is required.

In this study, we will investigate the solubility trapping mechanism. The fundamental aspect of this mechanism is that CO_2, which is lighter than brine when pure, is partially soluble in brine (3% in weight) and forms a heavier resulting solute that flows downward. It is crucial to evaluate adequately the vertical mass flux of CO_2 because this is the macroscopic parameter that determines the dissolution rate to adopt in large-scale models. Prediction of this downward flow is, however, made complex by a characteristic instability: the heavier layer of CO_2-rich brine becomes unstable and gives rise to the formation of finger-like structures. Such instabilities (named fingers or plumes) make the process of CO_2 sinking much more efficient but also much harder to predict.

1.3 Object of the thesis

In this work, the effect of convective dissolution on the solubility trapping mechanism is investigated. Mass flux of CO_2 is controlled by the dynamics of individual fingers, which in turn is governed by the interplay between the diffusion of CO_2 across the finger interface and the forces due to buoyancy. For typical values of the parameters characterizing a real geological formation, the problem becomes multiscale with correspondingly high computational costs required for the purpose of getting accurate solutions.

In this work, high-resolved direct numerical simulations are used to analyse the dynamics of CO_2-brine mixtures into deep saline aquifers. We proposed some analytical and phenomenological models, based on the data obtained from our computational analysis, in order to describe the evolution of the system in different flow configurations and different miscibility conditions.

1.3.1 Layout of the thesis

This thesis is organised as follows. We consider two classical flow configurations: the Rayleigh-Bénard and the Rayleigh-Taylor instabilities, respectively studied in Parts I and II, which represent the archetypal problems

for buoyancy driven flows. A schematic representation of the organisation of the thesis is illustrated in Fig. 1.3.

In Part I, the effect of porous medium permeability on the solute dissolution rate is considered. The dissolution process is modelled through a conservative equation for the solute (advection-diffusion approach). In Chap. 3, we will investigate the effect of anisotropy on the CO_2 dissolution rate. With an accurate analysis of the flow topology modifications, we propose a generalization of a theoretical box-model, originally developed for the description of the shutdown of convection in isotropic porous media. In Chap. 4, we will consider a different lower boundary condition, i.e. the fluid is injected from above but the domain bottom is impermeable to fluid and solute flux. This is a more representative description of the dissolution process in geological formations. With this conceptual set up, we will in-

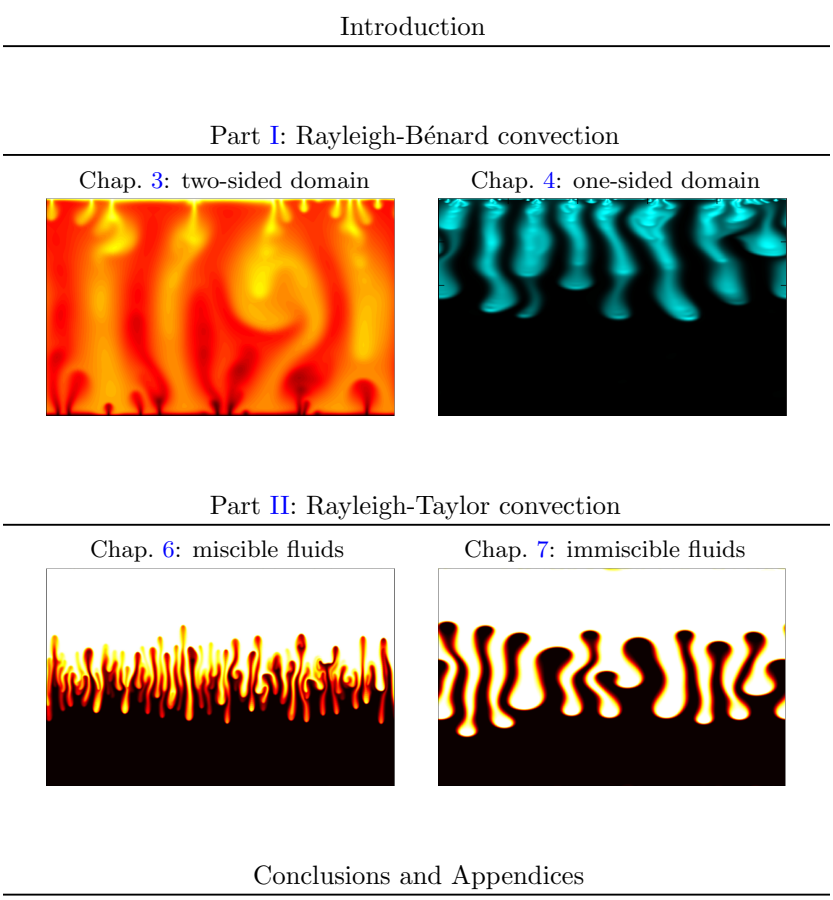

FIGURE 1.3 – Diagram showing the layout of the thesis.

vestigate the effect of anisotropy on onset, development and shutdown of convection. We provide a parametrization for the dissolution flux, and we will employ these results in a large-scale model, where the dissolution rate previously determined represents a boundary value for the large, buoyant CO_2 current.

In Part II, we consider a Rayleigh-Taylor configuration, and the effects of miscibility are investigated. In Chap. 6, using the same approach proposed in Part I, we will characterize the evolution of a Rayleigh-Taylor convection in isotropic porous media. We observed that this system is strongly connected with the correspondent Rayleigh-Bénard configuration, and the similarities are highlighted. In Chap. 7, the fluids are considered immiscible. Indeed, CO_2 is only partially miscible in brine, and a fully miscible approach may be not satisfying. A new model is derived in order to describe in a thermodynamically consistent way the evolution of such a complex system. This model is based on the diffuse interface approach (Cahn-Hilliard equation). The evolution of these immiscible fluids is compared with the results obtained in the miscible case.

Finally, we will draw conclusion and outline future developments. Furthermore, details on the numerical schemes and on the computational approach adopted will be reported.

I

Rayleigh-Bénard convection

2

Introduction to Rayleigh-Bénard convection in porous media

Solute convection in anisotropic porous media has important fundamental features and may also bear implications for geological CO_2 sequestration processes. Indeed, geological formations identified as possible sequestration sites are often made of sedimentary rocks, which derive from the deposition of subsequent layers. Due to this peculiar formation process, the permeability field associated with the porous site results anisotropic.

The dissolution dynamics, such as onset of convection, steady dissolution rate and shutdown of convection, are strongly influenced by this characteristic anisotropy.

2.1 Rayleigh-Bénard configuration

When a positive top-to-bottom density difference drives the flow between two horizontal walls, the system is identified as a Rayleigh-Bénard convection (or two-sided configuration), which represents a suitable model for the characterization of the dissolution efficiency. In the frame of porous media, the governing parameter is the Rayleigh-Darcy number, which measures the relative importance of advection compared to diffusion. This problem received renovated attention due to the application to geological CO_2 sequestration processes. Many studies are available at low Rayleigh-Darcy numbers or for isotropic porous media. Unfortunately, most of the geological formations identified as possible sequestration sites are anisotropic and characterized by high Rayleigh-Darcy numbers.

However, a more physical representation prescribes the so-called one-sided configuration. The dense solute injected from the top boundary, is driven downwards by gravity and follows a complex time-dependent dynamics. The process of solute dissolution, which is initially controlled by

diffusion, becomes dominated by convection as soon as viscous fingers appear, grow and interact. The dense solute finally reaches the bottom wall where, due to the prescribed impermeable boundary, it starts filling the domain so to enter the shutdown stage, where convection is inhibited.

With the aid of direct numerical simulations, we examine the role of anisotropic permeability on the distribution of solutal concentration in fluid satured porous medium, both in two- and one-sided configurations.

2.2 Reference Element Volume approach

Consider an ideal, fully satured porous layer, characterized by uniform permeability and porosity. If we assume incompressible and inertialess flow, the averaged velocity field is given by the Darcy law. In other words, the Darcy velocity, which is the fluid velocity multiplied by the porosity, is proportional to the pressure gradient. In this work we will refer to the Darcy velocity simply by saying velocity.

The adoption of the Darcy law rather the classical Navier-Stokes equation is essentially motivated by the computational resources nowadays available. Indeed, if we consider the porous medium as a matrix of spheres having, in general, different sizes and random distribution, the fully resolved direct numerical simulation of the flow around these spheres will not be affordable. The situation is represented in Fig. 2.1. Typical domain size (H^*) for geologically-relevant problem is of the order of tens of meters, whereas the porous size of the order of 10^{-3} m or less. Using the classical Navier-

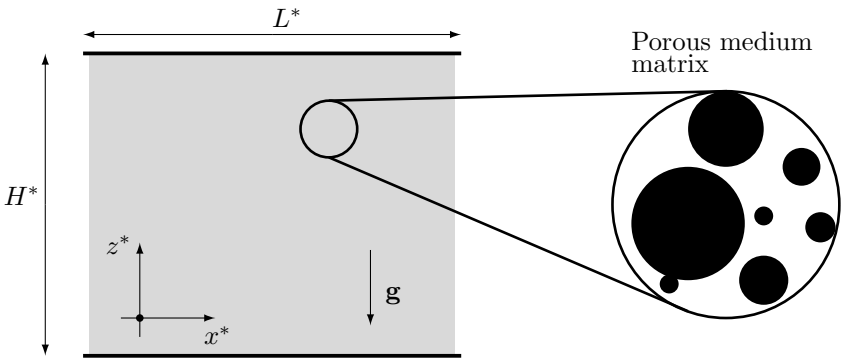

FIGURE 2.1 – Schematic of a representative porous domain. The black horizontal lines represent the domain boundaries, which confine the porous medium (grey zone). The porous material can be modelled as a matrix of spheres randomly distributed, but on mesoscales, it is efficiently described by averaged equations. Indications of the horizontal and vertical directions and gravity are also reported.

Stokes equations, the boundary layer around the spheres should be resolved, and the computational effort in not sustainable nowadays. Moreover, a precise domain mapping is required.

A possible solution consists into average the Navier-Stokes equations over a Reference Volume Element (REV), whose size is smaller than the domain height but larger than the characteristic pore size. A mathematical derivation of the Darcy equations is available in Whitaker (1998), which demonstrates that the Darcy equations represent an upscale of the Navier-Stokes equations. Now the meaning of the Darcy velocity is straightforward.

Finally, throughout this thesis we consider several coupling effects, such as buoyancy or Korteweg stresses. Buoyancy is treated with the Oberbeck-Bous-sinesq approximation, i.e. the effect of density changes is not negligible only into the buoyancy term, or in other terms, density variations are not comparable with the density magnitude itself. This assumption will be motivated in Chap. 3. In turn, the effect of Korteweg stresses is considered in Chap. 7, and will be discusses in detail in Chaps. 5 and 7. These two contributions will be accounted in the Darcy equation of motion.

An upscale analogue to the one obtained for the Navier-Stokes equations can be found for the solute (or energy) equation, with the additional hypothesis of negligible solute (or heat) flux from and towards the porous medium. Unfortunately, a general derivation has not been achieved yet for the Korteweg stresses. A more detailed analysis on this issue is presented in Chap. 7.

2.3 Outline of Part I

With respect to the outgoing fluxes, two different configurations are considered.

In Chap. 3, we will consider the canonical Rayleigh-Bénard configuration to investigate the effect of anisotropy on porous media convection. Our computational analyses span over few decades of the Rayleigh-Darcy number, and confirm the linear scaling of dissolution rate that was previously found in literature. In addition, we found that anisotropic permeability $\gamma < 1$, i.e. with vertical permeability smaller than horizontal permeability, effectively increases the Nusselt number compared with isotropic conditions. We link this seemingly counterintuitive effect with the modifications occurring to the flow topology in anisotropic porous media. We used proper orthogonal decomposition to investigate the feasibility of reduced order models in different regimes. Finally, we will use our data computed for the two-sided configuration (i.e. Dirichlet conditions on upper and lower boundaries) to examine the time evolution of solutal dynamics in the one-sided configuration, and we will demonstrate that the finite-time (short-term) amount of CO_2 that can be dissolved in anisotropic sedimentary rocks is much larger than in isotropic rocks.

In Chap. 4, we will use direct numerical simulations to examine the role of anisotropic permeability in a more physical configuration, where solute is injected from above and the lower boundary is insulated. We will present the entire transient dynamics for large Rayleigh-Darcy numbers and anisotropic permeability fields. We will also provide suitable and reliable models to parametrize the solute dissolution rate. Finally, we will propose a further application to carbon sequestration: the results obtained in the anisotropic one-sided configuration will be used in a large-scale model and we will demonstrate that the anisotropic permeability plays a key role in large and small sequestration projects.

3

Influence of anisotropic permeability on porous media convection

Part of the results presented in this chapter have been published under the title "Influence of anisotropic permeability on convection in porous media: implications for geological CO_2 sequestration" (De Paoli et al., 2016) in the journal *Physics of Fluids*.

3.1 Introduction

When a temperature difference is applied to a liquid filled porous layer, buoyancy driven flows may arise. If we refer to a two-dimensional cartesian layer across which a small temperature difference is applied, the arising gravity driven flow is dominated by diffusion. When temperature increases, instabilities occur and the flow becomes unstable and chaotic, finally achieving a fully convective regime. The temperature difference driving the flow within the layer is represented by a suitable dimensionless number, called Rayleigh-Darcy number (Ra), which quantifies the relative importance of advection compared to diffusion. Archival literature in this field is focused mainly on the onset of instabilities, which occurs at $Ra = 4\pi^2$ (Horton and Rogers Jr, 1945; Lapwood, 1948). The flow transfer efficiency is measured in terms of the Nusselt number (Nu), which supplies the value of the dimensionless heat flux transferred across the boundaries of the system. For the case of practical interest at large Rayleigh-Darcy numbers (up to $Ra = 4 \times 10^4$), it was shown by Hewitt et al. (2012) that Nu increases almost linearly with Ra, in good agreement with previous numerical and experimental studies (Otero et al., 2004; Backhaus et al., 2011). The above-mentioned problem maintains the same mathematical description when a solute difference is applied across the layer. In this case, the driving parameter is a modified version of the Rayleigh-Darcy number Ra based on

the concentration difference and the flow of solute is parametrized by the Sherwood number (Sh) or, more frequently, by a modified Nusselt number based on the concentration gradient.

Literature on this problem is vast and old, dating back to the Darcy's work for the derivation of the governing equations. However, in recent years this problem has received renovated attention for the implications it can bear in carbon dioxide (CO_2) sequestration strategies (Weir et al., 1996; Huppert and Neufeld, 2014). With reference to this problem, sequestration of liquid CO_2 via injection into brine-filled large geological formations has been identified as one of the possible remedies (Metz et al., 2005; Schrag, 2007; Friedmann, 2007). Essential aspects of CO_2 capture mechanisms are as follows: after injection, CO_2 dissolves in the brine (3% in weight), forms a heavier solute (CO_2+brine) and flows downward. An accurate evaluation of the solute downward flux is crucial to determine the filling time of the available reservoir capacity (from 320 to 10000 Gt worldwide, see Xu et al. (2006)), and consequently the optimal rate of CO_2 injection beneath the ground surface. However, the geological scale Ra numbers are of the order of $10^4 - 10^5$, which makes precise flow predictions hard to obtain.

According to current modelling approaches (Otero et al., 2004; Hewitt et al., 2012), the archetypal system to study solute convection into sedimentary rocks is the two-sided Rayleigh-Bénard configuration, in which convective transport occurs between a lighter layer (lower boundary) and a heavier layer (upper boundary). An alternative approach, perhaps more related to the physics of the concentration driven CO_2 dissolution process, is the so-called one-sided configuration (Hewitt et al., 2013a; Slim, 2014). In the one-sided configuration, convective transport occurs only away from the upper boundary and the dynamics of the system is a function of time. After onset, heavy plumes fall vertically with possible minor sideway perturbations, which in turn may produce plume interactions and branching before impingement on the lower boundary. Due to the impermeable bottom boundary condition, the domain starts filling up with dense solute and vertical convection is hindered (shutdown).

Even though sedimentary geological formations, which are composed by the subsequent deposition of horizontal layers, are inherently anisotropic (Xu et al., 2006) and are characterized by different values of the vertical-to-horizontal permeability ratio ($\gamma = k_v/k_h$), estimates for the vertical flux of solute (Nu) in literature (Otero et al., 2004; Hewitt et al., 2012; Riaz et al., 2006) are almost entirely based on the assumption of isotropic media ($\gamma = 1$). To date, there are only few works (Xu et al., 2006; Cheng et al., 2012; Ennis-King et al., 2005) on solute convection in anisotropic porous media, which however mainly focused on the study of instability inception, characterized by Ra lower than those typical of geological CO_2 sequestration. Our aim here is to explore the role of the anisotropic rock permeability (different values of γ) and to extend previous analyses on solute convection at large Rayleigh-Darcy numbers in anisotropic porous media.

The present chapter is built as follows. In Sec. 3.2 we will describe the governing equations and the boundary conditions adopted to run the present numerical simulations. We will consider first the analysis of the two-sided configuration: since in this configuration the flow reaches a steady state dynamic, time averages can be done and can help to identify the main convection mechanisms in a more convincing way if compared with the one-sided configuration (Huppert and Neufeld, 2014). Also important, the dissolution flux of solute in the one-sided cell can be directly computed from the two-sided model (Hewitt et al., 2013a). In Sec. 3.3 we will discuss the role of the anisotropic rock permeability on the vertical flux of solute. In particular, we will show that, compared to the isotropic case, increasing the horizontal rock permeability leads to a remarkably larger downward flux of solute. A physical explanation of this result will be also given based on a detailed examination of the flow topology. In Sec. 3.4 we will use proper orthogonal decomposition to investigate the feasibility of reduced order models at different regimes. In Sec. 3.5 we will use our previous results on the two-sided configuration to introduce and discuss the dynamics of the one-sided configuration. We generalize the shutdown model presented in literature (Hewitt et al., 2013a), accounting for the influence of the anisotropic rock permeability on the overall amount of solute dissolved in time. Finally, in Sec. 3.6 we will draw conclusions on possible implications of our results on long-term CO_2 storage.

3.2 Methodology

We consider a fluid-saturated porous medium in a two dimensional domain, assuming a uniform porosity Φ and considering different values of the vertical (k_v) to horizontal (k_h) permeability ratio $0.25 \leq \gamma \leq 1$. The value of $\gamma < 1$ is chosen to be representative of real geological applications (Ennis-King et al., 2005), i.e. $\gamma < 1$. The unstable density stratification (characterized by a top-to-bottom density difference $\Delta\rho^*$) drives the solute in a downward flow which is incompressible and governed by the Darcy's law. In a two dimensional domain, being u^* and w^* the velocities along the horizontal (x^*) and the vertical direction (z^*) respectively, and with p^* and C^* the pressure and solute concentration, the balance equations are:

$$\frac{\mu}{k_h}u^* = -\frac{\partial p^*}{\partial x^*} \quad , \quad \frac{\mu}{k_v}w^* = -\frac{\partial p^*}{\partial z^*} - \rho^* g \tag{3.1}$$

$$\frac{\partial u^*}{\partial x^*} + \frac{\partial w^*}{\partial z^*} = 0 \tag{3.2}$$

where μ is the fluid viscosity and g the acceleration due to gravity. The superscript * denotes dimensional variables. For the range of Rayleigh numbers considered in the present study, the Oberbeck-Boussinesq hypothesis

can be applied.[1] As a consequence, we assume that the fluid density ρ^* is the only solute-dependent property, which can be evaluated in terms of the concentration of solute C^* into the mixture using the linear equation of state:

$$\rho^* = \rho_s^* \left[1 - a(C_s^* - C^*)\right], \tag{3.3}$$

where a is a positive constant coefficient while C_s^* and ρ_s^* are the concentration field and the density value at the top boundary.

Neglecting the effects of dispersion, and indicating with D the solute diffusivity, the concentration fulfills the time-dependent advection-diffusion equation:

$$\Phi \frac{\partial C^*}{\partial t^*} + u^* \frac{\partial C^*}{\partial x^*} + w^* \frac{\partial C^*}{\partial z^*} = \Phi D \left(\frac{\partial^2 C^*}{\partial x^{*2}} + \frac{\partial^2 C^*}{\partial z^{*2}} \right) . \tag{3.4}$$

We assume impenetrable boundaries kept at a fixed solute concentration (mimicking the presence of a saturated solution near the top boundary and of pure fluid near the bottom boundary):

$$w^* = 0 \quad , \quad C^* = 0 \quad \text{on} \quad z^* = 0 \quad , \tag{3.5}$$

$$w^* = 0 \quad , \quad C^* = C_s^* \quad \text{on} \quad z^* = H^* \quad , \tag{3.6}$$

whereas periodicity is applied along the horizontal direction x^*.

3.2.1 Dimensionless equations

A relevant velocity scale for the flow is the free-fall buoyancy velocity, $W^* = gk_v\Delta\rho^*/\mu$. To account for the effect of anisotropy, we use different velocity/length scales in the vertical and horizontal directions (through the introduction of the scaling factor $\sqrt{\gamma}$). In particular, we set:

$$x = \frac{x^*}{H/\sqrt{\gamma}} \quad , \quad z = \frac{z^*}{H} \quad , \quad u = \frac{u^*}{W^*/\sqrt{\gamma}} \quad , \quad w = \frac{w^*}{W^*} \tag{3.7}$$

$$p = \frac{p^*}{\mu W^* H^*/k_v} \quad , \quad C = \frac{C^* - C_s^*}{C_s^*} \quad , \quad t = \frac{t^*}{\Phi H^*/W^*} \quad . \tag{3.8}$$

The governing parameter of the problem is the Rayleigh-Darcy number:

$$Ra = Ra_T \cdot Da = \frac{gH^* k_v \Delta\rho^*}{\mu \Phi D}, \tag{3.9}$$

defined based on the thermal Rayleigh number ($Ra_T = g\Delta\rho^* H^{*3}/\mu D$) and on the Darcy number ($Da = k_v/H^{*2}$). The Rayleigh-Darcy number can

[1] Landman and Schotting (2007) shown that the Oberbeck-Boussinesq approximation approximation is valid if $Ra\,/(\Delta\rho^*/\rho_s^*)$, which is widely verified in the present work.

also be seen as the ratio of diffusive and convective time scales (but also as an inverse diffusivity (Hewitt et al., 2013b) or as the dimensionless layer thickness (Slim, 2014). In dimensionless form, Eqs. (3.1), (3.2) and (3.4) become:

$$u = -\frac{\partial P}{\partial x} \quad , \quad w = -\frac{\partial P}{\partial z} - C \tag{3.10}$$

$$\frac{\partial u}{\partial x} + \frac{\partial w}{\partial z} = 0 \tag{3.11}$$

$$\frac{\partial C}{\partial t} + u\frac{\partial C}{\partial x} + w\frac{\partial C}{\partial z} = \frac{1}{Ra}\left(\gamma\frac{\partial^2 C}{\partial x^2} + \frac{\partial^2 C}{\partial z^2}\right) \tag{3.12}$$

where $P = p + z/(aC_s^*)$ is the reduced pressure. The effect of anisotropy (γ) is explicit only in Eq. (3.12) but it is also present in the other equations through the reference length/velocity scales defined above. The dimensionless boundary conditions result:

$$w = 0 \quad , \quad C = -1 \quad \text{on} \quad z = 0 \tag{3.13}$$

$$w = 0 \quad , \quad C = 0 \quad \text{on} \quad z = 1 \ . \tag{3.14}$$

Equations (3.10)-(3.12) are solved by a Fourier-Chebyshev pseudo-spectral method. Further details on the numerical approach can be found in Appendix A and in Sec. 3.A.1.

In the present study, $\gamma < 1$ is obtained by increasing the horizontal permeability k_h while keeping k_v constant (i.e. keeping the same Ra). By doing so, we can compare simulations at the same Ra (i.e. same driving force or same domain height), but different γ (i.e. different porous medium). We perform a systematic study of solutal convection in anisotropic porous media in the Ra parameter space covering a broad range of Ra numbers ($50 \leq Ra \leq 5 \times 10^4$), while assuming $0.25 \leq \gamma \leq 1.00$.

3.3 Results

In this section, we describe the results obtained from numerical simulations of the two-sided configuration with anisotropic rock permeability ($\gamma \leq 1$). In fact, we start our analysis considering the dynamics of the flow for $\gamma = 1$ (isotropic rock permeability). The dynamics of the present system depends on the value of the Rayleigh-Darcy number. For $Ra \leq 4\pi^2$ diffusion dominates and convection is prevented (Horton and Rogers Jr, 1945; Lapwood, 1948). For $4\pi^2 < Ra < 1300$ the flow exhibits large and steady non-linear rolls, with the onset of a secondary instability as Ra approaches the value $Ra \simeq 1300$. This dynamics has been extensively analysed in previous works (Graham and Steen, 1994; Otero et al., 2004) and will not be discussed

further here. For $Ra > 1300$ the system cannot sustain the stable quasi-periodic configuration and undergoes a transition towards a chaotic state, characterized by the occurrence of unsteady motions (Otero et al., 2004). A brief description of the flow properties at low and intermediate regimes is provided in Sec. 3.4.

We describe the flow structure using contour maps of the concentration field C, since concentration is transported by the velocity field and reproduces faithfully the underlying flow structure. The basic fluid mechanics of such flow is depicted in Fig. 3.1.

We focus on the first row of Fig. 3.1, which shows contour maps of C in the $x-z$ plane for $Ra = 8 \times 10^3$ (Fig.e 3.1a), $Ra = 16 \times 10^3$ (Fig. 3.1b) and $Ra = 5 \times 10^4$ (Fig. 3.1c).

Small fingers of light fluid raise from the bottom boundary moving upward, while corresponding fingers of heavy fluid move downward from the top boundary. These fingers, named *protoplumes* in Hewitt et al. (2012), come close each other and form larger plumes (*megaplumes*) that penetrate across the domain and reach the opposite boundary. Large plumes, whose velocity is initially low, are vigorously accelerated by buoyancy and reach the opposite boundary, where they are deflected horizontally. These horizontal branches push closer the newly forming fingers so to produce a new descending (or ascending) large plume in a cyclic fashion.

To further clarify the dynamics of merging plumes, in Fig. 3.1d to 3.1i we show the time evolution of the concentration field C measured along an horizontal slice at two different vertical positions. The horizontal slice is located at a distance $z = 10^2/\,Ra$ from the lower boundary (just outside of the boundary layer) in Fig. 3.1d-e-f, and at $z = 1/2$ (cell centerline) in Fig. 3.1g-h-i. The position of the two cutting planes is explicitly shown in Fig. 3.1a-c and is indicated as z_A, z_B. Near the wall (Fig. 3.1d-e-f), the emerging picture indicates the presence of a characteristic structure, consisting of protoplumes (small ribs) that coalesce to form megaplumes (long and persistent roots). Adjacent megaplumes can merge or form branches, as indicated by the meandering concentration pattern. From a comparative analysis of Fig. 3.1d, Fig. 3.1e and Fig. 3.1f it is apparent that the number and the strength of protoplumes near the boundary increases with increasing Ra. Farther from the wall (Fig. 3.1g-h-i), megaplumes increase persistence and stability for increasing Ra. This is revealed by the regular streaky pattern at $Ra = 5 \times 10^4$ (Fig. 3.1i) in comparison with those at smaller Ra (Fig. 3.1g-h).

The dynamics of protoplumes and megaplumes qualitatively described above for $\gamma = 1$ remains substantially unchanged also for $\gamma \neq 1$, though the assumption of a anisotropic rock permeability produces quantitative effects. To quantify these effects, we consider the behaviour of the mean concentration profile $\langle C \rangle$ along the vertical direction z. Results are shown in Fig. 3.2. In particular, in Fig. 3.2a we present the reference results obtained assuming $\gamma = 1$ and varying Ra ($Ra = 8 \times 10^3$, $Ra = 16 \times 10^3$

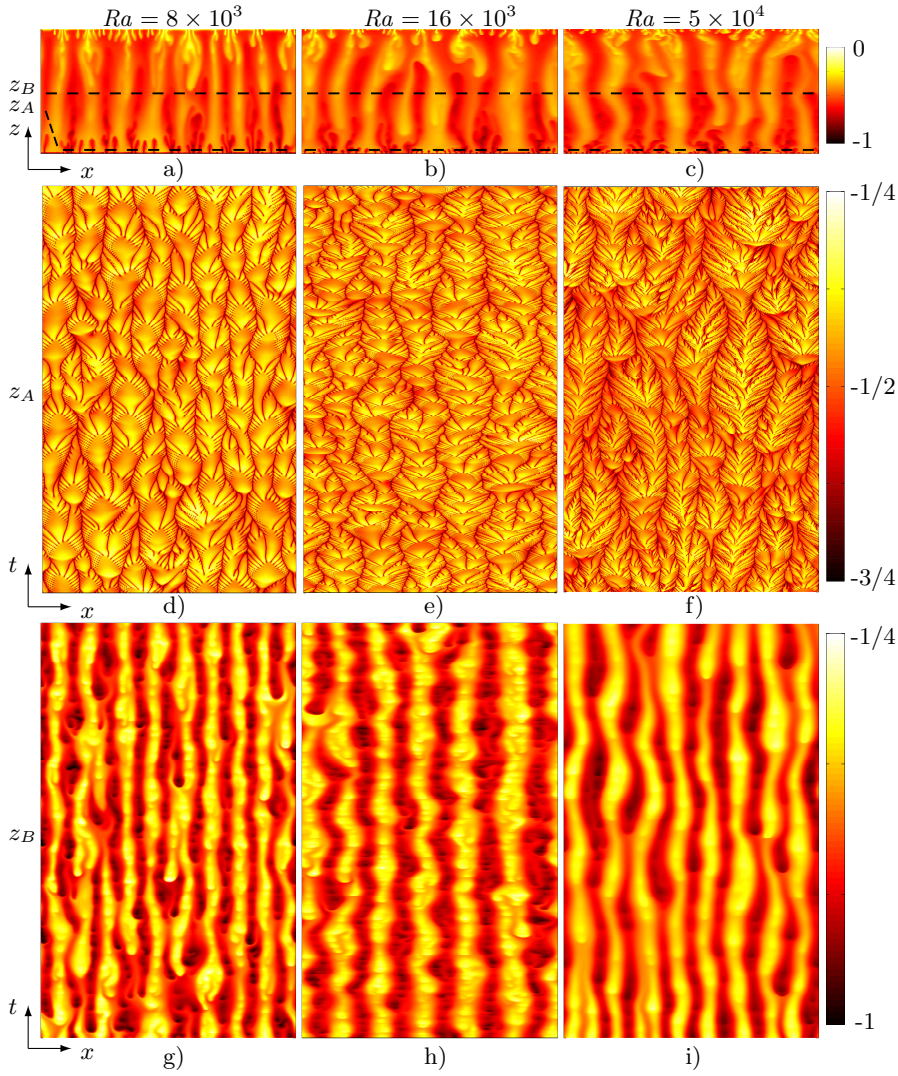

FIGURE 3.1 – Panels a-c) contour maps of the concentration field C of the solute for $Ra = 8 \times 10^3$ (panel a), $Ra = 16 \times 10^3$ (panel b) and $Ra = 5 \times 10^4$ (panel c). Panels d-e-f and g-h-i) space-time (also called *world lines*) measurements of C along two horizontal slices located at $10^2/\,Ra$ from the lower layer (z_A) (panels d-e-f), i.e. just outside of the boundary layer whose extension is $15/\,Ra$, as suggested by Otero et al. (2004), and at the centerline of the cell (z_B) (panels d-e-f). The location of the "cutting planes" z_A and z_B is explicitly shown in panels a-c. The value of Ra for the world lines measurements corresponds to that of the contour maps in the above panels ($Ra = 8 \times 10^3$, $Ra = 16 \times 10^3$ and $Ra = 5 \times 10^4$ from left to right).

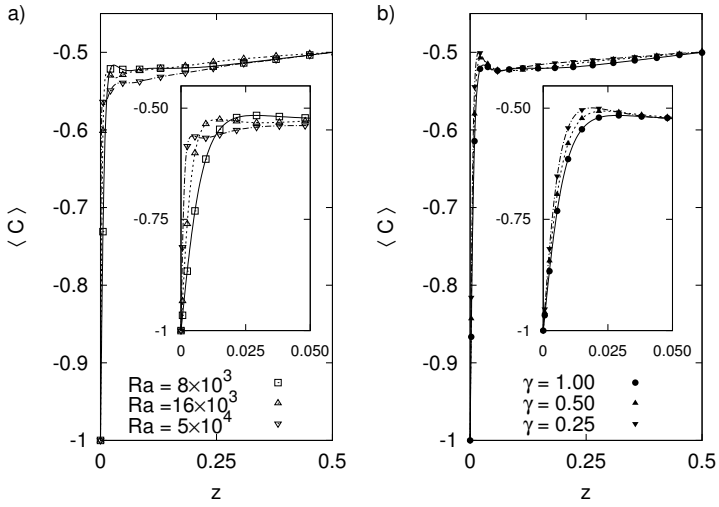

FIGURE 3.2 – Panel a) profiles of the average concentration $\langle C \rangle$ computed along the vertical direction z for different Ra numbers with $\gamma = 1$. Panel b) profiles of the average concentration $\langle C \rangle$ computed along the vertical direction z at $Ra = 8 \times 10^3$ and different values of γ. The insets in each panel show a close-up view of the region near the boundary.

and $Ra = 5 \times 10^4$). In Fig. 3.2b we show the results obtained for a given Ra ($Ra = 8 \times 10^3$) and different γ ($\gamma = 1.00$, $\gamma = 0.50$ and $\gamma = 0.25$). Note that brackets $\langle \cdot \rangle$ indicate average in time and in space over the horizontal direction x. A close up view of the mean concentration profiles near the boundary (up to $z = 1/20$) is shown in the inset of each panel. We analyse first the effect of Ra on the mean concentration profile (Fig. 3.2a). The jump of $\langle C \rangle$ to the centerline value $\langle C \rangle = -1/2$ is observed across a thin boundary layer, the thickness of which can be computed as $\delta = \Delta C / 2[\partial \langle C \rangle / \partial z]_{z=0} = 1/2[\partial \langle C \rangle / \partial z]_{z=0}$, with ΔC being the overall top-to-bottom concentration difference and equal to 1 due to the concentration scale used. A similar behaviour is also observed for varying γ (Fig. 3.2b). Note that the significant reduction of δ for decreasing γ is a strong indication for the enhanced vertical flux of solute (Schumacher, 2009).

We briefly discuss here the behaviour of the root mean square (rms) of the solute concentration fluctuations C_{rms} as a function of the vertical coordinate z. Results are shown in Fig. 3.3. We consider first the effect of Ra on C_{rms} for an isotropic porous medium (Fig. 3.3a). We clearly observe that for increasing Ra the peak of C_{rms} moves toward the boundary while remaining almost constant in amplitude. This is a further indication of the reduction of the boundary layer thickness discussed above. A similar trend is observed for varying γ (Fig. 3.3b). A close up view of the behaviour of C_{rms} near the boundary (up to $z = 1/20$) is provided in the inset of both

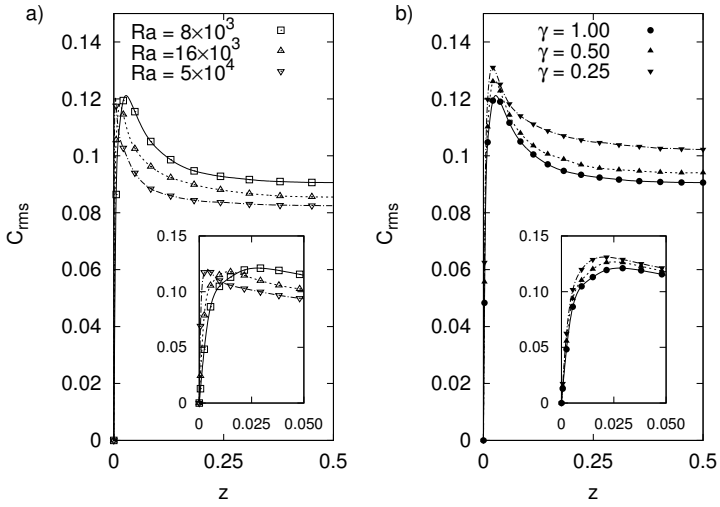

FIGURE 3.3 – Panel a) profiles of the root mean square of the concentration fluctuations, $C_{\rm rms}$, computed along the vertical direction z for different Ra ($Ra = 8 \times 10^3$, $Ra = 16 \times 10^3$, $Ra = 5 \times 10^4$) and $\gamma = 1$. Panel b) profiles of the root mean square of the concentration fluctuations computed along the vertical direction z at $Ra = 8 \times 10^3$ and different values of γ ($\gamma = 1$, $\gamma = 0.50$ and $\gamma = 0.25$). The inset in each panel shows a close up view of the region near the boundary.

Fig. 3.3a and Fig. 3.3b to properly visualize the shape of the $C_{\rm rms}$ profile. The behaviour of the maximum value of solute fluctuations, $\max(rms)$, as a function of Ra and γ is shown in Fig 3.4. These results clearly indicate that the maximum value of $C_{\rm rms}$ (as well as of $w_{\rm rms}$) remains almost constant for increasing Ra. Yet, $\max(C_{\rm rms})$ and $\max(w_{\rm rms})$ increase remarkably for decreasing γ.

To evaluate explicitly the downward solute flux for different Ra, we computed the actual value of the Nusselt number (see Appendix 3.A). The behaviour of Nu as a function of Ra is shown in Fig. 3.5. The inset refers to the behaviour of Nu over the entire range of Rayleigh numbers simulated in the present work ($50 < Ra < 5 \times 10^4$) for the isotropic porous medium ($\gamma = 1$, $-\bigcirc-$). These results are shown together with those provided by Hewitt et al. (2012) (—) to confirm and extend previous predictions on the asymptotic linear increase of Nu with Ra (Otero et al., 2004; Hewitt et al., 2012).

The results shown in the main panel of Fig. 3.5 are one of the key messages of the present chapter. Symbols indicate the values of Nu obtained from simulations at $Ra \geq 2 \times 10^3$ for different γ: $\gamma = 1$ ($-\blacktriangledown-$), $\gamma = 0.75$ ($-\blacktriangle-$), $\gamma = 0.50$ ($-\bullet-$) and $\gamma = 0.25$ ($-\blacksquare-$). A remarkable effect of γ on Nu is easy to observe over the entire range of Ra, with increments of Nu up to about 40% for $\gamma = 0.25$. This provides a clear indication of the

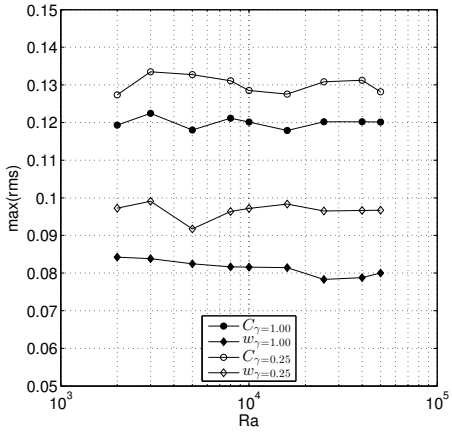

FIGURE 3.4 – Maximum value of the temporally and spatially averaged root mean square of the concentration fluctuations (C_{rms}), vertical velocity (w_{rms}) and horizontal velocity (u_{rms}) as a function of Ra and for two values of γ ($\gamma = 1$ and $\gamma = 0.25$).

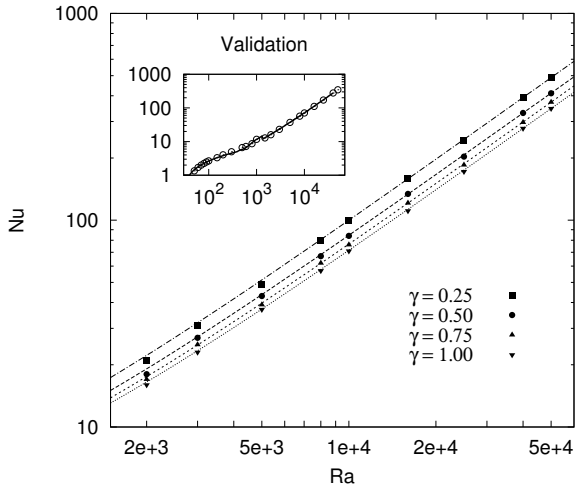

FIGURE 3.5 – Time and space averaged Nusselt number Nu as a function of the Rayleigh-Darcy number (Ra) for different values of the permeability ratio $\gamma = k_v/k_h$ ($\gamma = 1$, $\gamma = 0.75$, $\gamma = 0.50$ and $\gamma = 0.25$). Results are shown only for high Rayleigh-Darcy numbers ($Ra \geq 2 \times 10^3$). Predictions from the simplified model $Nu = \beta + \alpha\gamma^n\, Ra$ (with $\alpha = 0.00688$ and $\beta = 2.75$ proposed by Hewitt et al. (2012) for the isotropic case, and $n = -1/4$ to account for anisotropic permeability) are shown (lines) together with the numerical results (symbols). The inset shows the values of Nu (symbols) for $\gamma = 1$ and for all Ra considered in this study. Results from Hewitt et al. (2012) (solid line) are also shown for comparison.

enhanced downward flux of solute occurring when increasing the horizontal permeability. We wish to remark here that our simulations for $\gamma < 1$ are run by increasing k_h (horizontal permeability) while keeping k_v (vertical permeability) constant. This choice was necessary to compare our results against previous works (Otero et al., 2004; Hewitt et al., 2012) (we kept Ra constant while varying γ). Current results can be predicted by the linear scaling

$$Nu = \beta + \alpha\gamma^n \, Ra \tag{3.15}$$

with $\alpha = 0.00688$ and $\beta = 2.75$, which extends that proposed by Hewitt et al. (2012) for the isotropic case $\gamma = 1$: our data show that it is possible to maintain the same scaling, though introducing the permeability ratio γ to the power $-1/4$. Note that the precise value of n obtained from data fitting is $n = -0.2514 \pm 0.0053$. It was not possible to compare our data against previous experimental or numerical results from literature: we were able to find only few studies (Xu et al., 2006; Cheng et al., 2012; Green and Ennis-King, 2014) analysing flow convection in a fluid saturated anisotropic porous medium. In Xu et al. (2006), the authors studied by linear and global stability analysis the onset of convection (which occurs at lower Ra than those considered here) and found indications that reducing γ leads to a faster solute dissolution (increase of Nu). Later, Cheng et al. (2012) combined stability analysis and numerical simulations (up to $Ra = 6400$) to show that solutal convection can be triggered earlier in anisotropic porous media, leading the authors to the conclusions that a wider range of potential reservoirs can be effectively exploited for CO_2 sequestration. More recently, Green and Ennis-King (2014) found that reducing γ could decrease Nu, which is only in apparent contradiction with our results. In Green and Ennis-King (2014), decreasing γ is obtained by decreasing k_v rather than by increasing k_h. Note however that varying k_v leads to different Ra. Hence, it is difficult to compare results of Nu for different γ (and also different Ra). To the best of our knowledge, these calculations have never been performed in the high-Ra regime. In the following, we will also give sound physical reasons why reducing γ can lead to a seemingly counterintuitive increase of solute vertical flux (Nu).

In the high-Ra regime, the flow is made of a sequence of falling plumes that drive the heavy fluid (high concentration of solute) downward and by rising plumes that drive light fluid (low concentration of solute) upward (Neufeld et al., 2010). In Fig. 3.6 we show a close up of a falling plume that is developing near the top boundary over a length of one third of the domain. The thick black line identifies the mid value of the dimensionless concentration $C = -1/2$ and represents the contour of the plume. The values of the vertical velocity gradient, $\partial w/\partial z$, are indicated in Fig. 3.6a with the color range, white being the maximum positive gradient and black being the maximum negative gradient. The values of the vertical velocity, w, are indicated in Fig. 3.6b with the color range, white being the max-

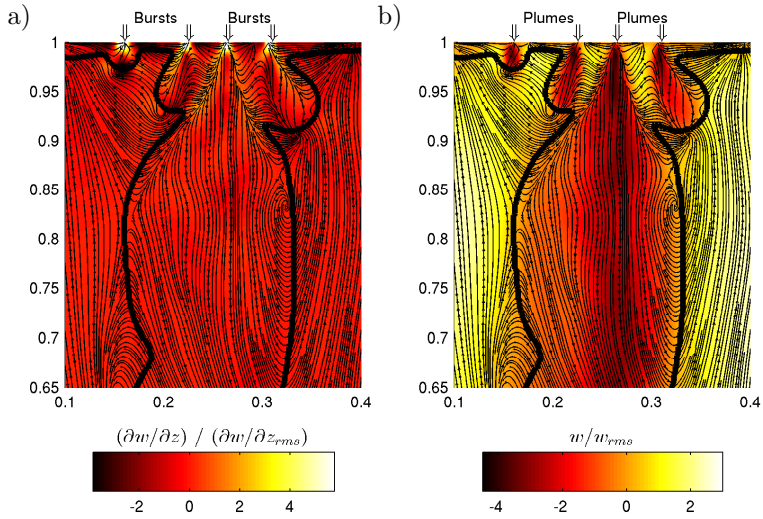

FIGURE 3.6 – Sketch of a falling plume near the top boundary, identified by the isocontour $C = -1/2$ (thick line). Panel a) contour maps of the vertical velocity gradient $\partial w/\partial z$ within the plume, normalized by the root mean square value $\partial w/\partial z_{\mathrm{rms}}$. Panel b) contour maps of the vertical velocity w within the plume, normalized by the root mean square value w_{rms};

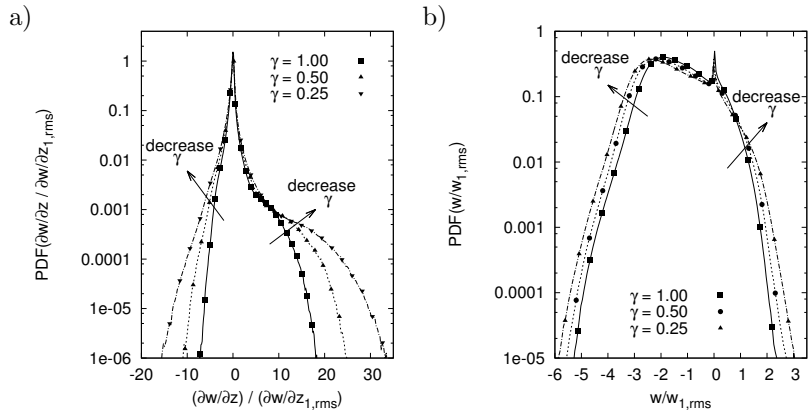

FIGURE 3.7 – Panel a) Probability Density Function (PDF) of the vertical velocity gradient $\partial w/\partial z$, normalized by the root mean square value of $\partial w/\partial z$ for $\gamma = 1$, $\partial w/\partial z_{1,\mathrm{rms}}$. Panel b) Probability Density Function (PDF) of fluid vertical velocity w, normalized by the root mean square value of w for $\gamma = 1$, $w_{1,\mathrm{rms}}$. The PDF calculation is done considering only the fluid region of falling plumes (i.e. $C > -1/2$, see Fig. 3.6). Results refer to the case of $Ra = 8 \times 10^3$.

imum upward velocity and black being the maximum downward velocity. In both Fig. 3.6a-b flow streamlines are also plotted to show in detail the flow behaviour inside and outside the plume. Focusing on the tiny region near the top boundary (i.e. $z \geq 0.95$ in Fig. 3.6a) it is possible to observe a number of small, concentrated bursts of positive vertical velocity gradient that control the development of the plumes (identified by regions of large downward velocity in Fig. 3.6b). Following the plume structure, we can see that farther from the top boundary ($z \simeq 0.75$) the vertical velocity gradient is small (Fig. 3.6a), indicating that the vertical downward velocity of plumes is maximum (Fig. 3.6b). Flow streamlines clearly mark the regions where the fluid is recirculating due to the shear produced by the falling plume interacting with the neighbouring rising plumes. In an effort to explain the importance of the permeability ratio γ in modifying the flow, we want to focus specifically on the modification to w and $\partial w/\partial z$. We compute the probability density function (PDF) of w and $\partial w/\partial z$ in the region of the falling plumes, as identified in Fig. 3.6, for different values of γ. We plot the PDF($\partial w/\partial z$) in Fig. 3.7a and the PDF(w) in Fig. 3.7b. All data are normalized by the corresponding root mean square (rms) for $\gamma = 1$. We discuss first the PDF($\partial w/\partial z$) in the isotropic case, corresponding to $\gamma = 1$ ($-\blacksquare-$). The distribution is asymmetric, due to the sampling on the falling plume, with the most probable value in zero. We also observe a wide positive tail, indicating that a large proportion of the events correspond to a velocity increase while the fluid is falling. When γ is decreased, the distribution broadens, demonstrating a more probable occurrence of the positive, but also negative, extreme events. We remark here that while $\partial w/\partial z > 0$ is an indication of plume acceleration, $\partial w/\partial z < 0$ is an indication of plume deceleration. A vis-a-vis comparison of Fig. 3.6a and Fig. 3.7a suggests that the events $\partial w/\partial z > 5$, for which we report an increase for decreasing γ, are those associated to the newly forming plumes. If we focus on the negative tail, we can associate the increase of events $\partial w/\partial z < -5$ with strong deceleration in the vertical direction of the falling plume when approaching the bottom boundary (not shown in Fig. 3.6). The decrease of γ has a similar effect also on the distribution of w (Fig. 3.7b): decreasing γ increases the frequency of positive and negative extreme events (predominantly occurring in the core of the plume, see Fig. 3.6b). We report also a decrease of the frequency of moderate events. Falling plumes are large convective regions that entrain the fluid downward. However, falling plumes can exhibit, due to the shearing action of the neighbouring rising plumes, also small areas characterized by lumps of fluid going upward: this explains the positive values in Fig. 3.7b. From the qualitative behaviour of Fig. 3.6 and the quantitative results in Fig. 3.7, we can now explain why in Fig. 3.5 we observe an increase of Nu for a decrease of the permeability ratio γ. When we increase the horizontal permeability k_h, we facilitate the horizontal motion of the fluid with a corresponding increase of $\partial u/\partial x$. To preserve the mass balance in the flow domain, continuity must prescribe a corresponding in-

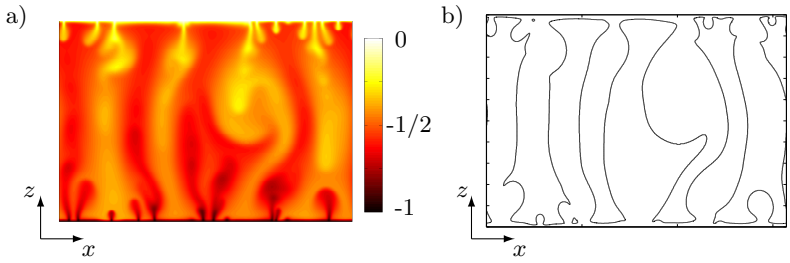

FIGURE 3.8 – Panel a) contour maps of the concentration field C in the entire domain. Dark regions indicate small solute concentration (light fluid) whereas bright regions indicates large solute concentration (heavy fluid). Panel b) corresponding shape of plumes identified by the present plume-detection algorithm, i.e. by detecting the contour line $C(\mathbf{x}) = -1/2$.

crease of the magnitude of $\partial w/\partial z$. This observation and the broadening of the tails in the velocity distribution reported in Fig. 3.7b can lead us to the conclusion that a decrease of the horizontal resistance induces an increase of the flow in the vertical direction, even though the vertical permeability k_v is maintained constant.

3.3.1 Plume dynamics

As discussed above, solute convection in porous media is essentially driven by plumes. For this reason, we wish to investigate further the characteristics of plumes for varying Ra and γ.

Plume detection Plume identification is a longstanding problem in buoyancy-driven flows (see Paparella and von Hardenberg (2012); Ching et al. (2004); van der Poel et al. (2015) and references therein). Plumes are usually identified based on the value of the velocity-temperature (or concentration) correlation or on the value of the temperature (or concentration) fluctuations. Although the definition of plumes based on these markers leads to slightly different results for pure fluid thermal (or solutal) convection, we checked that in the present case of solutal convection in porous media they all lead essentially to the same results. Following Otero et al. (2004), Hewitt et al. (2012) and Slim (2014), in the present work we identify a descending plume P as the set of points $\mathbf{x} = (x, z)$ (in the domain D) where

$$P = \{\mathbf{x} \in D \quad : \quad C(\mathbf{x}) \geq -1/2\} \ .$$

An example of plume detection is given in Fig. 3.8, where we show the contour maps of the concentration field (Fig. 3.8a) and the corresponding shape of plumes detected with the present algorithm, i.e. by detecting the contour line $C(\mathbf{x}) = -1/2$ (Fig. 3.8b).

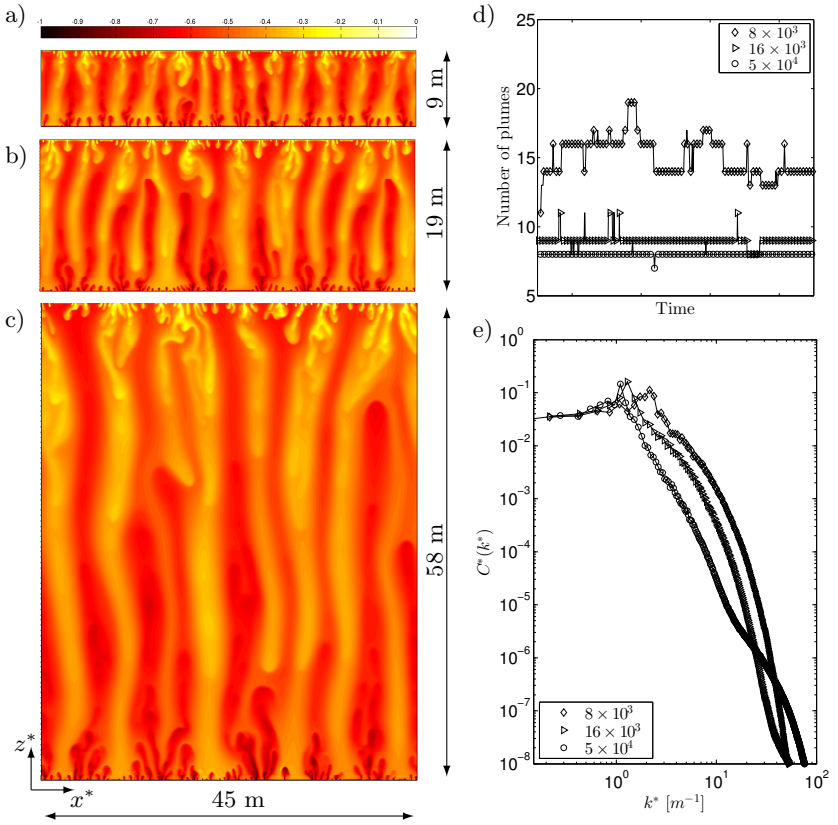

FIGURE 3.9 – Plume statistics for the isotropic case ($\gamma = 1$) and for three different Ra number. Panels a-c) instantaneous distribution of the concentration fields at $Ra = 8 \times 10^3, 16 \times 10^3$ and 5×10^4. Panel d) number of plumes computed in time (along the half channel height) using the present plume detection algorithm. Panel e) power spectra of the concentration C for the three different values of Rayleigh-Darcy number analysed here as a function of the physical wavenumber $k^* = 2\pi n/L^*$.

Plume statistics Upon identification of a plume, we are able to compute their number, width and extension (surface area). Plume statistics computed at different Ra and for the isotropic case ($\gamma = 1$) are given in Fig. 3.9: in the left column (Fig. 3.9a-c) we show contour maps of solute concentration in the entire domain (whose size is here expressed in dimensional units [m]) for $Ra = 8 \times 10^3$ (Fig. 3.9a), $Ra = 16 \times 10^3$ (Fig. 3.9b) and $Ra = 5 \times 10^4$ (Fig. 3.9c). The values of H^* and L^* have been chosen to mimick a realistic physical situations. Hence, H^* ranges between 9 and 58 m whereas $L^* = 45$ m. The time evolution of the number of megaplumes (detected along the centerline of the channel, $z^* = H^*/2$, using the plume

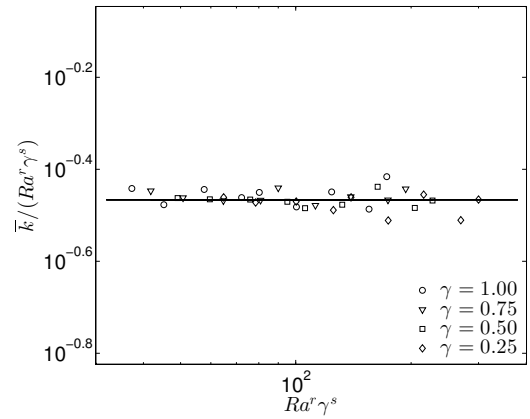

FIGURE 3.10 – Horizontally-averaged wavenumbers $\overline{k}$ obtained from our numerical simulations at different Rayleigh-Darcy numbers Ra and different permeability ratios γ (symbols). Results are normalized by Ra^r and γ^s. An analytical scaling with $r = 0.48$ and $s = -0.40$ (straight line) is presented for comparison purposes.

detection algorithm presented above) for the three different cases is presented in Fig. 3.9d. Increasing Ra has a twofold effect on megaplumes: it decreases their number while increasing their persistence. This is clearly visible from the variability of the number of megaplumes in time, which is highly fluctuating for $Ra = 8 \times 10^3$, whereas it is almost constant for $Ra = 5 \times 10^4$. Note also that, since the physical domain is kept constant for varying Ra ($L_x^* = 45.562$ m), a reduction in the number of plumes (at large Ra) reflects into an increase in the average plume diameter (i.e. the plume width). Results, not shown here for brevity, indicate that the average plume diameter is 1.5 m for $Ra = 8 \times 10^3$, 2.4 m for $Ra = 16 \times 10^3$ and 2.8 m for $Ra = 5 \times 10^4$. A more quantitative estimate of the number of megaplumes can be obtained by looking at the power spectra of the concentration field computed along the centerline of the channel, as shown in Fig. 3.9f. The wavenumber ($k^*_{\max}$) at which the power spectrum has a maximum is linked to the number of megaplumes in the cell. In particular, we found that $k^*_{\max} = 2.15$ m^{-1} for $Ra = 8 \times 10^3$, $k^*_{\max} = 1.29$ m^{-1} for $Ra = 16 \times 10^3$ and $k^*_{\max} = 1.10$ m^{-1} for $Ra = 5 \times 10^4$. From the wavenumber definition $k^*_{\max} = 2\pi n / L^*$, we can therefore evaluate n, here identifying the number of megaplumes, for the three different cases. We obtain $n \simeq 15$ for $Ra = 8 \times 10^3$, $n \simeq 9$ for $Ra = 16 \times 10^3$ and $n \simeq 8$ for $Ra = 5 \times 10^4$, in agreement with the value of n inferred from the qualitative plume detection (see Fig. 3.9d). From the knowledge of the concentration power spectrum $C(k)$, being $C(k)$ the amplitude of the Fourier transform in the Fourier space, we can compute, at each time instant t_j, the average horizontal wavenumber

k_j as

$$k_j = \frac{\int kC(k)dk}{\int C(k)dk} \ . \tag{3.16}$$

The instantaneous values of the wavenumber k_j are then averaged also in time to give the dimensionless average wavenumber $\overline{k}$. We perform this calculation for both isotropic ($\gamma = 1$) and anisotropic permeability ($\gamma < 1$). From our numerical measurements (Fig. 3.10), we found

$$\overline{k} = 0.342\, Ra^{0.48}\, \gamma^{-0.40}, \tag{3.17}$$

which is in fair agreement with the predictions given for the isotropic case (Hewitt et al., 2012) $\overline{k} = 0.48\, Ra^{0.4}$. The slight discrepancy between the results could be possibly due to a difference in the cell dimension (see Appendix 3.A).

3.4 Low-dimensional modelling

In previous sections of this chapter, we observed that a large computational cost is necessary to describe convection in porous media at large Rayleigh numbers. This represents a limitation to the time and scales that can be accurately examined. Moreover, a challenge in current applied mathematics consists in the computational reduction of non-linear problems, typically characterized by high computational costs, into lower order problems with the aid of Reduced Order Models (ROMs). The aim of these models is to speed up the calculation and/or understand the governing large-scale dynamics.

This approach has been applied in many field of physics and, among the others, many attempts to reduce turbulence have been done. However, we are faraway from the reduction of fully developed turbulent flows. Within the context of convection in porous media, few results have been achieved using a proper orthogonal decomposition. In particular, Siade et al. (2010) analysed a one-dimensional buoyant current in porous media, using an approach similar to that presented in Sec. 4.5. They provide a strategy for optimal snapshot selection found by maximizing the minimum eigenvalue of the snapshot covariance matrix. In addition, in literature two-dimensional satured porous layers have been considered (Chini et al., 2011; Wen et al., 2012). With the aid of a POD, Chini et al. (2011) proposed a model reduction strategy which fits very well the DNS results at low Rayleigh number ($Ra = 100$). In the work of Wen et al. (2012), the authors employed a reduced order model to derive new upper bounds for Rayleigh-Bénard convection in porous media. They also provide an estimate of the number of degrees of freedom (n_m) of the reduced model required to fully describe (in terms of Nusselt number) the system, i.e. $O(Ra) < n_m < O(Ra^2)$. No investigations are available for high Rayleigh numbers.

In this section, we will use a proper orthogonal decomposition to analyse convection in isotropic porous media at low ($Ra = 5 \times 10^2$), intermediate ($Ra = 2 \times 10^3$) and high ($Ra = 16 \times 10^3$) Rayleigh numbers.

In Sec. 3.4.1 and 3.4.2, we describe the Reduced Order Modelling (ROM) technique and the Proper Orthogonal Decomposition (POD) respectively. In Sec. 3.4.3, we discuss qualitatively and quantitatively the number of modes required to fully describe the systems considered. The reduced order modelling of convection in anisotropic porous media is left for future work.

3.4.1 Reduced order modelling

The investigated flow is fully described by the set of Eqs. (3.10)-(3.12), provided that $\gamma = 1$. An accurate solution obtained with a pseudo-spectral algorithm is computationally expensive, and Reduced Order Models (ROMs) could permit to get cheaper (but still accurate) solutions. However, some key points must be taken into account (Lassila et al., 2014):

1. if the decay of the singular values obtained via POD is sufficiently rapid, then a limited number of modes will potentially represent the solution and an attempt at building a ROM can be performed;

2. flow features that are not sufficiently energetic will not be in the POD, and thus cannot be captured by the ROM;

3. snapshots must refer to the same regime or to the same qualitative flow structure.

We performed a POD analysis and evaluated the number of modes required for an accurate description of this problem.

3.4.2 Proper orthogonal decomposition

Proper orthogonal decomposition is here used for the identification of coherent structures of concentration. It relies on a linear decomposition of a general vectorial field (concentration) $C(\mathbf{x}, t)$ with respect to the orthogonal modes (empirical eigenfunctions) $\Phi^i = \Phi^i(\mathbf{x})$. The concentration corresponding to the $n-$th snapshot can be reconstructed as:

$$C(\mathbf{x}, t_n) = C^n = \sum_{j=1}^{NT} a_j^n \Phi^j \tag{3.18}$$

where NT is the series truncation order and a_j^n are the POD coefficients.[2] In other terms, NT represents the number of snapshots (concentration fields) available. Moreover, within the Eq. (3.18), the term $a_j^n \in \mathbf{A} \in \mathbb{R}^{NT \times NT}$ is

[2] In the notation adopted here, superscript symbols refer to the columns and subscripts to the rows.

associated to a time-dependent matrix, whereas $\Phi^j \in \mathbb{R}^{NC\times 1}$ is linked to the space, being $NC = NX \times NZ$ the collocation points number used. POD coefficients a_j^n and modes Φ^j have to be determined.

Arranging C for NT snapshots as:

$$\mathbf{C} = \begin{bmatrix} C^1 & C^2 & \cdots & C^{NT} \end{bmatrix} , \tag{3.19}$$

a symmetric matrix $\mathbf{B} = \mathbf{C}^T\mathbf{C}$ (autocovariance matrix) can be defined. Due to symmetry, the corresponding rearranged eigenvalues λ_i satisfy the relation $\lambda^1 > \lambda^2 > \cdots > \lambda^{NT} = 0$. As a result, these eigenvalues are given by the solution of the following equation:

$$\mathbf{B}\mathbf{a}^i = \lambda^i \mathbf{a}^i , \tag{3.20}$$

being $\mathbf{a}^i$ the corresponding eigenvectors, which can be stored in a matrix as follows:

$$\mathbf{A} = \begin{bmatrix} \mathbf{a^1} & \mathbf{a^2} & \ldots & \mathbf{a}^{NT} \end{bmatrix} . \tag{3.21}$$

Then, orthogonal POD modes are given by:

$$\Phi_i = \frac{\sum_{n=1}^{NT} \mathbf{a}_n^i \mathbf{C}^n}{|| \sum_{n=1}^{NT} \mathbf{a}_n^i \mathbf{C}^n ||}, \quad i = 1, \ldots, NT \tag{3.22}$$

and can be rearranged in the matrix $\mathbf{\Psi}$, which is also orthogonal, as:

$$\mathbf{\Psi} = \begin{bmatrix} \Phi^1 & \Phi^2 & \ldots & \Phi^{NT} \end{bmatrix} . \tag{3.23}$$

For the snapshot n, POD coefficients $\mathbf{a}^i$ are given by:

$$\mathbf{a}^n = \mathbf{\Psi}^T \mathbf{C}^n \tag{3.24}$$

and finally, a snapshot is reconstructed as:

$$\mathbf{C}^n = \mathbf{\Psi}\mathbf{a}^n = \sum_{i=1}^{NT} a_i^n \Phi^i . \tag{3.25}$$

It can be shown that there are (at least) two equivalent ways to build the POD modes (Golub and Van Loan, 2012). The first consist into compute the eigenvalues of the covariance matrix. The latter and more stable one, which is the one we use, consists into find the Singular Value Decomposition (SVD) of the matrix of snapshots $\mathbf{C}$.

Following these steps, we will analyse three different regimes corresponding to low ($Ra = 5 \times 10^2$), intermediate ($Ra = 2 \times 10^3$) and high ($Ra = 16 \times 10^3$) Rayleigh numbers. In Fig. 3.11, the flow configurations considered are summarized.

3.4.3 POD Results

We provide a qualitative and a quantitative analysis of the flow features. Moreover, we draw some conclusions for possible reduced order model development.

Qualitative analysis A snapshot of the first simulation considered ($Ra = 5 \times 10^2$) is reported in Fig. 3.11a. After an initial transition, the system undergoes a steady state, when the Nusselt number is nearly constant. Therefore, it can be well described by a 1^{st}-order model, due the time-invariance of the concentration field.

The second regime investigated ($Ra = 2 \times 10^3$) is well approximated using a reduced number of modes. Indeed, the boundary layer thickness is quite large compared to the domain height, but secondary instabilities arise. In Fig. 3.12, the instantaneous field approximations realized employing $k = 5$, 10 and 20 modes are reported in panels a), b) and c) respectively. The corresponding isocontours are plotted on the right column of Fig. 3.12. In this case, we observe that the description provided using 20 modes is qualitatively accurate. However, important differences in the secondary instabilities are identifiable, especially in the nearby of the horizontal walls.

Finally, we consider the system with $Ra = 16 \times 10^3$ and the flow configuration in this case completely changed with respect to previous regimes. The boundary layer thickness decreases and a large number of modes is

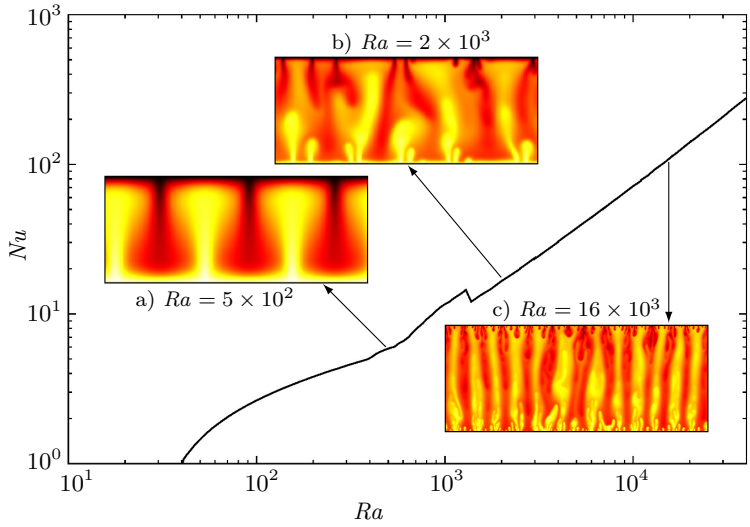

FIGURE 3.11 – Main panel) Nusselt number Nu as a function of the Rayleigh number Ra in the isotropic case ($\gamma = 1$). The scaling is linear for high-Ra, when the megaplumes dominate the domain bulk. Insets a-c) the flow structure at low ($Ra = 5 \times 10^2$), intermediate ($Ra = 2 \times 10^3$) and high ($Ra = 16 \times 10^3$) Rayleigh numbers is represented. Three distinct regimes are clearly visible, as discussed in Sec. 3.3.

required in order to describe the system in an accurate way. In Fig. 3.13 for instance, even with 20 modes the smallest structures are not well described. This definitely represents a big issue, indeed these newborn, small plumes fulfill a key role in the solute dissolution process, and a more accurate representation is required.

Quantitative analysis Following the approach adopted from Puragliesi and Leriche (2012), we quantify the number of modes necessary to describe the system with the aid of a cumulative energy indicator (e_k) rather than the global Nusselt number used by Wen et al. (2012). In particular, the

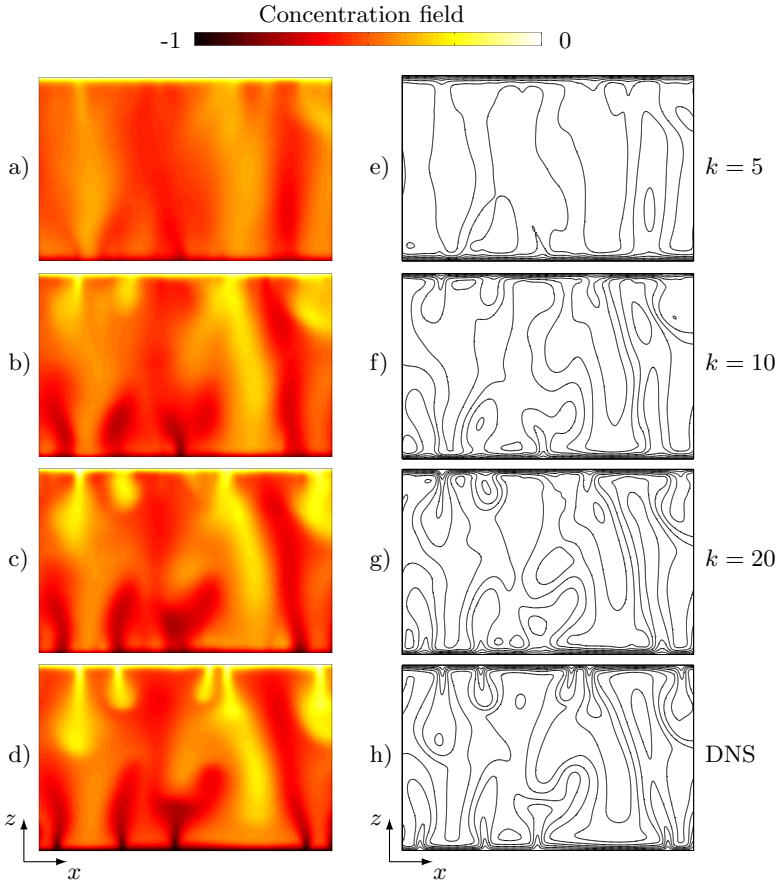

FIGURE 3.12 – Concentration field for $Ra = 2 \times 10^3$ and $L = \pi$. Snapshot of the concentration field (panels a-d) and the corresponding concentration contours (panels e-h), computed at the same time and with different mode numbers, are plotted. Only the first half of the domain is shown ($0 < x < \pi/2$). In this case, a good qualitative description of the system is obtained with 20 modes.

cumulative energy, which is defined as

$$e_k = \frac{1}{E}\sum_{i=1}^{k}\lambda_i \ , \tag{3.26}$$

being $E = \sum_{i=1}^{N}\lambda_i$, is a normalized energy and allows us a straightforward identification of the most energetic and dominant modes. Further information about the goodness of the reduced order model are provided by the normalized eigenvalues (λ_k/E). In Fig. 3.14 results are shown for the three simulations considered.

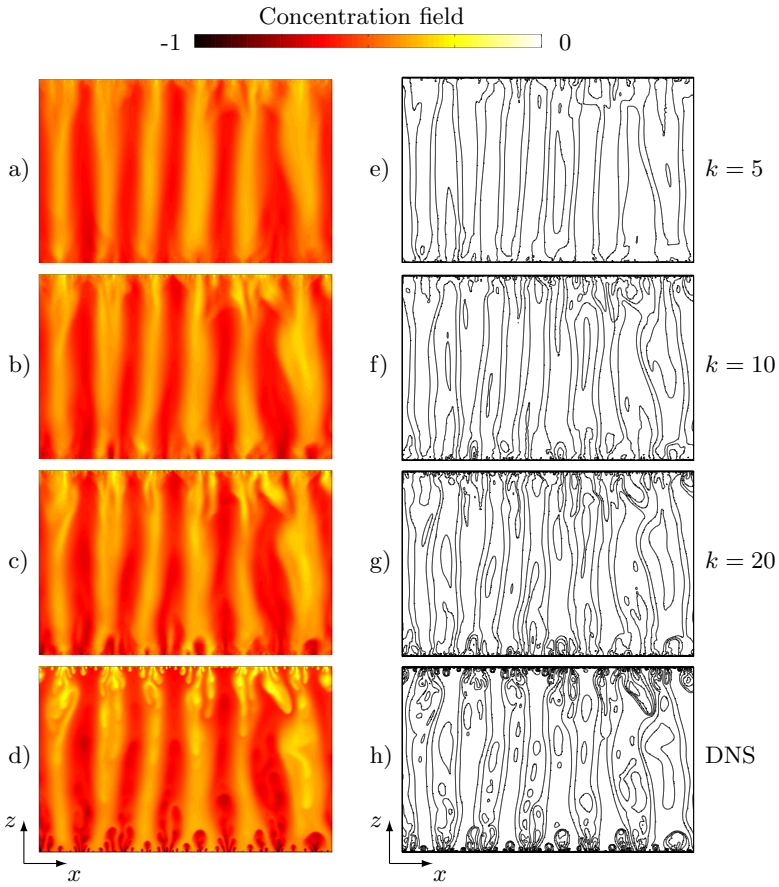

FIGURE 3.13 – Concentration field for $Ra = 16 \times 10^3$ and $L = \pi$. Snapshot of the concentration field (panels a-d) and the corresponding concentration contours (panels e-h), computed at the same time and with different mode numbers, are plotted. Only the first half of the domain is shown $(0 < x < \pi/2)$. In this case 20 modes are not sufficient to provide a good approximation of the system, which differs, especially in the nearby of the boundaries.

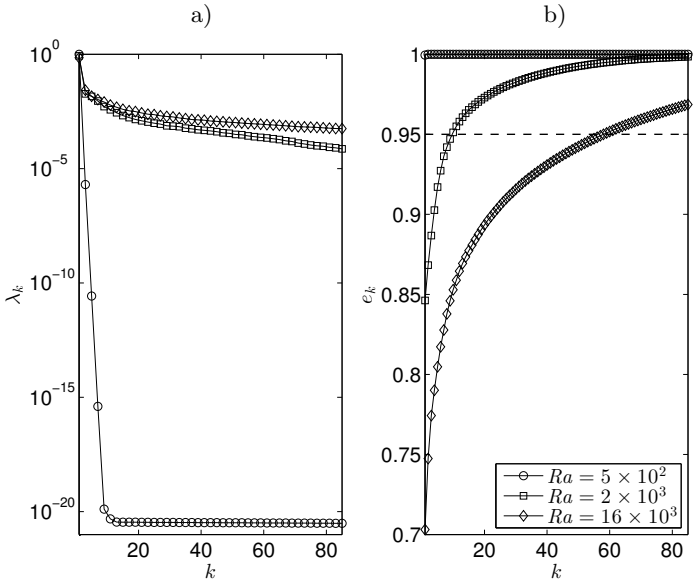

FIGURE 3.14 – Quantitative estimate of the numbers of modes required to reproduce the main features of the flow at low, intermediate and high regimes. Panel a) Relative value of the eigenvalue λ_k corresponding to the mode k. Panel b) cumulative energy e_k plotted as a function of the number of modes considered.

First, we observe that for low values of the Rayleigh number ($Ra = 5{\times}10^2$), the decay of the singular values is rapid (Fig. 3.14a), and an attempt to build a ROM is feasible. However, at higher regimes ($Ra = 2 \times 10^3$ and $Ra = 16 \times 10^3$) the decay is much more slower. For instance, if we can consider as energy limit $e_l = 0.95$, we observe that it can be reached with $k = 1$, 10 and 58 modes for $Ra = 5 \times 10^2$, 2×10^3 and 16×10^3 respectively (Fig. 3.14b).

According to the conditions introduced in Sec. 3.4.1, we end up concluding that, in the current configuration, reduced order modelling description is suitable only at low regimes. Indeed, POD is one of the simplest decompositions available, and it is suitable for the analysis of linear equations. The problem considered here is instead not fully linear, due to the advective term included in Eq. (3.12). Nevertheless, POD analysis remains a useful tool that can provide information about the flow topology ans simplify the main dynamics occurring in porous media convection.

3.5 Relationship between the two-sided and the one-sided cell

To analyse the physics of concentration-driven CO_2 dissolution in geological reservoirs, the adoption of the so-called one-sided cell is perhaps more

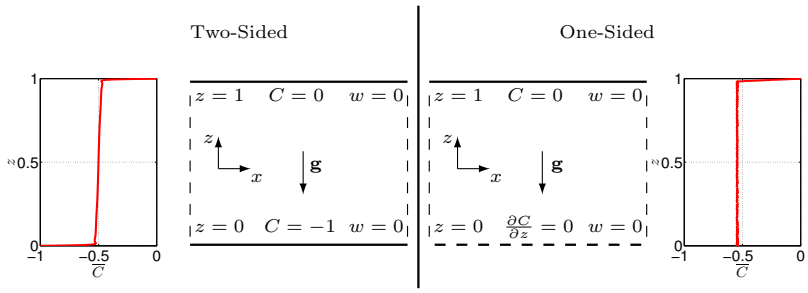

FIGURE 3.15 – Sketch of the computational domain in the two-sided (left panel) and in the one-sided (right panel) cell. The two-sided cell (left) has physical boundaries, characterized by an imposed value of the solute concentration, in the vertical direction (upper and lower horizontal solid lines), whereas it has periodic boundaries in the horizontal direction (left and right vertical dashed lines). The one-sided cell (right) is instead characterized by a zero-flux boundary condition at the lower boundary (impenetrable and no-flux condition).

indicated compared to the two-sided cell discussed above. Differently from the two-sided cell, in the one-sided cell convection occurs only from the upper boundary whereas the lower boundary is an impenetrable and no-flux boundary. Details on the different boundary conditions characterizing the two-sided and the one-sided cells are given in Fig. 3.15.

In literature, the transient solute dynamics in the one-sided cell has been recently analysed experimentally (Slim et al., 2013) and numerically (Hidalgo et al., 2012; Hewitt et al., 2013a; Slim, 2014) for isotropic porous media. The characteristic dynamics of the one-sided cell is the following. After injection of solute from the upper boundary, diffusion dominates until fingers become strong enough to trigger vertical convective motions. Fingers become stronger and stronger in time, and merge into large and columnar plumes (megaplumes) that extend vertically over the entire domain. Once megaplumes reach the bottom boundary, the domain starts filling with dense solute. This is the final (and longer) stage of the entire process of solute convection, and is usually called the "shutdown regime". As already discussed for the case of isotropic porous media (Hewitt et al., 2013a; Neufeld et al., 2010), during the shutdown regime a precise connection between the two-sided and the one-sided cell can be established. In the following, we will try to extend this link also in case of anisotropic porous media.

The one-sided cell corresponds to one half of the two-sided cell. In particular, it is characterized by a cell height and by a density difference both of which is one-half of the corresponding value of the two-sided cell. As a consequence, indicating with Ra_1 and Ra_2 the Rayleigh-Darcy numbers of the one-sided cell and of the two-sided cell respectively, we have $Ra_2 = 4\,Ra_1$.

We start from the theoretical box model proposed by Hewitt et al. (2013a) and we try to extend it to the case of anisotropic porous media.

The solute flux in the one-sided cell is conveniently defined as

$$F(t) = \frac{1}{L}\int_0^L \left.\frac{\partial C(x,t)}{\partial z}\right|_{z=1} dx \ , \tag{3.27}$$

while the mean concentration at time t and at the vertical position z is

$$\overline{C}(z,t) = \frac{1}{L}\int_0^L C(z,t)dx \ . \tag{3.28}$$

Following Hewitt et al. (2013a), we assume that: i) far from the walls the averaged concentration profile is uniform over the domain height $\overline{C}(z,t) \approx \overline{C}(t) = \vartheta(t)$; ii) during the shutdown regime, the fundamental flow structures are those that characterize the steady-state two-sided system (protoplumes and megaplumes); iii) the Rayleigh-Darcy number in the one-sided domain, defined as $Ra = gH^* k_v \Delta\rho^*/(\mu\Phi D)$, depends on the actual density difference $\Delta\rho^*$ existing between the top of the domain and a generic point outside the boundary layer. Under the above hypotheses, it is possible to define a time-dependent Rayleigh-Darcy number, $Ra(t) = Ra_0\,|\vartheta(t)|$, where Ra_0 is computed based on the initial density difference.

We consider the time-dependent three dimensional advection-diffusion equation

$$\frac{\partial C}{\partial t} + \mathbf{u}\cdot\nabla C = \frac{1}{Ra_0}\left[\gamma\left(\frac{\partial^2 C}{\partial x^2} + \frac{\partial^2 C}{\partial y^2}\right) + \frac{\partial^2 C}{\partial z^2}\right] \tag{3.29}$$

and we integrate it over the whole domain. Imposing the boundary conditions

$$w = 0 \quad , \quad \frac{\partial C}{\partial z} = 0 \quad \text{on} \quad z = 0 \ , \tag{3.30}$$

$$w = 0 \quad , \quad C = 0 \quad \text{on} \quad z = 1 \tag{3.31}$$

and using the Stokes theorem and the definition (3.28), we obtain

$$\frac{\partial}{\partial t}\int_0^1 \overline{C}(z,t)\ dz = \frac{1}{Ra_0}\frac{1}{L}\int_0^L \left.\frac{\partial C}{\partial z}\right|_{z=1} dx \ . \tag{3.32}$$

For an alternative derivation of Eq. (3.32) see Sec. 4.4. Assuming that the averaged concentration profile is uniform over the vertical direction z, we have $\overline{C}(z,t) \approx \vartheta(t)$. As a result, the left-hand side of Eq. (3.32) reduces to

$$\frac{\partial}{\partial t}\int_0^1 \overline{C}(z,t)\ dz \approx \frac{\partial}{\partial t}\int_0^1 \vartheta(t)\ dz = \frac{\partial\vartheta(t)}{\partial t} \ . \tag{3.33}$$

Note that the same result can be obtained also considering two lateral impermeable walls (in the x direction) instead of two periodic boundaries.

According to the Nusselt number definition adopted for the one-sided domain (see Appendix 3.A), we finally obtain the evolution in time of the solute concentration:

$$\frac{d\vartheta(t)}{dt} = \frac{Nu(t)}{Ra_0}|\vartheta(t)| \ . \tag{3.34}$$

To resolve Eq. (3.34) we need an estimate for $Nu(t)$ in case of anisotropic porous media. This is accomplished here using our previous predictions (correlation (3.15)) with the modified Rayleigh number $Ra = 4\,Ra_0$ (to switch from the one-sided to the two-sided cell).

By imposing the initial condition $\vartheta(t_0 = 0) = -1$, we obtain the dynamic behaviour of the mean concentration profile:

$$\vartheta(t) = \frac{\beta}{4\,Ra_0\,\gamma^n\alpha}\left[1 - \left(1 + \frac{\beta}{4\,Ra_0\,\gamma^n\alpha}\right)\exp\left(\frac{\beta}{Ra_0}t\right)\right]^{-1} \ . \tag{3.35}$$

Upon definition of $\varepsilon = \beta/(4\,Ra_0\,\gamma^n\alpha)$, we have

$$\vartheta(t) = \varepsilon\Big[1 - \big(1+\varepsilon\big)\exp\big(4\alpha\gamma^n\varepsilon t\big)\Big]^{-1}. \tag{3.36}$$

In the limit of large Ra, $\varepsilon \to 0$ and we finally get the following expression for the dynamic behaviour of the mean concentration profile and of the vertical flux as a function of the permeability ratio γ:

$$\vartheta(\gamma, t) \approx \frac{-1}{1 + 4\alpha\gamma^n t} \ , \tag{3.37}$$

$$F(\gamma, t) \approx \frac{4\alpha\gamma^n\,Ra_0}{\Big[1 + 4\alpha\gamma^n t\Big]^2} \ . \tag{3.38}$$

Note that, for $Ra = 10^4$, the difference between the prediction given by Eq. (3.36) and by Eq. (3.37) is always below 1% of the maximum value of $\vartheta(t)$, which makes the approximation $\varepsilon \to 0$ reasonable for solute convection in real-scale reservoirs.

The behaviour of $F(\gamma, t)$ for the different values of γ considered in this study is shown in Fig. 3.16a. At the beginning, $F(\gamma, t)$ is larger for smaller γ, indicating that the vertical flux of solute increases for decreasing γ. At later stages, we observe a crossover between the different curves occurring at $t = \tilde{t}$. By matching the value of $F(\gamma, t)$ for two different values of γ (here indicated by γ_1 and γ_2) we obtain the value of the crossover time $\tilde{t} = (\gamma_1\gamma_2)^{-n/2}/4\alpha$, which falls in the range $\tilde{t} = [30; 35]$ and is only slightly sensitive to the value of γ.

From the knowledge of the instantaneous solute flux $F(\gamma, t)$ we can explicitly compute, for a given γ, the total amount of solute $\mathcal{F}(\gamma, t)$ dissolved in the entire domain during the shutdown regime:

$$\mathcal{F}(\gamma, t) = \frac{4\alpha\gamma^n t}{1 + 4\alpha\gamma^n t}\,Ra_0 \, . \tag{3.39}$$

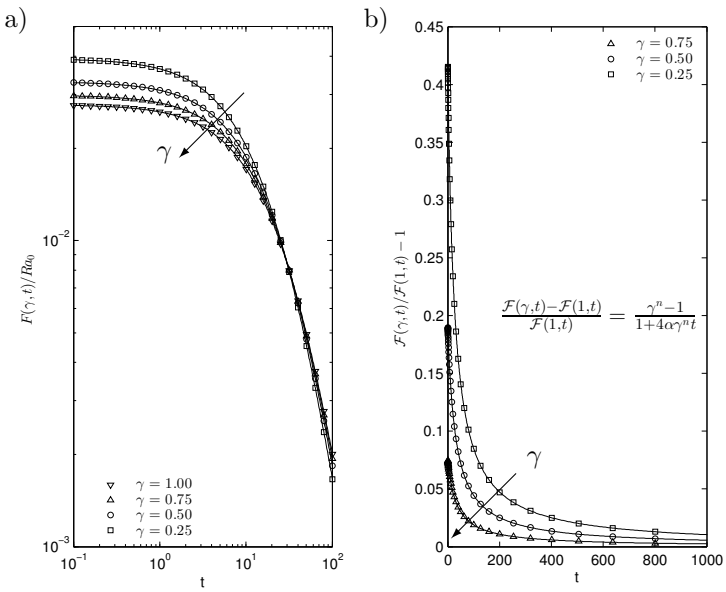

FIGURE 3.16 – Panel a) dynamic behaviour of the vertical solute flux ($F(\gamma,t)/\,Ra_0$, see also Eq. (3.38)) computed for a one-sided domain for different values of γ. Panel b) dynamic behaviour of the normalized amount of solute (Eq. (3.39)) for different values of γ.

In particular, we consider the dynamic behaviour of the normalized difference $(\mathcal{F}(\gamma,t) - \mathcal{F}(1,t))/(\mathcal{F}(1,t))$ between the solute dissolved for $\gamma \neq 1$ and that dissolved for $\gamma = 1$. Results, which are shown in Fig. 3.16b, indicate that during the initial transient the quantity of solute dissolved for $\gamma = 0.25$ can be 40% larger than that for $\gamma = 1$. This suggests that, for finite times, the amount of solute that can be efficiently dissolved in real reservoirs ($\gamma \neq 1$) is considerably larger compared to the uniform permeability case ($\gamma = 1$). As expected, in the long-term limit we have $\mathcal{F}(t \to +\infty) \to Ra_0$, which means that for extremely long times the amount of dissolved solute depends only on the available volume (Ra_0) but not on γ. Note however that this result is not in contrast with the previous observation that for finite times ($t^* < 10^2$ years) γ has a strong impact on the amount of dissolved solute.

3.6 Conclusions and future developments

Solute convection in porous media at high Rayleigh-Darcy number Ra is characterized by complex macroscopic phenomena (viscous fingering, megaplumes) that are difficult to model and to predict. Further complications arise when the porous medium is anisotropic. This is the case of realistic

sedimentary rock reservoirs, which can be modelled as porous media with a vertical-to-horizontal permeability ratio $\gamma = k_v/k_h$ smaller than unity.

In this chapter we focused exactly on the effect of γ (with $\gamma < 1$) on the solute convection in a two-dimensional saturated porous medium. We started considering the case of the so-called two-sided domain, in which convective transport occurs between a lighter layer (lower boundary) and a heavier layer (upper boundary). We performed simulations for a range of Rayleigh-Darcy numbers Ra ranging from 50 to 5×10^4. We have characterized the flow dynamics in terms of protoplumes (small plumes emerging from the boundary) and megaplumes (generated by the coalescence of protoplumes). Flow field statistics obtained for different Ra and different γ have been compared to discuss the role of the different parameters on the overall transport efficiency of the solute. We have shown that, for $\gamma < 1$, the vertical convective flux of solute increases significantly (up to 40%, for the range of γ examined here). We have also linked this phenomenon to the modification of the flow topology: increasing k_h (i.e. decreasing γ) increases the horizontal velocity gradient of the satured fluid and in turn enhances the solute vertical transport.

We used proper orthogonal decomposition to investigate the feasibility of reduced order model at different regimes. This analysis is motivated by the large computational effort, i.e. high-resolved grids, required to accurately solve convective transport in porous layers. Our results show that, in the current configuration, reduced order modelling description is suitable only at low regimes.

We finally used our results on the two-sided configuration to introduce and discuss the solute dynamics in the so-called one-sided configuration (where convection occurs only away from the upper boundary). This configuration is perhaps more related to the physics of the concentration driven CO_2 dissolution process. We found that, for realistic CO_2 dumping times ($t^* < 10^2$ years), the amount of CO_2 that can be efficiently dissolved in sedimentary rock reservoirs characterized by $\gamma < 1$ is larger than that dissolved in case of $\gamma = 1$ (isotropic porous medium). This result opens new intriguing perspectives on the efficiency of long-term geological CO_2 storage.

3.6.1 Implications for CO2 sequestration

In the following, we will try to put the results presented above in the context of CO_2 sequestration in real reservoirs. We consider the case of Sleipner site, in the North Sea. We assume a porous medium with uniform porosity $\Phi = 0.3$, vertical permeability $k_v = 3 \times 10^{-12}$ m^2 and a layer depth $H^* = 20$ m (Neufeld et al., 2010; Bickle et al., 2007). The thermophysical properties of the fluid are those of CO_2+brine at a depth of 1 km (typical reservoir location). In particular, Pau et al. (2010) suggested a top-to-bottom density difference $\Delta\rho^* = 10.45$ kg/m^3, viscosity $\mu = 595 \times 10^{-6}$ Pa×s and diffusivity $D = 2 \times 10^{-9}$ m^2/s. The resulting Rayleigh-Darcy number is $Ra \approx 17 \times 10^3$.

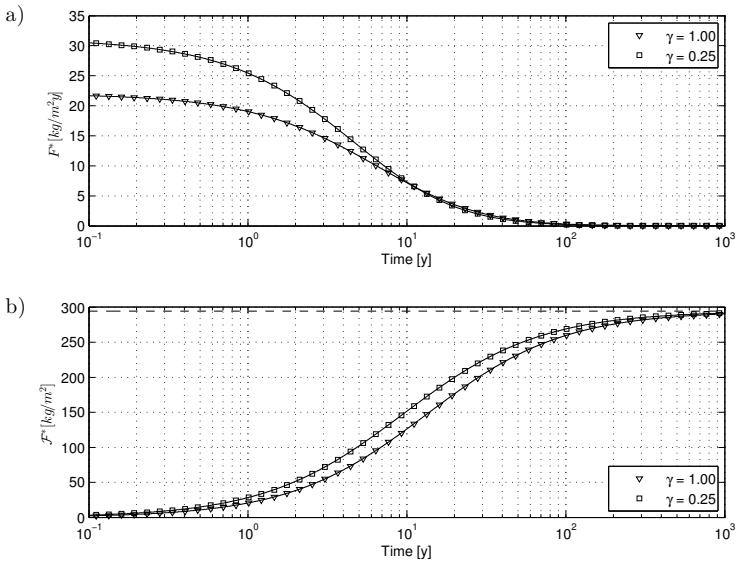

FIGURE 3.17 – CO2 convective flux (a) and total CO2 dissolved (b) in time. Dashed line represents the maximum amount of CO2 dissoluble per unit area.

The free-fall buoyancy velocity and the convective time scale are $W^* \approx 16.3$ m/y and $\hat{t} = \Phi H^*/W^* \approx 0.37$ y respectively.

From Eq. (3.38), we derive the dimensional value of the convective flux F^*, in terms of the physical time t^* and anisotropic permeability ratio γ:

$$F^*(\gamma, t^*) = \frac{4\alpha\gamma^n \hat{t}}{\left[\hat{t} + 4\alpha\gamma^n t^*\right]^2} H^* \Phi C_s^* \tag{3.40}$$

The total amount of CO_2 dissolved during the shutdown regime, obtained from dimensionless Eq. (3.39), is

$$\mathcal{F}^*(\gamma, t^*) = \frac{4\alpha\gamma^n t^*}{\hat{t} + 4\alpha\gamma^n t^*} H^* \Phi C_s^* \ . \tag{3.41}$$

In Fig. 3.17 we report, for the present example, the convective fluxes and the dissolved CO_2 for the two extreme cases of $\gamma = 1$ (isotropic medium) and $\gamma = 0.25$. Results clearly show that, up to the critical time $\widetilde{t}^* \approx 11.2$ y, the convective flux of CO_2 (Fig. 3.17a) is definitely larger for $\gamma = 0.25$ than for $\gamma = 1$ (isotropic case). This reflects into a larger amount of dissolved CO_2 for $t^* < 10^3$ (Fig. 3.17b). Alternatively, we might say that, for a given amount of CO_2 per unit area $\overline{\mathcal{F}^*}$ to be injected beneath the earth surface, the dissolution time for safety CO_2 storage is definitely shorter when $\gamma < 1$. To put some numbers, if $\overline{\mathcal{F}^*} = 150\ kg/m^2$, the dissolution times are $t^* = 10\ y$ for $\gamma = 0.25$ and $t^* = 15\ y$ for $\gamma = 1$. Note also that,

for extremely long times ($t^* \to \infty$), the amount of dissolved CO_2, which is independent of γ, is roughly 3×10^2 kg/m^2. This represents indeed a theoretical estimate of the overall storage capability of the reservoir.

3.A Appendix

In this section we report some details on the numerical methodology employed in the present study.

3.A.1 Numerical approach

We used a pseudo-spectral method, which transforms field variables in the wavenumber space through a Discrete Fourier Transform in the horizontal direction and a Chebyshev expansion in the wall-normal direction (see Appendix A). Equations (3.10)-(3.12) are rewritten in vectorial form as:

$$\mathbf{u} = -\nabla P + \mathbf{k}C \ , \tag{3.42}$$

$$\nabla \cdot \mathbf{u} = 0 \ , \tag{3.43}$$

$$\frac{DC}{Dt} = \frac{1}{Ra}\left(\gamma \nabla_H^2 C + \frac{\partial^2 C}{\partial z^2}\right) \ , \tag{3.44}$$

with $\mathbf{k}$ the unit vector in the vertical direction and $\nabla_H^2 = \partial^2/\partial x^2 + \partial^2/\partial y^2$. Taking twice the curl of Eq. (3.42) and using Eq. (3.43) it is possible to compute the wall-normal velocity $\hat{w}$ by solving a second order Helmoltz equation in the wavenumber space (k_x, k_y):

$$\left[\frac{\partial^2}{\partial z^2} - \left(k_x^2 + k_y^2\right)\right]\hat{w} = -\left(k_x^2 + k_y^2\right)C \ . \tag{3.45}$$

Once $\hat{w}$ is available, $\hat{u}$ and $\hat{v}$ can be determined as:

$$\hat{u} = i\frac{k_x}{k_x^2 + k_y^2}\frac{\partial \hat{w}}{\partial z} \ , \tag{3.46}$$

$$\hat{v} = i\frac{k_y}{k_x^2 + k_y^2}\frac{\partial \hat{w}}{\partial z} \ . \tag{3.47}$$

Equation (3.44) is then discretized in time using an Adams-Bashforth explicit method for the non linear term $S = \mathbf{u} \cdot \nabla C$ and a Crank-Nicholson implicit method for the diffusive term:

$$\frac{\hat{C}^{n+1} - \hat{C}^n}{\Delta t} = \frac{3}{2}\hat{S}^n - \frac{1}{2}\hat{S}^{n-1} + \frac{1}{2\,Ra}\left(\gamma \nabla_H^2 + \frac{\partial^2}{\partial z^2}\right)(\hat{C}^{n+1} - \hat{C}^n) \ . \tag{3.48}$$

Due to the above mentioned algorithms, the numerical scheme adopted has a second order accuracy in time. The computational time step Δt has been chosen to fulfill the CFL condition and ranges between $\Delta t = 5 \times 10^{-5}$ ($Ra = 5 \times 10^4$ and $\gamma = 0.25$) and $\Delta t = 2 \times 10^{-3}$ ($Ra = 2 \times 10^3$ and $\gamma = 1$).

Transforming Eq. (3.48) in the wavenumber space, the concentration $\hat{C}$ can be obtained by solving the second order Helmoltz equation:

$$\left(\frac{\partial^2}{\partial z^2} - \frac{1 + \gamma\delta(k_x^2 + k_y^2)}{\delta}\right)\hat{C}^{n+1} = -\frac{\hat{H}}{\delta} \ , \tag{3.49}$$

where $\delta = \Delta t/(2\,Ra)$ and

$$\hat{H} = \delta\left(\frac{\partial^2}{\partial z^2} - \frac{1 + \gamma\delta(k_x^2 + k_y^2)}{\delta}\right)\hat{C}^n + \delta\,Ra\big(3\hat{S}^n - \hat{S}^{n-1}\big) \ . \tag{3.50}$$

Further details on the numerical scheme and on the spatial discretization adopted are reported in Appendix A.

The initial condition of the present simulations consists of a perturbed linear concentration profile

$$C_0(z) = C(0) + \big[C(1) - C(0)\big]z + \xi \tag{3.51}$$

where $C(0)$ and $C(1)$ are the values of the concentration at the bottom and top walls, whereas ξ is a random number with amplitude $|\xi| < 2 \times 10^{-3}|C(1) - C(0)|$.

Following Wen et al. (2013), and considering that the horizontal scales become thinner in high-Ra convection, we ran simulations on a domain whose aspect ratio $\Gamma = L/H$ was reduced from 2π to $\pi/4$ for increasing Ra. The resulting domain was discretized in space using up to 8192×1025 nodes in the x and z directions for $Ra = 5 \times 10^4$. We finally checked that the steady state solution was independent of the spatial resolution (grid independence) and of the aspect ratio Γ.

3.A.2 Nusselt number calculation

The Nusselt number Nu, which represents the non-dimensional flux of heat or solute through the boundaries of a two-sided domain, is computed as

$$\overline{Nu}(t) = \frac{1}{2L}\int_0^L \left(\left.\frac{\partial C(x,t)}{\partial z}\right|_{z=0} + \left.\frac{\partial C(x,t)}{\partial z}\right|_{z=1}\right) dx \ . \tag{3.52}$$

Note that the Nusselt number, averaged in space over the horizontal direction x, is a function of time. However, after an initial transient t_i, the simulation reaches a steady state condition (whose final instant is t_f), where the Nusselt number fluctuates around an asymptotic value $\langle Nu \rangle$ evaluated as

$$\langle Nu \rangle = \frac{1}{t_f - t_i}\int_{t_i}^{t_f} \overline{Nu}(t)\ dt \ . \tag{3.53}$$

Throughout this chapter, $\langle Nu \rangle$ is indicated as Nu for ease of reading. Statistics are averaged over a time window of $150 \times \hat{t}$, where $\hat{t}$ is the convective time scale $\hat{t} = \Phi H^*/W^*$ (with Φ the porosity, H^* the domain height and W^* the freefall buoyancy velocity). Note that for the one-sided configuration we defined the time-dependent Nusselt number $Nu(t)$ following Hewitt et al. (2013a) as

$$Nu(t) = \frac{F(t)}{|\vartheta(t)|} \ , \tag{3.54}$$

where $F(t)$ is the solute flux and $\vartheta(t)$ is the concentration difference.

4

Modelling convection regimes from onset to shutdown

Part of the results presented in this chapter have been published under the title "Dissolution in anisotropic porous media: modelling convection regimes from onset to shutdown" (De Paoli et al., 2017) in the journal *Physics of Fluids*.

4.1 Introduction

When a heavier fluid is injected at the top of a porous slab, it is driven downward by gravity. After an initial diffusion transport, viscous fingers appear and merge into convective plumes, whose strength and persistence depend on the magnitude of the driving force. If the bottom boundary is impermeable, the porous medium is eventually filled up by the liquid. The major proportion of this process is characterized by convective phenomena, from onset (Horton and Rogers Jr, 1945; Lapwood, 1948) (when convective overturning starts) to shutdown (when the filling process is being completed and convection cannot exist anymore). The dynamics described above has a fundamental importance in geological CO_2 sequestration, since it faithfully mimics the process of liquid CO_2 injection/transport in saline aquifers (Bolster, 2014; Szulczewski et al., 2013). The injection of CO_2 is realized at depths between 800 and 3000 m, where CO_2 exists at a supercritical (liquid) state (Huppert and Neufeld, 2014). At the beginning, CO_2 is lighter than brine and rises up until reaching an impermeable cap rock that stops the rising motion and favours a slower horizontal spreading. Under these conditions, CO_2 has time to dissolve into the brine thereby increasing the density of brine. This new layer of dense saturated brine becomes rapidly unstable, so to foster the downward transport and the consequent deposition of CO_2 at the bottom of the geological reservoir.

Therefore, the problem of CO_2-brine convection (solutal convection) described above shares some similarities with the classical thermal convection system (in a porous medium) characterized by two impermeable walls with prescribed temperature (Rayleigh-Bénard convection). However, it does display a fundamental difference. Classical Rayleigh-Bénard convection supports the existence of a statistically steady state, whose dynamics depends only on the value of the Rayleigh-Darcy number (Ra) (Otero et al., 2004; Hewitt et al., 2012; De Paoli et al., 2016). Solutal convection has instead a dynamics that is time-dependent and is characterized by a sequence of different regimes changing in time. The dynamics develops from the upper boundary, and the size of the system (or, in other words, the Rayleigh-Darcy number Ra) is not influential until flow structures reach the opposite boundary. After this stage, the system starts depending on Ra. A comprehensive description of the above mentioned solutal convection in porous medium has been recently proposed by Slim (2014). Through the use of accurate numerical simulations, Slim (2014) extended previous experimental (Neufeld et al., 2010; Backhaus et al., 2011) and numerical (Pau et al., 2010; Hewitt et al., 2013a; Hidalgo et al., 2012) results found in literature and was finally able to provide a unified picture of the entire dynamics for solute convection in an isotropic porous medium.

However, one important aspect for geological CO_2 sequestration is rock anisotropy. Sedimentary rocks, which are composed by the subsequent accumulation of horizontal layers, are characterized by an horizontal permeability, k_h, that is larger compared to the vertical one, k_v. Hence the vertical-to-horizontal permeability ratio, $\gamma = k_v/k_h$, is typically $\gamma < 1$. Despite this fact, a larger proportion of the studies in this field consider the case of an isotropic porous medium ($\gamma = 1$). There are only few works that focus on solutal convection in an anisotropic porous slab (see Cheng et al. (2012); Green and Ennis-King (2014) among the others). However, these studies were usually performed at lower Ra ($Ra < 10^4$) and considered only the initial transient dynamics of the flow (they did not provide a detailed description of the entire dissolution process dynamics). Our aim here is to fill this gap by performing numerical simulations at large Ra and $\gamma < 1$ to provide for the first time a unifying picture of solute dynamics in realistic geological reservoirs.

The present chapter is organized as follows: in Sec. 4.2 the physical and numerical setup will be presented and discussed. In Sec. 4.3 we will present the main results obtained from our simulations. We will characterize the entire solute dynamics, from the initial stages dominated by diffusion, up to the final shutdown stage. We will also provide parametrizations and suitable correlations for each stage of the solute dynamics. In Sec. 4.4, we will use our numerical results to develop a simple phenomenological model that provides a good estimate of the time required by the solute to fill the reservoir (shutdown time). In Sec. 4.5, we will implement in a large-scale model the effect on anisotropy, in order to identify the effects of

the permeability ratio on the CO_2 buoyant currents. We will finally draw conclusions and outline future developments.

4.2 Methodology

We consider a porous medium in a two dimensional domain, where x^* is the horizontal direction and z^* the vertical direction. The porous medium, which is filled with a CO_2+brine solution (solute), is characterized by a uniform porosity Φ (fixed parameter between the different simulations) and by different values of the vertical (k_v) to horizontal (k_h) permeability ratio $\gamma = k_v/k_h$. To represent physical geological situations, we choose $1/2 \leq \gamma \leq 1$ (Ennis-King et al., 2005). At the beginning, the CO_2 concentration is zero everywhere but at the top boundary, where CO_2 is injected. As a consequence, the solute is driven by the composition-induced density difference in the vertical direction (with heavier fluid laying on top of lighter fluid) and is governed by a modified version of the Darcy's law written under the assumptions of the Oberbeck-Boussinesq approximation (Landman and Schotting, 2007). A natural reference velocity scale for this flow is the free-fall buoyancy velocity, $W^* = gk_v\Delta\rho^*/\mu$, with μ the fluid viscosity, g the acceleration due to gravity and $\Delta\rho^*$ the initial top-to-bottom density difference of the solute. The corresponding reference length scale is $h^* = \Phi D/W^*$, with D the solute diffusivity. To account for the effect of anisotropy, we use different velocity/length scales in the vertical and horizontal directions through the introduction of the scaling factor $\sqrt{\gamma}$. As a consequence, variables are made dimensionless as (Cheng et al., 2012):

$$x = \frac{x^*}{h^*/\sqrt{\gamma}} \quad , \quad z = \frac{z^*}{h^*} \quad , \quad u = \frac{u^*}{W^*/\sqrt{\gamma}} \quad , \quad w = \frac{w^*}{W^*} \tag{4.1}$$

$$p = \frac{p^*}{\Delta\rho^* g h^*} \quad , \quad C = \frac{C^*}{C_s^*} \quad , \quad t = \frac{t^*}{\Phi h^*/W^*} \quad , \tag{4.2}$$

where t^* is time, u^* and w^* are the velocities in the horizontal (x^*) and vertical (z^*) directions, whereas p^* and C^* are pressure and solute concentration (with C_s^* the solute concentration at the top boundary). Note that the superscript * is used to represent dimensional quantities. We assume that the solute density is the only physical property that depends on concentration through the equation of state

$$\rho^* = \rho_s^* \left[1 - \frac{\Delta\rho^*}{\rho_s^* C_s^*} \left(C_s^* - C^* \right) \right] , \tag{4.3}$$

with ρ_s^* the density at the top boundary. Using the above scalings, the dynamics of the solute is described by the following set of dimensionless equations:

$$u = -\frac{\partial P}{\partial x} \quad , \quad w = -\frac{\partial P}{\partial z} - C, \tag{4.4}$$

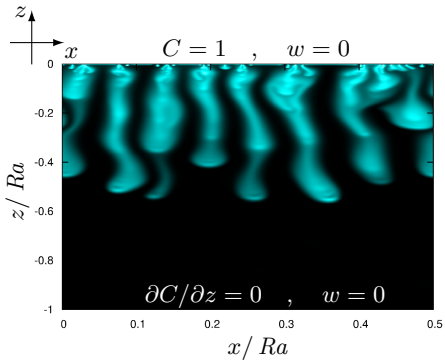

FIGURE 4.1 – Sketch of the computational domain with explicit indication of the boundary conditions (Eqs. (4.7)-(4.8)) employed. The contour map of the solute concentration C at a given time instant t is also shown to provide a flow visualization of the dynamics for the present physical configuration (injection of CO_2 from the upper boundary).

$$\frac{\partial u}{\partial x} + \frac{\partial w}{\partial z} = 0, \tag{4.5}$$

$$\frac{\partial C}{\partial t} + u\frac{\partial C}{\partial x} + w\frac{\partial C}{\partial z} = \gamma\frac{\partial^2 C}{\partial x^2} + \frac{\partial^2 C}{\partial z^2}, \tag{4.6}$$

with $P = p + z(\rho_s^*/\Delta\rho^* - 1)$ the reduced pressure. Boundary conditions for the governing equations are as follows: the top wall is an impermeable boundary characterized by a fixed solute concentration (mimicking the presence of a saturated solution near the top boundary), whereas the bottom boundary is an impermeable boundary for both fluid and solute (i.e. no-flux boundary). Periodicity is applied at the side boundaries (along x). In dimensionless form, these boundary conditions become:

$$w = 0 \quad , \quad C = 1 \quad \text{for} \quad z = 0 \ , \tag{4.7}$$

$$w = 0 \quad , \quad \frac{\partial C}{\partial z} = 0 \quad \text{for} \quad z = -\,Ra \ . \tag{4.8}$$

A sketch of the computational domain together with the indication of the boundary conditions and a contour map of the concentration C at a given time instant is shown in Fig. 4.1.

The main parameter of the simulation is the Rayleigh-Darcy number, which is the ratio of diffusive to convective time scales, defined as

$$Ra = \frac{gH^* k_v \Delta\rho^*}{\mu\Phi D}, \tag{4.9}$$

where H^* represents the domain height. With the proposed scalings, Ra appears only in the boundary conditions (but not in the governing equations)

and can be viewed as a dimensionless layer thickness. This clearly reveals that the value of Ra is not important until plumes impinge on the bottom boundary. Only after plumes impingement the presence of the bottom boundary is perceived by the entire fluid and Ra starts playing a major role on the subsequent dynamics (Slim, 2014). Note that the effect of anisotropy (γ) is explicit only in Eq. (4.6) but it is also present in the other equations through the reference length/velocity scales defined above. In the present study, we obtain $\gamma < 1$ by increasing the horizontal permeability k_h while keeping k_v constant (i.e. keeping the same Ra). Following this strategy, we are able to compare simulations at the same Ra (i.e. same driving force or same domain height), but different γ (i.e. different porous medium).

Governing Eqs. (4.4)-(4.6) have been solved through a pseudo-spectral Chebyshev-Tau method, which makes use of Discrete Fourier Transform in the horizontal direction, and Chebyshev polynomials in vertical direction.

The time step, $\Delta t = 1/2$, has been chosen to ensure stability conditions. The spatial resolution ranges from 2048×513 in the isotropic case, to 8192×1025 in the case of $\gamma = 1/2$. Further details on the numerical method can be found in Appendix A and in Sec. 3.A.1.

4.3 Results

In this section we discuss the results obtained from our numerical simulations of the concentration-driven CO_2 dissolution process in geological reservoirs. As in previous works (Slim, 2014), we assume as initial condition the diffusive concentration profile

$$C(z,t) = 1 + \mathsf{erf}\left(\frac{z}{\sqrt{4t}}\right) \tag{4.10}$$

perturbed with a random noise. In particular, we follow the entire time-dependent dynamics of the flow field for a given Ra number ($Ra = 2 \times 10^4$) and different values of γ ($\gamma = 1$, $3/4$ and $1/2$). The value of Ra is motivated by the physical parameters available for the Sleipner site (North Sea), as discussed in Sec. 3.6.1.

We start our discussion considering the case of an isotropic porous medium ($Ra = 2 \times 10^4$, $\gamma = 1$). We will briefly discuss the different flow regimes observed in the present computation, since some of these observations will be useful in the following while discussing the effects of γ on the solute dynamics.

The entire time-dependent solute dynamics is made of six consecutive regimes. At the beginning, solute transport occurs from the upper boundary only (where CO_2 is injected) and is essentially dominated by solute diffusion: a *diffusion (i)* and a *linear-growth regime (ii)* are here observed. Later, small fingers form, grow, interact and merge into megaplumes so to enter a long transient phase dominated by convection. Three different regimes are now

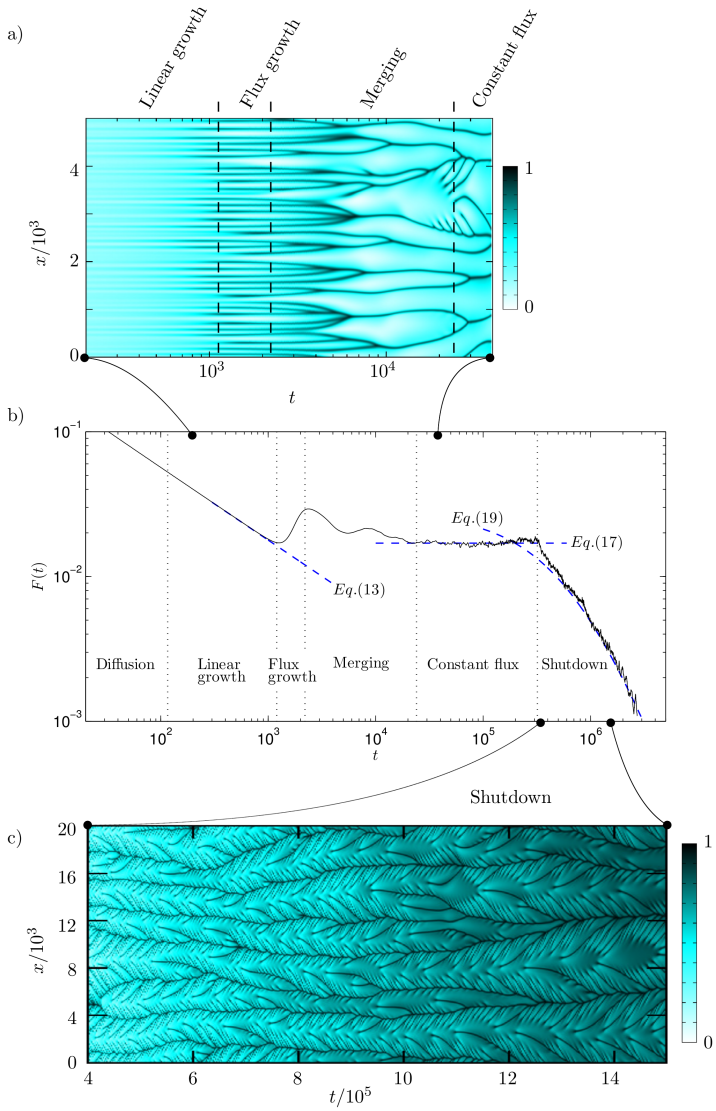

FIGURE 4.2 – Dynamic behaviour of the solute dissolution for $Ra = 2\times10^4$ and $\gamma = 1$. Panel b) Dissolution flux $F(t)$ as a function of time. Solid line refers to the present numerical simulation. Dashed lines indicate analytical predictions found in literature for the diffusion regime ($t < 10^3$, Eq. (4.13)), the constant flux regime ($2\times10^4 < t < 2\times10^5$, Eq. (4.17)) and the shutdown regime ($2\times10^5 < t < 3\times10^6$, Eq. (4.19)). The formulation of these theoretical predictions is explicitly given in the text (Sec. 4.3). Note that the extent of the different flow regimes is also explicitly indicated. Panels a,c) World lines of the concentration field measured along an horizontal slice (x) located close to the top wall ($z = -20$ for panel a, $z = -50$ for panel c) measured for different time windows during the transient evolution (panel a refers to $2\times10^2 \leq t \leq 4\times10^4$, whereas panel c refers to $4\times10^5 \leq t \leq 15\times10^5$).

encountered: *flux growth (iii), merging (iv)* and *constant flux regimes (v)*. Finally, megaplumes reach the bottom boundary (which is impermeable for both fluid and solute) and the reservoir starts filling up with dense solute: the flow enters the so called *shutdown regime (vi)*.

A comprehensive picture of the entire time-dependent flow dynamics just drafted above is shown in Fig. 4.2. The central panel of this figure (Fig. 4.2b) presents the behaviour of the solute flux $F(t)$ as a function of time. The dashed lines represent analytical prediction of $F(t)$ found in literature for the different flow regimes, the extensions of which are explicitly indicated as well (further details on the different scalings and analytical expressions will be explicitly given in the following sections). Associated to the changes of F(t) in time, we expect a modification of the flow structure. This is clearly shown in Fig. 4.2a and Fig. 4.2c, where the time evolution of the concentration C measured along an horizontal slice located close to the top wall is plotted. This provides a good representation for the behaviour of plumes in time. In particular, we note that diffusion dominates for $t < 10^3$ (Fig. 4.2a), with plumes appearing only at the end of the linear growth regime (emergence of dark roots at $t \simeq 10^3$ in Fig. 4.2a). For $t > 10^3$ plumes start interacting (merging and constant flux regimes in Fig. 4.2a). Later, during the constant flux regime and for most of the shutdown regime, the dominating dynamics consists of small protoplumes (small ribs in Fig. 4.2c) generated at the wall and merging into larger megaplumes (long roots in Fig. 4.2c). Note that during the shutdown regime the relative strength of protoplumes and megaplumes compared to the surrounding flow decreases with time (flow homogeneization for $t > 10^5$, Fig. 4.2c). The above dynamics of solute convection in an isotropic porous medium has been widely investigated from both a numerical and an experimental point of view (Slim, 2014; Hewitt et al., 2013a; Pau et al., 2010; Neufeld et al., 2010). However, it has been only slightly characterized for a non-istotropic porous medium (Xu et al., 2006; Cheng et al., 2012; Green and Ennis-King, 2014).

In the following, we try to fill this gap, discussing the effect of γ on the solute dynamics. We will recast the entire dynamics into three main stages: a diffusion dominated stage (including diffusion and linear growth); a convective dominated stage (including flux growth, merging and constant flux); and a shutdown stage (shutdown).

4.3.1 The diffusion-dominated stage

As already discussed, upon injection from the top boundary, the solute moves downwards by diffusion. Since solute diffusion is very slow, the bottom boundary can be considered sufficiently far from the top boundary during this stage. Therefore, we can approximate the bottom boundary conditions as

$$w = 0 \quad , \quad C \approx 0 \quad \text{on} \quad z = -Ra\,. \tag{4.11}$$

Within this framework, the solution of Eq. (4.6) yields:

$$C(z,t) = 1 + \mathrm{erf}\left(\frac{z}{\sqrt{4t}}\right), \tag{4.12}$$

with the dimensionless solute flux being

$$F(t) = \frac{1}{L}\int_0^L \left.\frac{\partial C}{\partial z}\right|_{z=0} dx = \frac{1}{\sqrt{\pi t}}\ , \tag{4.13}$$

where L is dimensionless domain width. The corresponding amount of solute dissolved in time, $G(t)$, is given by the integral of the solute flux $F(t)$,

$$G(t) = \int_0^t F(\tau)d\tau = \frac{2\sqrt{t}}{\sqrt{\pi}}. \tag{4.14}$$

The profiles of $F(t)$ and $G(t)$ obtained from the present computations are shown in the two panels of Fig. 4.3 for $Ra = 2 \times 10^4$ and different values of γ (symbols in Fig. 4.3). The dashed line in Fig. 4.3 indicates the analytical prediction given by Eq. (4.13). We first consider Fig. 4.3a. For $t < 10^3$, we observe that the behaviour of $F(t)$ is independent of γ and follows nicely the theoretical predictions. Later in time, at $t = t_{on}$ (onset time of convection), convection is triggered and the profile of $F(t)$ departs from the theoretical prediction of a pure diffusive flow. In literature, there are different expressions to find the value of t_{on} as a function of γ (Green and Ennis-King, 2014), essentially because t_{on} depends on the initial conditions prescribed in the simulations. To predict the value of t_{on}, we follow the expression of Cheng et al. (2012):

$$t_{on} = 47.9\gamma^{0.79}\ . \tag{4.15}$$

In the present cases, we obtain $t_{on} = 47.9$ ($\gamma = 1$), $t_{on} = 38$ ($\gamma = 3/4$) and $t_{on} = 27$ ($\gamma = 1/2$). The departure of $F(t)$ from the purely diffusive profile for $t > t_{on}$ is barely visible at the beginning. Well beyond t_{on}, at time $t = t_d$, diffusion is balanced by convection and the dissolution flux reaches a minimum. We further remark here that there is a large difference between t_{on} and t_d (t_d is on average two orders of magnitude larger than t_{on}). The decrease of γ (i.e. the increase of the horizontal permeability) reduces the value of t_d (and also of t_{on}), indicating that convection is triggered early when $\gamma < 1$. In particular, we found $t_d \simeq 2.2 \times 10^3$ ($\gamma = 1$), $t_d \simeq 1.6 \times 10^3$ ($\gamma = 3/4$) and $t_d \simeq 1.1 \times 10^3$ ($\gamma = 1/2$). Just after t_d, the dissolution flux increases sharply. For this reason t_d is sometimes taken as a practical measure of the onset time of convection. From a phenomenological point of view, after t_d viscous fingers become visible and start transporting efficiently dense solute away from the boundary, so to increase the dissolution flux. Fingers are at first characterized by negligible lateral movements (see also the regular and parallel footprint of fingers during the flux growth regime in Fig. 4.2). Later, fingers increase their length and strength and start

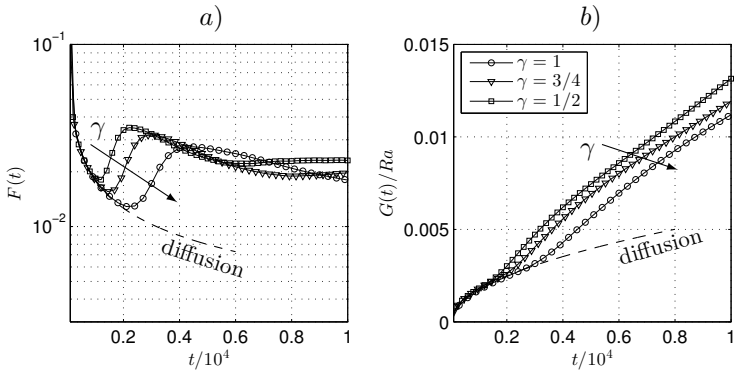

FIGURE 4.3 – Panel a) Solute dissolution flux $F(t)$ vs time t in the early stages of the simulations, plotted for $Ra = 2 \times 10^4$ and $\gamma = 1/2,\ 3/4$ and 1. The dashed line represents the dissolution flux computed as in Eq. (4.13). Panel b) Total solute dissolved from $t = 0$ for the different permeability ratios considered (solid lines) and from the theory (Eq. (4.14)). We report the same simulations presented in a), and the lower the permeability ratio, the sooner the flux deviates from diffusion.

modifying the entire velocity field. This cause fingers to come closer and eventually merge with the neighbours (as also shown by the evolution of the finger roots during the merging regime in Fig. 4.2a to create larger plumes. The merging process decreases the number of plumes and increases the boundary layer thickness, hence reducing the dissolution flux (decrease of $F(t)$ for $t > 0.2 \times 10^4$ in Fig. 4.3). By looking at the behaviour of $G(t)$ in Fig. 4.3b, one important observation can be made. After the initial transient where $G(t)$ follows the pure diffusional profile (regardless of the value of γ), we note that solute dissolution appears more efficient for decreasing γ. At $t = 10^4$, the amount of solute dissolved for $\gamma = 1/2$ can be up to 20% larger compared to $\gamma = 1$.

4.3.2 The convection-dominated stage

After the initial diffusive dynamics, the flow enters a convection dominated stage called constant flux regime (Slim and Ramakrishnan, 2010; Slim et al., 2013; Slim, 2014). During this regime, primary plumes already generated in the previous stages of the flow rapidly grow. At the same time, the diffusive boundary layer between adjacent plumes becomes unstable and continuously produces new protoplumes. The newly formed protoplumes are driven laterally by the background flow and coalesce with primary plumes. During this stage, the average flux of solute fluctuates around a mean constant value (Fig. 4.4). For isotropic conditions ($\gamma = 1$), we recover the value $F(t) = 1.7 \times 10^{-2}$ proposed by Pau et al. (2010), Slim (2014) and Hesse (2008), among the others. The dimensional solute flux can be expressed

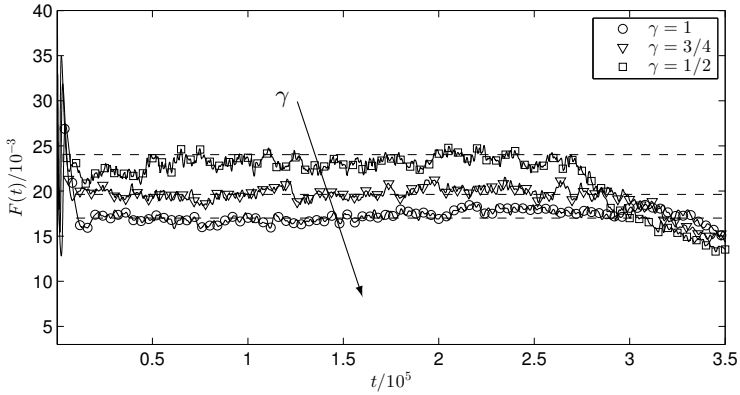

FIGURE 4.4 – Constant flux regime. Dimensionless solute flux $F(t)$ for three different permeability ratios (1/2, 3/4 and 1) at fixed Rayleigh number ($Ra = 2 \times 10^4$). In the constant flux regime, the simulations (solid lines) are in good agreement with the predictions of Green and Ennis-King (2014) (dashed lines).

(Neufeld et al., 2010; Green and Ennis-King, 2014) as

$$F^*(t^*) = 0.017\sqrt{k_h k_v}\frac{C_s^* \Delta\rho^* g}{\mu} \tag{4.16}$$

or, in dimensionless form,

$$F(t) = 0.017\gamma^{-1/2} \ . \tag{4.17}$$

The theoretical predictions given by Eq. (4.17) are shown by the dashed lines (−−) in Fig. 4.4. We note a fair agreement between numerical results (symbols) and theoretical predictions (dashed lines), which demonstrates that the scaling law proposed in literature for lower values of Ra ($10^3 \leq Ra \leq 9 \times 10^3$, where the minimum and maximum extrema correspond to $\gamma = 1/20$ and $\gamma = 1$ respectively) can be extended to larger values of Ra. Note that, although the time at which the constant flux regime starts does depend on the initial conditions of the flow, the average value of the dissolution rate $F(t)$ in the constant flux regime does not (Slim, 2014). This indicates also that the constant flux regime (and the final shutdown regime) are universal stages in which the effects of different initial conditions are only chaotic fluctuations around the average behaviour. Therefore, the corresponding parametrization (presented in this section and in the following ones) is universal and does not depend on the specific initial conditions. We wish to remark here that this dynamics does not change substantially in 3D domains. The main difference between 2D and 3D results is that time fluctuation of $F(t)$ around its average value are large for 2D rather than for 3D cases (Pau et al., 2010). This was also observed by Hewitt et al. (2014), using different boundary conditions (i.e. Dirichlet type boundary conditions at both top and bottom boundaries).

4.3.3 The shutdown stage

Once the plumes reach the bottom boundary, the domain starts filling up with dense solute and the flow enters the last stage of its dynamics, usually called the shutdown stage. Despite its practical importance, the shutdonw stage in anisotropic porous media has never been explicitly computed, with the only available predictions (De Paoli et al., 2016) being based on extrapolations from different flow configurations (different boundary conditions at the bottom wall). In the present chapter, we explicitly compute the solute dynamics in the shutdown regime for $\gamma < 1$. Results are shown in Fig. 4.5. Symbols in Fig. 4.5a refer to the behaviour of $F(t)$ for $\gamma = 1$. These results are obtained running four different simulations with different initial random perturbations, and averaging the corresponding results to observe a smoother profile. The dashed line represents the theoretical prediction of $F(t)$ based on numerical results for the two-sided configuration (De Paoli et al., 2016). We briefly recall here that these theoretical predictions prescribe that $F(t)$ depends on the permeability ratio γ and on the convective time scale $\hat{t} = \Phi H^*/W^*$ as:

$$F^*(t^*) = \frac{4\alpha\gamma^n \hat{t}}{\left(\hat{t} + 4\alpha\gamma^n t^*\right)^2} H^* \Phi C_s^*, \tag{4.18}$$

with $\alpha = 0.00688$ and $n = -0.25$. Upon rescaling this expression with the present length and time scales, we obtain the following behaviour for the dimensionless dissolution flux $F(t)$:

$$F(t) = \frac{4\alpha\gamma^n}{\left(1 + 4\alpha\gamma^n t/\, Ra\right)^2} \ . \tag{4.19}$$

For $\gamma \to 1$, Eq. (4.19) tends to the expression given by Hewitt et al. (2013a). First note that the temporal extension of the shutdown stage ($O(10^6)$) is at least an order of magnitude larger than that of the previous stages ($O(10^5)$). We clearly observe that the prediction obtained using the theoretical model follows nicely the numerical simulations, but during the transition of the flow from the constant flux to the shutdown regime, up to $t \simeq 4\times10^5$. The source of this discrepancy lies on the model hypothesis of having a well mixed $C(t)$ profile, which is not fulfilled during this transition. The corresponding behaviour of the solute dissolved in time during the shutdown stage, $G(t)$, is shown in the inset of Fig. 4.5a for $\gamma = 1$. As expected, G(t) increases sharply at the beginning and levels for larger times, due to the ongoing weakening of convection. To highlight the role of γ on the dynamics of the shutdown regime, in Fig. 4.5b we show the behaviour of the normalized difference $G(\gamma)/G(1) - 1$ between the solute dissolved for $\gamma \neq 1$ and that dissolved for $\gamma = 1$. We clearly observe that the amount of solute dissolved for $\gamma \neq 1$ can be definitely larger (up to 25% for $\gamma = 1/2$) than that dissolved for $\gamma = 1$. Note that this difference increases for decreasing γ. As expected, in

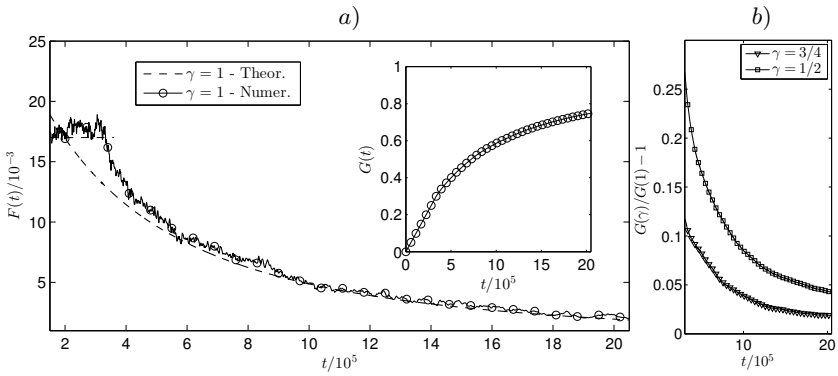

FIGURE 4.5 – Panel a) Dynamic behaviour of the solute dissolution flux F(t) for $Ra = 2 \times 10^4$ and $\gamma = 1$ ($- \circ -$) during the shutdown regime (and including also a small part of the constant flux regime, $t < 4 \times 10^5$). The theoretical prediction given by the model of De Paoli et al. (2016) is also shown (dashed line, $--$). The amount of solute dissolved in time, G(t) is shown in the inset for $\gamma = 1$. Panel b) Dynamic behaviour of the normalized amount of solute $(G(\gamma) - G(1))/G(1)$ dissolved for $\gamma = 1/2$ and $\gamma = 3/4$.

the long term limit ($t > 20 \times 10^5$) the solute dissolved depends only on the available volume but not on γ (i.e., $\lim_{t\to\infty} [G(\gamma)/G(1) - 1] = 0$).

From the discussion presented above, it is apparent that most of the solute dissolution occurs during the constant flux and the shutdown regime (they cover a large proportion of the dynamics, $t > 2\times10^4$). For this reason, deriving simple and reliable models of these two regimes based on accurate small-scale simulations is crucial for the development of numerical tools for the prediction of the solute dynamics in realistic applications (large-scale reservoirs with anisotropic permeability). This will be accomplished in the next section.

4.4 Model definition

In the previous sections we have revisited the available models found in literature (Hewitt et al., 2013a; Slim, 2014; Green and Ennis-King, 2014; De Paoli et al., 2016) to descibe the solute dissolution in geological reservoirs having anisotropic rock permeability. To summarize our previous observations,

$$F(t) = \begin{cases} 1/\sqrt{\pi t} & , \quad 0 \le t < t_1 \\ 0.017\gamma^{-1/2} & , \quad t_1 \le t < t_2 \\ 4\alpha\gamma^n / \left(1 + 4\alpha\gamma^n t/\, Ra\right)^2 & , \quad t_2 \le t < +\infty \end{cases} \tag{4.20}$$

where t_1 and t_2 represent the time at which the constant flux and the shutdown regime start, respectively. Although the expression of $F(t)$ is well

defined for the different regimes, the time instants at which the different regimes that start and finish remain still unclear. To resolve this problem, we propose the following reasoning.

At the beginning, the entire domain is fully saturated with pure brine, such that

$$C^*(x, z \neq 0, t = 0) = 0 \qquad \forall x. \tag{4.21}$$

At $t > 0$, CO_2 is injected from the top boundary and the domain starts filling up with dense solute. The maximum quantity of solute that can be dissolved is given by the available volume of the reservoir per unit depth, ΦH^*, multiplied by the concentration of the saturated upper boundary C_s^*. The amount of solute dissolved from time zero to the time t^*, $G^*(t^*)$ [kg/m^2], is

$$G^*(t^*) = \int_0^{t^*} F^*(\tau^*) d\tau^*. \tag{4.22}$$

Upon rescaling of G^* by $\Phi C_s^* H^*$, we have (De Paoli et al., 2016) $G(t \to +\infty) = Ra$. This imposes a constraint for the dimensionless flux $F(t)$, since

$$\int_0^{+\infty} F(\tau) d\tau = Ra \ . \tag{4.23}$$

Neglecting the contribution of the flux growth and merging regimes to the solute dissolution process (these two regimes are short in time, depend on the initial condition and are hard to parametrize (Slim, 2014)), and using the expression summarized in Eq. (4.20) for $F(t)$, we obtain

$$\frac{2}{\sqrt{\pi}}\sqrt{t_1} + 0.017\gamma^{-1/2}(t_2 - t_1) + \frac{Ra}{1 + 4\alpha\gamma^n t_2 / Ra} = Ra \ . \tag{4.24}$$

From both literature predictions (Slim, 2014) and present results, we have $t_1 = O(10^3)$. We can easily show that, for large Ra, the amount of solute dissolved during diffusion, $G = O(10)$, is negligible compared to the total amount of solute dissolved in the entire dissolution process, $G(\infty) = Ra = O(10^4)$. Therefore we end up with

$$\frac{t_2}{Ra} = \left(\frac{4\alpha\gamma^n}{0.017\gamma^{-1/2}} - 1 \right) \frac{1}{4\alpha\gamma^n} \approx 31\gamma^{0.68} - 8.3 \ , \tag{4.25}$$

where the approximation (numerical fit) allows to obtain a quick evaluation of the theoretical shutdown time neglecting the phenomena occurring during the transition from the constant flux to the shutdown regime. Theoretical (solid line, $-$) and approximated solution (symbols, $\circ$) are reported in Fig. 4.6. We observe an excellent fit for $\gamma > 1/20$.

According to this result, the isotropic shutdown time $t_2(\gamma = 1) = 22.6$ is approximatively 50% larger than the expected one ($15 - 16 \times Ra$, see also Hewitt et al. (2013a) and Slim (2014)). As already mentioned, this problem is due to the behaviour of the solute concentration during the transition

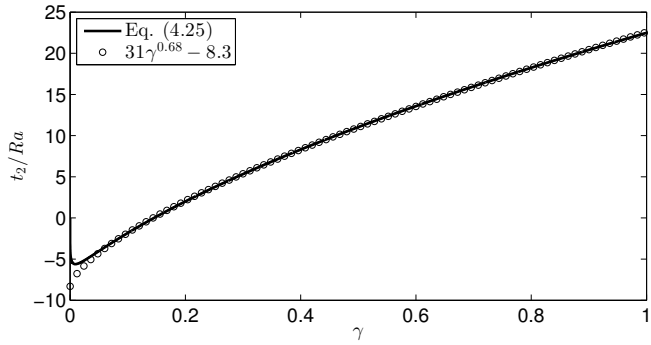

FIGURE 4.6 – Theoretical shutdown time $t_2/\,Ra$ is plotted as a function of the permeability ratio γ. Expression given by Eq. (4.25) (solid line, $-$) and approximated solution (symbols, $\circ$) are shown. The approximate solution $\left(31\gamma^{0.68} - 8.3\right)$ well fits the analytical expression for $\gamma > 1/20$.

from the constant flux regime to the shutdown regime. During this transition, the assumption of having a well-mixed concentration profile used to derive the model (De Paoli et al., 2016) is not fulfilled. This is apparent in Fig. 4.7, where the solute concentration in the domain is explicitly shown at different times (from P1 to P4). The distribution of C is definitely not uniform for P1, P2 and P3 (hence the concentration profile is not uniform, i.e. solute is not well-mixed), whereas it becomes more homogeneous for P4 (solute is well-mixed). In an effort of obtaining a more precise estimate of the time at which the shutdown regime starts (t_2), we should model the time evolution of the concentration profile during the transition between the constant flux regime and the shutdown regime. From the results of our numerical simulations (Fig. 4.8a), we observe that the horizontally-averaged concentration profile at a certain time instant t during the constant flux regime, $\overline{C}(z,t) = 1/L \int_L C(x,z,t)dx$, exhibits an almost linear variation along the vertical coordinate z (see the solid line in Fig. 4.8a). Therefore, $\overline{C}(z,t)$ can be expressed as

$$\overline{C}(z,t) = -\frac{C_1(t)}{z_1(t)}[z - z_1(t)], \tag{4.26}$$

with, $z_1 \leq z \leq 0$ for any t. The linear prediction of $\overline{C}(z,t)$ given by Eq. (4.26) is also shown in Fig. 4.8a (dashed line, $--$) together with the numerical results. To determine the value of the two constants of the model (C_1 and z_1, which in general do depend on time), we use the following constraints. At the beginning ($t = 0$) the domain is solute-free (fully-saturated with pure brine). At $t > 0$, CO_2 is injected from the top boundary. Therefore, the amount of solute dissolved from time $t > 0$ up to time t is equal

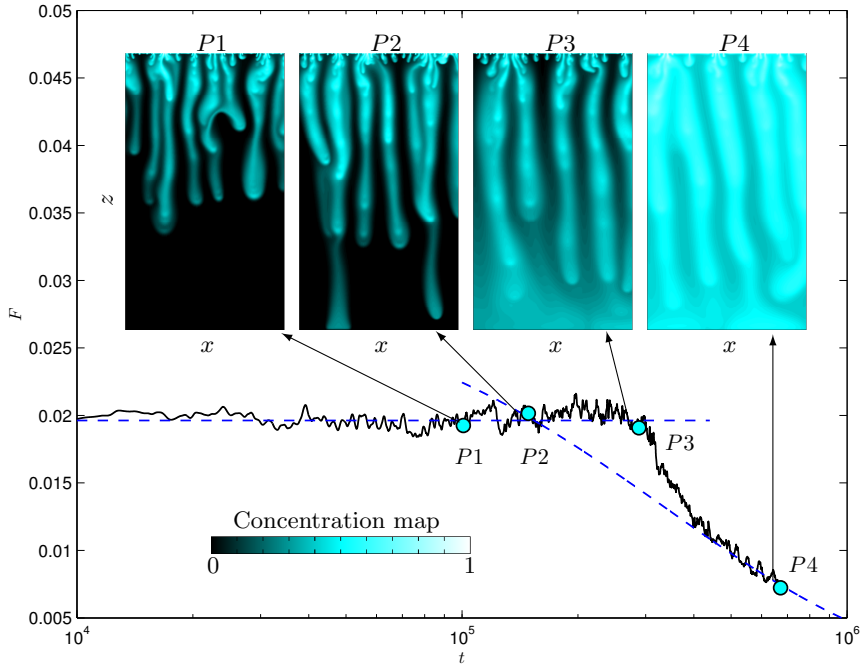

FIGURE 4.7 – Transition phase between the constant flux and the shutdown regime. Solid line (−) indicates the time evolution of the dissolution flux $F(t)$, whereas the dashed lines (−−) correspond to the theoretical predictions given by the models (see Eqs. (4.17), (4.19)). Four different snapshots of the solute concentration fields are also shown. In P1, plumes are far from the bottom boundary (constant flux); plumes reach the bottom boundary in P2; later, the domain starts filling up with dense solute (P3) until convection shutdown (P4).

to the amount of solute contained in the volume V at time t:

$$\int_0^t \left(\int_L \left. \frac{\partial C(x,z,\tau)}{\partial z} \right|_{z=0} dx \right) d\tau = \int_V C(x,z,t) dV \ . \tag{4.27}$$

The same result is achievable through the integration of Eq. (4.6) and accounting for the boundary conditions Eq. (4.7)-(4.8), as in Sec. 3.5.

Equation (4.27) can be integrated using Eq. (4.26) (to express $C(x,z,t)$) and Eq. (4.17) (to express $\partial C(x,z,\tau)/\partial z$) to give:

$$C_1(t) z_1(t) = -0.034 \gamma^{-1/2} t \ . \tag{4.28}$$

From our numerical simulations, we observe that $C_1(t)$ (that is the position at which the concentration starts showing a linear dependence on z, see Fig. 4.8a) is almost constant with time, regardless of the value of γ. In particular, we found $0.21 < C_1 < 0.26$ for $1/2 \leq \gamma \leq 1$. This information on C_1 can be used, together with Eq. (4.28) to obtain the value of z_1, which

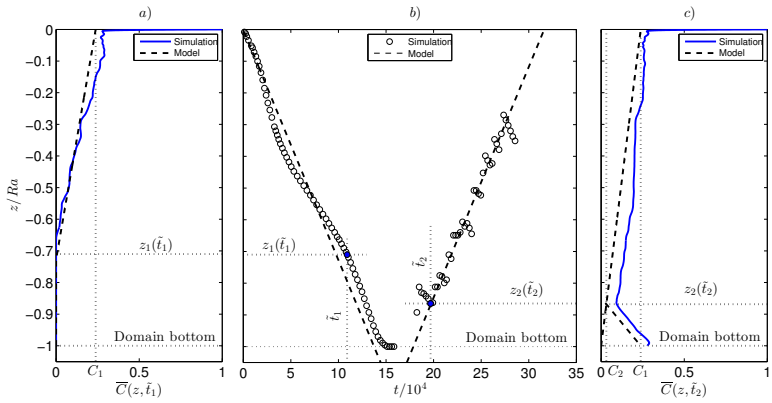

FIGURE 4.8 – Panels a) and c) Horizontally-averaged concentration profile $\overline{C}$ computed at $\tilde{t}_1 \approx 11\times10^4$ and $\tilde{t}_2 \approx 19\times10^4$. The profiles obtained from the simulation ($\gamma = 3/4$, solid lines) are plotted against the model (dashed lines). Panel b) the "averaged plume tip" $z_1(t)$ (left side) and the local concentration minimum $z_2(t)$ (right side) are plotted. The values obtained from the simulations (circles) are well approximated from the model (dashed line). The filled circles represent the instants related to the left and right panel profiles.

can be seen as the position of the wavefront of a falling solutal wave (or as the averaged tip position of falling plumes). Therefore the wavefront moves downward at a constant speed $\partial z_1/\partial t = w = -0.034\gamma^{-1/2}/C_1$. For $\gamma = 1$, $C_1 = 0.21$ and the $w = -0.16$, in fair agreement with the results obtained by Slim (2014) ($C_1 = 0.27$ and $w = -0.13$). Note that the constant speed of the solutal wavefront, which is a consequence of the linear behaviour adopted in the model, is also supported by the present numerical results. To demonstrate this, in Fig. 4.8b, we plot the dynamic behaviour of z_1 obtained from simulations (symbols, $-\circ-$), together with the theoretical behaviour (dashed line, $--$) obtained for a constant velocity profile (i.e. a linear variation of z_1 with t) is also shown for comparison. Although some discrepancies between numerical and analytical results are present, the agreement is satisfactory and demonstrates the reliability of the model.

After the plumes reach the bottom boundary, the solute concentration C increases from the bottom to the top. During this stage, the concentration profile $C(z,t)$ has a bilinear shape (see Fig. 4.8c). When the solute wavefront reaches the bottom ($t = t_b$), we have

$$\overline{C}(z,t_b) = \frac{z + Ra}{Ra} C_1 \ . \tag{4.29}$$

For $t > t_b$, after an initial redistribution phase during which C fluctuates at the bottom boundary, we can assume that the solute wavefront bounces back and moves upwards with the same average velocity of the falling phase,

w, but opposite sign. We also assume that the concentration at the bottom boundary is fixed and equal to C_1 (this is in fair agreement with the results of the simulations, see the solid line in Fig. 4.8c). From this assumptions, we find that the position of the kink of the concentration profile ($z_2(t)$ in Fig. 4.8c) moves upward from $z_2 = -Ra$ until $z_2 = 0$ as

$$z_2(t) = -Ra - w[t - (1+\eta)t_b]. \tag{4.30}$$

Note that η is a parameter accounting for the redistribution phase of solute after the first impact of the wavefront on the bottom boundary. For $\gamma = 1$, $3/4$, and $1/2$, the parameter η results to be 0.4, 0.3 and 0.2 respectively. This reflects the physical intuition that the smaller is γ (larger k_h, i.e. smaller horizontal resistance to the flow) the shorter the redistribution phase. Using the bilinear model, we are able to predict the shutdown time t_2 (i.e. the time the solute wavefront takes to reach the bottom boundary and back to the top one):

$$t_2 = \frac{(2+\eta)\,Ra}{|w|} = \frac{(2+\eta)C_1}{0.017\gamma^{-1/2}}\,Ra \quad . \tag{4.31}$$

For the isotropic case ($\gamma = 1$), we have $t_2 \simeq 14.5\,Ra$, in fair agreement with literature results (Hewitt et al., 2013a; Slim, 2014) ($15 - 16 \times Ra$).

We finally note that the shutdown time predicted by Eq. (4.31) reduces for reducing γ. This is also supported by the present numerical results (see the different times at which the profile start decreasing in Fig. 4.4).

4.5 Application to large-scale dynamics

The ability to understand the time dynamics of convective mixing over realistic spatial scales in complex geophysical flow is fundamental for proper sequestration sites selection (Gasda et al., 2011). As discussed in Sec. 4.1 and in Chap. 1, several trapping mechanisms, acting on different space and time scales, are involved in the CO_2 storage process. MacMinn et al. (2012) investigated the effect of convective dissolution on the spreading of buoyant CO_2 in homogeneous and isotropic porous media. In particular, with the aid of experiments and numerical simulations, they investigated the dynamics of buoyant CO_2 in groundwater aquifers, in order to predict the lifetime of such a current. In this section, we will draw some possible scenarios of CO_2 spreading in anisotropic porous media, using the model presented from MacMinn et al. (2012). We make a comparison between the evolution of buoyant currents in isotropic and anisotropic porous media. The results obtained from our numerical simulations and presented in previous sections of this chapter are employed, in order to quantify the lifetime of CO_2 buoyant currents in different porous formations.

4.5.1 Model description

The model presented from MacMinn et al. (2012) derives from a more fundamental model discussed in Bear (2013). The aim of the original model, which we briefly recall in this section, was to predict the behaviour of a buoyant fluid immersed in a porous medium fully satured with an heavier fluid.

Consider an isotropic, two-dimensional and homogeneous porous layer characterized by height H^*, vertical permeability k_v and porosity Φ. Suppose the porous layer is satured with a fluid (brine) with density ρ_w^* and viscosity μ_w. A lighter fluid (CO_2) with density ρ_c^* and viscosity μ_c, is injected, and it occupies a portion $2L^*$ of the domain in horizontal direction. However, due to symmetry we can consider just the right half of the domain. A sketch of the initial configuration is provided in Fig. 4.9a. Assuming impermeable horizontal walls, i.e. the geological formation is delimited by two horizontal low-permeability layers, and using the Dupuit approximation ($w^* \ll u^*$), Bear (2013) shows that the thickness of the buoyant fluid $h^*(x^*, t^*)$ evolves according to the equation:

$$\frac{\partial h^*}{\partial t^*} - W^* \frac{\partial}{\partial x^*}\left[(1-f)h^* \frac{\partial h^*}{\partial x^*}\right] = 0 \tag{4.32}$$

where

$$W^* = \frac{(\rho_w^* - \rho_c^*)\, g k_v}{\Phi \mu_c} \tag{4.33}$$

is the CO_2 buoyancy velocity and $f = Mh/[(M-1)h+1]$ is a function of the mobility ratio $M = \mu_w/\mu_c$. In this model there is no dissolution effect (r.h.s. of Eq. (4.32) is zero), and only buoyancy is considered (Fig. 4.9b). The volume of light fluid, $L^* \times H^*$, remains constant and the fluid redistributes along the upper wall.

A possible extension of this model consists into take into account the dissolution of CO_2 in brine. In this way, the evolution of the buoyant current is controlled by the dissolution rate of CO_2 in brine (q_m^*), which limits the current spreading process. Several attempts to compute the dissolution rate referring also to different geological formations are available in literature (Pau et al., 2010; Neufeld et al., 2010), and all these estimates have the same order of magnitude.

In the frame of an anisotropic porous medium, due to the approximations adopted, no difference arises in the derivation of the equations, i.e. the horizontal properties of the flow do not influence the evolution of the current thickness h^*. On the other hand, the results obtained in this chapter confirm that the solute dynamics is strongly influenced by the permeability ratio γ. Thus, according to the Eq. (4.17), we end up with $q_m^* \sim \gamma^{-1/2}$, and the porous medium anisotropy has a positive effect because the dissolution rate increases (indeed $0 < \gamma \leq 1$). The governing equation for the one-current

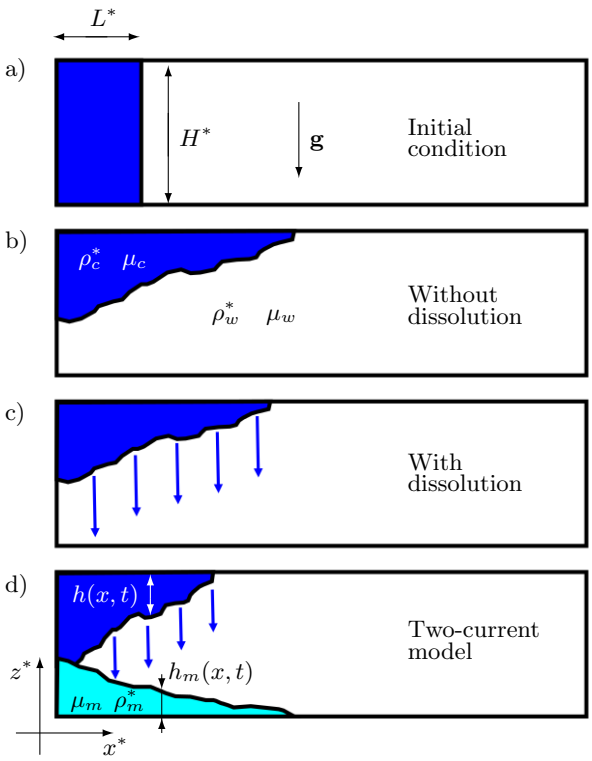

FIGURE 4.9 – Modelling of buoyant current with convective dissolution. Panel a) The system is initialized with buoyant fluid (ρ_c^*, μ_c) and ambient fluid (ρ_w^*, μ_w). Panel b) System without dissolution (pure buoyancy). Panel c) The effect of the dissolution is included. Panel d) The dense fluid current (ρ_m^*, μ_m) interacts with the buoyant one and modifies the evolution of the system (i.e. modifies the lifetime of the buoyant current).

model with dissolution in anisotropic porous medium becomes:

$$\frac{\partial h^*}{\partial t^*} - W^* \frac{\partial}{\partial x^*}\left[(1-f)h^* \frac{\partial h^*}{\partial x^*}\right] = -\frac{q_m^*}{\Phi} \ , \tag{4.34}$$

and a schematic representation in provided in Fig. 4.9c.

Finally, a further extension consists into account for the influence of the satured fluid (CO_2+brine mixture), with properties ρ_m^* and μ_m, on the dissolution process of the buoyant fluid (Fig. 4.9d). In this case, we consider two currents, and we indicate the height of the second current with h_m^*. We introduce the volume fraction of the buoyant fluid dissolved in the dense fluid $X_v = \rho_m^* X_m / \rho_c^*$, being X_m the mass fraction. Furthermore, we define the mobility ratio for the dense fluid $M_m = \mu_w/\mu_m$ and the buoyancy velocity ratio δ

$$\delta = \frac{W_m^*}{W^*} = \frac{(\rho_m^* - \rho_w^*) g k_v / \Phi \mu_m}{(\rho_w^* - \rho_c^*) g k_v / \Phi \mu_c} \ . \tag{4.35}$$

Using as dimensionless variables

$$x = \frac{x^*}{L^*} \quad , \quad h = \frac{h^*}{H^*} \quad , \quad h_m = \frac{h_m^*}{H^*} \tag{4.36}$$

$$t = \frac{t^*}{\left(L^*\right)^2 / (W^* H^*)} \quad , \quad \varepsilon_0 = \frac{q_m^*}{\Phi W^*} \left(\frac{L^*}{H^*}\right)^2 \tag{4.37}$$

the equations of the model become[1] finally:

$$\frac{\partial h}{\partial t} - \frac{\partial}{\partial x}\left[(1-f)h\frac{\partial h}{\partial x} - \delta f h_m \frac{\partial h_m}{\partial x}\right] = -\varepsilon \tag{4.38}$$

$$\frac{\partial h_m}{\partial t} - \frac{\partial}{\partial x}\left[\delta(1-f_m)h_m\frac{\partial h_m}{\partial x} - f_m h\frac{\partial h}{\partial x}\right] = \frac{\varepsilon}{X_v} \tag{4.39}$$

$$f = \frac{Mh}{(M-1)h + (M_m - 1)h_m + 1} \tag{4.40}$$

$$f_m = \frac{M_m h_m}{(M-1)h + (M_m - 1)h_m + 1} \tag{4.41}$$

where the dissolution rate ε is defined as follows:

$$\varepsilon(x) = \begin{cases} 0 & , \quad \text{if } h(x) = 0 \text{ or } (h + h_m)(x) = 1 \\ \varepsilon_0 & , \quad \text{else} \end{cases} . \tag{4.42}$$

The adoption of such a conditional definition, allows us to neglect dissolution where the currents are in touch ($h(x)+h_m(x) = 1$) and where the light fluid is absent (i.e. $h(x) = 0$).

4.5.2 Implications for geological CO2 sequestration

The two-current model described by Eqs. (4.38)-(4.41) is sensitive to the domain properties and to the fluids properties. In this section, we study two different injection scenarios characterized by different volumes of CO_2 injected, but keeping constant all the other properties, except for the permeability ration γ. We consider four scenarios and we analyse possible implications for long terms storage arising from anisotropy in the permeability field.

Domain properties We consider an aquifer in the Sleipner formation (North Sea), whose parameters are available in literature. For instance, Bickle et al. (2007) suggest that the "Layer 8" in the Sleipner site is characterized by $H^* = 20$ m, $\Phi = 0.300$ and $k_v = 4 \times 10^{-12}$ m^2. Moreover, we consider two different values for the permeability ratio: $\gamma_1 = 1$ and $\gamma_2 = 1/4$.

[1] For a detailed derivation of the equations, see MacMinn et al. (2011).

Fluids properties CO_2 density and viscosity are $\rho_c^* = 490$ kg/m^3 and $\mu_c = 3.52\times10^{-5}$ Pa s respectively (Bickle et al., 2007), whereas brine density and viscosity are $\rho_w^* = 1020$ kg/m^3 (Bickle et al., 2007) and $\mu_c = 5.95\times10^{-4}$ Pa s (Pau et al., 2010). We assume (MacMinn et al., 2012) that the viscosity mixture does not change significantly with respect to the pure brine viscosity ($\mu_m = \mu_w$) and the density difference existing between pure and satured brine is $\rho_m^* - \rho_w^* = 10.45$ kg/m^3 (Pau et al., 2010). Moreover, a mass fraction of fluid mixture dissolved in brine $X_m = 0.01$ is considered (MacMinn et al., 2012), and the corresponding volume fraction is $X_v = 0.021$. According to the above mentioned properties, we obtain the viscosity ratios $M = 16.90$ and $M_m = 1$, and the velocity ratio $\delta = 0.0012$.

Dissolution parameters The dissolution rate provided by Neufeld et al. (2010) refers to an isotropic and homogeneous porous medium, and it is $q_m^* = 6.15 \times 10^{-10}$ m/s. According to MacMinn et al. (2012), we suppose to inject along a linear path whose length is $B^* = 10^4$ m. The buoyant fluid region width ($2L^*$), introduced in Sec. 4.5.1, is obtained by dividing the total mass of CO_2 injected (Q) by the quantity $\rho_c^*\Phi H^* B^*$. Finally, the dimensionless dissolution rate ε_0 can be computed from Eq. (4.36). Therefore, the only parameter dependent on the injected mass and on the permeability ratio, is the dissolution rate ε_0. We analyse the following scenarios:

S1) isotropic large sequestration project,

S2) anisotropic large sequestration project,

S3) isotropic small sequestration project and

S4) anisotropic small sequestration project,

where the definitions "large" and "small" refer to the data provided by MacMinn et al. (2012) and Bickle et al. (2007) respectively. The parameters consider for these simulation are summed up in Tab. 4.1. The numerical algorithm adopted as well as the behaviour of the model are described in Appendix 4.A.

A parameter of interest for the CO_2 sequestration projects is the maximum extension of the current (or current nose) $x_N(t)$. It indirectly represents a measurement of the amount of CO_2 dissolved (see Fig. 4.10). In order to compare different scenarios and simulations, we consider the lifetime of the current t_L, i.e. the time necessary to the light fluid (CO_2) to reach the condition $x_N(t_L) = 0$.

Results From the two-current model, we observed that the current lifetimes satisfy the relationship

$$t_L(S4) < t_L(S3) < t_L(S2) < t_L(S1) \ . \tag{4.43}$$

TABLE 4.1 – Scenarios analysed with the two-current model are summed up in this table. We consider four different configurations: isotropic (S1 and S3) and anisotropic (S2 and S4) porous media; large (S1 and S2) and small (S3 and S4) sequestration projects. The related dissolution rate ε_0, which is among the input paramters for the model, is also reported.

Name	γ	Q^* [10^9 kg]	ε_0
S1	1.00	10.00	7.532×10^{-5}
S2	0.25	10.00	1.506×10^{-4}
S3	1.00	0.178	2.378×10^{-8}
S4	0.25	0.178	4.756×10^{-8}

This trend is in agreement with the predictions, i.e. the anisotropy has a positive effect on the CO_2 dissolution. In other words, for a given amount of CO_2 injected, the higher the permeability ratio, the lower the current lifetime ($t_L(S4) < t_L(S3)$ and $t_L(S2) < t_L(S1)$). As mentioned above, the model experiences a significant sensitivity of to the geometry of the geological formation. Therefore, it is not possible to predict the reduction of the current lifetime due to anisotropy for a generic formation, unless a detailed configuration is provided. In order to obtain an indication of the current lifetimes, a possible solution consists into explore a wide range of values of ε_0. Indeed, in the present formulation ε_0 accounts also for the anisotropy effects. This analysis is left for future work.

4.6 Conclusions and future developments

In this work we focused on the transient dynamics of solute convection in a two-dimensional anisotropic porous medium. Dense solute, which was initially injected from the top boundary, was driven down by gravity and finally accumulated at the bottom impermeable boundary. With this conceptual setup, we aimed at mimicking the process of liquid CO_2 sequestration in realistic geological reservoirs.

With the aid of accurate numerical simulations, we characterized and discussed the entire solute dynamics at high Rayleigh-Darcy number ($Ra = 2\times10^4$), from the initial diffusion-dominated stage up to the final convection-dominated and shutdown stages. The role of the anisotropic flow permeability (γ) throughout the entire process was singled out. We were able to provide for the first time a unifying picture of the solute dynamics in realistic geological reservoirs. Compared to the isotropic case ($\gamma = 1$), solute convection is triggered early when $\gamma < 1$ and solute dissolution appears in turn more efficient. In particular, we observes that the finite-time amount (short-term limit) of solute dissolved and stored inside the reservoir is larger for decreasing γ (up to 25% for $\gamma = 1/2$). As expected, in the long-term limit (asymptotic behaviour), the amount of solute dissolved depends only on the available volume but not on γ.

Simplified theoretical models based on the flow phenomenology have also been developed to predict the value of the solute flux, $F(t)$, throughout the entire dissolution process. These small-scale models can be easily nested into larger scale models to obtain accurate predictions of the dissolution flux in realistic applications. An example involving two-current models has been considered, and beneficial effects induced by anisotropy have been discussed.

Further steps of this study will be the description of the solute dissolution process of a given amount of solute in a close reservoir characterized by impermeable conditions for both fluid and solute on either the top and the bottom walls. In this case, a more sophisticated approach describing the dynamics of two immiscible (or partially miscible) species could be applied (Chap. 7).

4.A Appendix

In this section, we provide some details on the numerical methodology employed to solve the model presented in Sec. 4.5. Furthermore we provide a validation of the two-current model code and a brief explanation of the role of the parameters involved.

4.A.1 Numerical details and validation

So as to obtain the evolution of $h(x,t)$, $h_m(x,t)$ and related quantities, the set of Eqs. (4.38)-(4.41) is discretized in space using a 4^{th}-order finite differences scheme and in time using a 1^{st}-order Euler explicit scheme. Furthermore, in order to neglect the influence of the right boundary, we have adopted a large domain width (up to $30 \times L$, being L the dimensionless initial CO_2 width).

The code has been validated on four different simulations, summed up in Tab. 4.2. Simulations V1 and V2 do not include the presence of the dense current. In the limit of small viscosity ratios ($M \ll 1$) and one-current, the semi-analytical solution for the evolution of the current nose $x_N(t)$ is given

TABLE 4.2 – The code has been validated on four different simulations (symbols) neglecting (V1 and V2) or including (V3 and V4) the presence of the second current.

Name	M	M_m	δ	X_v	ε_0
V1	10^{-5}	–	–	–	10^{-5}
V2	10^{-5}	–	–	–	10^{-2}
V3	10^{-5}	1.00	0.5	0.25	10^{-2}
V4	5	1.00	0.5	0.25	10^{-2}

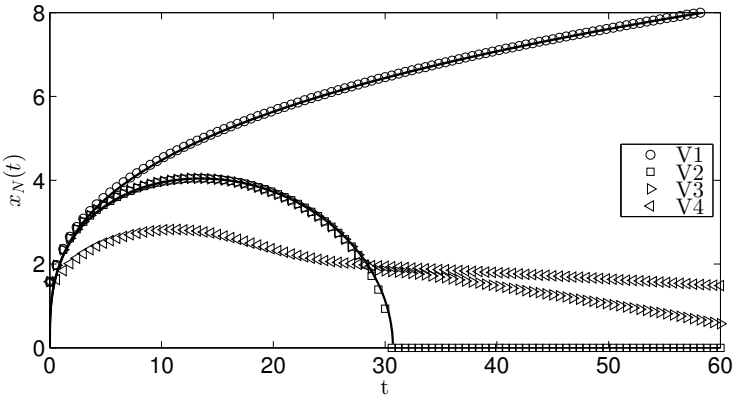

FIGURE 4.10 – Two-current model validation. The validation for the one-current model is obtained by comparing the evolution of the current nose x_N for the simulations V1 and V2, with analytical predictions of Eq. (4.44) (solid lines). Indeed, simulations V3 and V4 represent the two-current model with different values of the viscosity ratio M. The behaviour of V3 is also in agreement with the numerical solution found by MacMinn et al. (2012). All the parameters related to simulations V1-V4 are reported in Tab. 4.2.

by MacMinn et al. (2012)

$$x_N = (9t)^{1/3} \sqrt{1 - \frac{1}{18}\varepsilon_0 \, (9t)^{4/3}} \, . \tag{4.44}$$

The behaviour of x_N in time, according to Eq. (4.44) is reported in Fig. 4.10 (solid lines) for two different values of ε_0, and we observe that the numerical simulations V1 and V2 are in excellent agreement with the analytical solutions available.

4.A.2 Behaviour of two-current model

We provide here a more detailed analysis of the behaviour of the model and of its sensitivity to the governing parameters. Consider the current nose $x_N(t)$, whose evolution in time is reported in Fig. 4.10. Four approaches are represented and in each of them the comparison parameter we consider is the current lifetime t_L.

When the dissolution rate is small (simulations V1), the nose of the current evolves slowly. From Eq. (4.44), we obtain

$$t_L = \left(\frac{8}{9\varepsilon_0^3} \right)^{1/4} \tag{4.45}$$

and considering the values of ε_0 in V1 and V2 we obtain $t_{L,1} \approx 5.5 \times 10^3$ and $t_{L,2} \approx 3.1 \times 10^1$ respectively.

In V3 and V4 we take into account the effect of the second current. We observe that V3 nicely follows the theoretical behaviour, due to the small value of the mobility ratio considered ($M \ll 1$). Finally, when the mobility ratio is increased to values comparable with those typical of CO_2 aquifers (V4), the nose position early departs from the analytical profile, and t_L decreases further.

II

Rayleigh-Taylor convection

5

Introduction to Rayleigh-Taylor convection in porous media

When fluxes are exchanged between two phases, whether in terms of mass flux or not, the transfer mechanism acts through the interface. For this reason, an accurate description of the interface fulfils a key role in the modelling of dissolution phenomena. In order to include further interaction and mechanisms, the main dynamics occurring in presence of the interface should be captured first.

5.1 Diffused interface approach

An accurate physical description of the phenomena occurring along the interface, should be thermodynamically consistent. A suitable approach is represented by the phase-field model, based on the Cahn-Hilliard equation. This model governs the interaction of two immiscible fluids, or more in general of two phases, whose miscibility is allowed along the interface only, i.e. far from it the fluids are considered as pure.

When the continuous approach is applied to the description of immiscible fluid systems far from the interface region, a fictitious enlargement of the interface should be applied: real interfaces have a thickness of few molecules, namely 10^{-9} m, which require numerical resolutions that are beyond the current available limits. At that scales the continuous nature of the interface emerges (mixing layer of few molecules thickness). However, the continuum hypotheses does not apply and in those cases the applicability of this approach should be considered with attention.

In the phase-field model the state of the system is described, at any time, by a scalar order parameter ϕ, which is a function of the position vector $\mathbf{x}$. Moreover, the order parameter directly represents one of the physical properties of the fluid (i.e. molar concentration) and all the remaining properties

are in turn modelled as function of $\phi(\mathbf{x})$. According to the continuous approach, the order parameter is mathematically continuous over the entire computational domain (due to the continuous approximation of the interface) and it shows smooth variations across the interface between single fluid regions, where it assumes mostly uniform values. Coupling the continuous representation of the two fluid fields with a conservative transport equation of the order parameter, the system evolution can be resolved in time. It worth notice that the conservative nature of the model is a key point for its application to the description of immiscible fluid systems, in fact in this way the detriment of the interfacial layer is avoided and the capillary properties of the interface (i.e. surface tension) are recovered. The best-known phase-field model is represented by the Cahn-Hilliard equation, where the evolution of the order parameter is driven by the minimization of a suitable chemical potential.

Within the phase-field model theoretical framework, the capillary effects produced by the interface on the surrounding fluid are described with a force that is derived from the Korteweg stress tensor. This local force is consistent with the thermodynamic derivation of the Cahn-Hilliard equation and as a result the phase-field model gives a coherent physical description of both the interface advection and the flow field solution.

5.2 Rayleigh-Taylor configuration

A classical test case employed for buoyancy driven flows, is the well-known Rayleigh-Taylor configuration. It consists of two horizontal fluid layers, usually characterized by an initial unstable density profile. In the context of geological CO_2 sequestration, it mimics the CO_2-satured brine layer (heavy fluid) overlying a pure brine layer (light fluid). Even though this is not the most physical representation of the CO_2 dissolution process, it represents a first fundamental step, which can clarify many aspects of the dissolution dynamics involved in the solubility trapping mechanism.

5.2.1 Analogy with Hele-Shaw geometry

To perform experiments in porous media is not trivial due to their opacity. An affordable strategy consists in to adopt the Hele-Shaw cell, which is essentially composed of two plates separated by small gap, whose thickness is usually indicated with b^*. Being L^* and H^* the dimensions of the plates, within the Hele-Shaw cell, results $b^* \ll H^*, L^*$.

Consider a single phase Hele-Shaw flow. The fluid velocity field between the plates satisfies the Darcy law, provided that the permeability of the equivalent porous medium is $(b^*)^2/12$ and the porosity is unitary. The purpose of the Hele-Shaw theory is to describe depth-averaged two-dimensional porous media flows, and for single-phase configurations this

analogy is widely accepted. However, in the case of miscible fluids, concentration gradients may lead to anisotropy of the flow along the thin direction (Homsy, 1987), and the analogy with the porous medium is weaken. The analogy is even more fragile if we consider immiscible fluids. In a real porous medium, the fluids propagate through the pores of a solid matrix, and the effects of forces connected to the propagation of menisci cannot be accounted in a Hele-Shaw flow. However, Saffman and Taylor (1958) showed that for incompressible and immiscible fluids, the Hele-Shaw geometry is still governed by the Darcy law. As a consequence, it provides a good analogy with flows in porous media.

Therefore, we assume that the Hele-Shaw cell fully describes the behaviour of miscible and immiscible fluids in a two-dimensional, homogeneous and isotropic porous layer.

5.3 Outline of Part II

With respect to the mutual miscibility, fluids can be treated as miscible or immiscible. The first case is analysed with the classical advection-diffusion equation adopted in Part I. This analysis represents an excellent link between the well-known Rayleigh-Bénard configuration, studied in this thesis with particular attention to the anisotropic properties of the porous medium, and phase-field model. From this point of view, the Rayleigh-Bénard and the Rayleigh-Taylor systems share many features, which are investigated in detail above all focusing on the evolution of the structures and on the flow properties. In spite of these similarities, the Rayleigh-Taylor configuration is always unstable, whereas in the corresponding Rayleigh-Bénard system convection arises only if the governing parameter exceeds a characteristic critical value. Moreover, the system characterized by immiscible fluids exhibits a peculiar behaviour, indeed the surface tension acts stabilizing the interface. The governing parameter that accounts for this effect is the Bond number, which represents the ratio of buoyancy forces with respect to those obtained from Korteweg stresses (i.e. surface tension).

With the aid of direct numerical simulations, we will investigate the evolution of a Rayleigh-Taylor convection in two separate configurations: miscible (Chap. 6) and immiscible (Chap. 7) fluids. Results will be compared in terms of dimensional quantities (mixing length). Through the pseudo-spectral algorithm adopted (Fourier-Chebyshev discretization) we are able to analyse in detail the dynamics in presence of boundaries, result not achievable with the periodic-periodic approach commonly adopted (Fourier-Fourier). To the best of our knowledge, this is the first work where phase-field models in porous media are solved with pseudo-spectral methods.

6

Rayleigh-Taylor convection: miscible fluids

6.1 Introduction

Natural convection of miscible fluids is a fascinating phenomenon characterized by mixing. If an unstable density difference exists between two horizontal layers, the system is marked out by a Rayleigh-Taylor convection. This configuration has been widely investigated in pure fluids theoretically, numerically and experimentally (Boffetta and Mazzino, 2017). Several attempts to understand the characteristic non-linear dynamics are available in literature, dating back to the work of Fermi and Von Neumann (1953), which adopted the Lagrange equations to model the interface evolution of a squared plume. This problem has recently received renovated attention in the frame of flows in porous media, due to environmental (Huppert and Neufeld, 2014; Loodts et al., 2014) and chemical (De Wit, 2001) applications it can bear.

The Rayleigh-Taylor flow shares many similarities with the Rayleigh-Bénard problem. The latter has been investigated in past in the frame of porous media, starting from the works of Horton and Rogers Jr (1945) and Lapwood (1948), which focused on the onset of convection. More recently, few studies considered the dissolution efficiency and the flow topology both in isotropic (Hewitt et al., 2012; Otero et al., 2004) and anisotropic (De Paoli et al., 2016) porous media. Despite the affinities identified between the above mentioned configurations, the Rayleigh-Taylor system presents some peculiarities. First, if the Rayleigh-Taylor configuration is characterized by a positive top-to-bottom density difference, it is always unstable. In the corresponding Rayleigh-Bénard counterpart instead, convection arises only for Rayleigh numbers greater than $4\pi^2$. Second, the Rayleigh-Bénard problem is the archetypal of an open system, which is allowed to exchange a scalar (solute or heat) flux through its horizontal boundaries.

An overview of the earlier works regarding Rayleigh-Taylor convection

in porous media flows is provided by Homsy (1987), which described in detail the general problem of viscous fingering, considering also instabilities arising from viscosity differences, fluids miscibility (Saffman and Taylor, 1958) and finger properties and dynamics (Wooding, 1969). More recently, Fernandez et al. (2002) investigated experimentally and numerically the effect of the gap on the dynamics in a Hele-Shaw geometry, and the early stages of the instability growth. In recent years, many studies focused on the development of the mixing length in radial (Chui et al., 2015) and rectangular geometries (De Wit, 2004).

All these works examined the dynamics in the early stage of the convection process, i.e. no information is available since the finger approaches the walls and the following effects on dissolution. However, an accurate comparison of these phenomena becomes fundamental in order to quantify the time necessary to achieve, for instance, a certain amount of solute dissolved, which is the typical information required in the analysis of carbon sequestration sites. Moreover, another important parameter to be considered is the elongation of the fingers, i.e. the time required to a finger to impinge on the boundaries. To the best of our knowledge, these analyses have never been performed in wall-bounded domains. In this work, we draw an asymptotic behaviour for the Rayleigh-Taylor convection in porous media flows and we investigate the effects of the boundaries on the mixing process.

The present chapter is organised as follows. In Sec. 6.2, we will describe the numerical methodology adopted. In Sec. 6.3 we will present the results for unbounded and bounded domains. Finally, in Sec. 6.4 we will summarize our results and outline possible future developments.

6.2 Methodology

Consider a two-dimensional homogeneous and isotropic porous slab characterized by uniform permeability k and porosity Φ. The domain dimensions are L^* and H^*, in horizontal (x^*) and vertical (z^*) directions respectively. The upper half of the porous layer is initially satured with an heavy fluid (CO_2+brine) whereas the lower part with a lighter one (brine). Both these fluids are assumed to be incompressible and with a constant viscosity μ.

With the heavier fluid laying on top of the lighter fluid, the flow is driven by the composition-induced density difference in vertical direction, where the acceleration due to gravity (g) acts. The fluid velocities, u^* and w^* in horizontal and vertical direction respectively, are governed by the Darcy's law (see Sec. 2.2). Moreover, due to the typical values of the parameters involved in the carbon sequestration process, the Oberbeck-Boussinesq approximation is applied (Landman and Schotting, 2007) and the fluid velocity fulfils the equations:

$$\frac{\partial u^*}{\partial x^*} + \frac{\partial w^*}{\partial z^*} = 0 \tag{6.1}$$

$$\frac{\mu}{k}u^* = -\frac{\partial p^*}{\partial x^*} \quad , \quad \frac{\mu}{k}w^* = -\frac{\partial p^*}{\partial z^*} - \rho^* g \tag{6.2}$$

being p^* and ρ^* the pressure and the local density respectively.

Neglecting the effects of dispersion, solute is redistributed by advection and diffusion. Provided that the diffusivity is D, the solute concentration (C^*) evolves in time (t^*) according to

$$\Phi\frac{\partial C^*}{\partial t^*} + u^*\frac{\partial C^*}{\partial x^*} + w^*\frac{\partial C^*}{\partial z^*} = \Phi D\left(\frac{\partial^2 C^*}{\partial x^{*2}} + \frac{\partial^2 C^*}{\partial z^{*2}}\right). \tag{6.3}$$

We consider the fluid density as the only physical property that depends on concentration through the equation of state

$$\rho^* = \rho_s^*\left[1 - \frac{\Delta\rho^*}{\rho_s^* C_s^*}\left(C_s^* - C^*\right)\right] , \tag{6.4}$$

being ρ_s^* the density of the heavy fluid and C_s^* the corresponding concentration, i.e. maximum the concentration of CO_2 into the CO_2+brine layer, and $\Delta\rho^*$ the density difference between the satured brine and the pure brine.

6.2.1 Dimensionless equations

A relevant reference velocity scale for this flow is the free-fall buoyancy velocity, which is the vertical velocity of a rising light-fluid parcel surrounded by heavy fluid, $W^* = gk\Delta\rho^*/\mu$. We adopt as length scale H^*, even though this is not the unique reference length possible. In order to compare the evolution of domains with different sizes, i.e. different H^*, it results useful to define an alternative length scale (see Chap. 4) that will be discussed in Sec. 6.3.3. Essentially, variables are made dimensionless as in Chap. 3, with the exception of the concentration

$$x = \frac{x^*}{H^*} \quad , \quad z = \frac{z^*}{H^*} \quad , \quad u = \frac{u^*}{W^*} \quad , \quad w = \frac{w^*}{W^*} \tag{6.5}$$

$$p = \frac{p^*}{\Delta\rho^* g H^*} \quad , \quad C = \frac{C^*}{C_s^*} \quad , \quad t = \frac{t^*}{\Phi H^*/W^*} \quad . \tag{6.6}$$

Note that the absence of the superscript * is used to represent dimensionless variables. According to Eq. (6.5), the physical domain width L^* becomes dimensionless as $L = L^*/H^*$ and this quantity represents the domain aspect ratio. In other words, the dimensionless extensions of the domain are $H = 1$ and L in vertical and horizontal directions respectively.

Using the above scalings, the dimensionless velocity components are described by the equations:

$$u = -\frac{\partial P}{\partial x} \quad , \quad w = -\frac{\partial P}{\partial z} - C, \tag{6.7}$$

$$\frac{\partial u}{\partial x} + \frac{\partial w}{\partial z} = 0 \ , \tag{6.8}$$

with $P = p + z(\rho_s^*/\Delta\rho^* - 1)$ the reduced pressure, whereas the concentration is governed by the following equation:

$$\frac{\partial C}{\partial t} + u\frac{\partial C}{\partial x} + w\frac{\partial C}{\partial z} = \frac{1}{Ra_0}\left(\frac{\partial^2 C}{\partial x^2} + \frac{\partial^2 C}{\partial z^2}\right), \tag{6.9}$$

where the main parameter of the simulation appears, i.e. the final (or global) Rayleigh-Darcy number, defined as

$$Ra_0 = \frac{g\Delta\rho^* k H^*}{\mu\Phi D} \ , \tag{6.10}$$

which expresses an inverse diffusivity (De Paoli et al., 2016) or a dimensionless layer thickness (De Paoli et al., 2017).

Another key parameters is the mixing length h^*. It represents the distance occurring between the rear and the tip of the fingers, the peculiar structures that dominate the convective phenomena in porous media flows. Few strategies have been adopted in literature to define this parameter, based on local properties (De Wit, 2004), i.e. threshold value, or global properties (Cabot and Cook, 2006), i.e. integral quantities. According to De Wit (2004), we choose to identify the mixing zone, whose dimensionless extension is h, as the portion of the domain where $\varepsilon < \overline{C}(z,t) < 1-\varepsilon$, with $\varepsilon = 10^{-2}$ and being $\overline{C}(z,t)$ the horizontally-averaged concentration profile, defined as:

$$\overline{C}(z,t) = \frac{1}{L}\int_0^L C(x,z,t)dx \ . \tag{6.11}$$

We wish to remark that it is useful to define an instantaneous (also called effective or current) Rayleigh-Darcy number, Ra, defined on the mixing length h^* rather than on the domain height H^*, which will be extensively discussed in Sec. 6.3.

Boundary conditions for the governing equations are as follows: top and bottom boundaries are impermeable for both fluid and solute (i.e. no-flux boundary). In dimensionless form, these boundary conditions become:

$$w = 0 \quad , \quad \frac{\partial C}{\partial z} = 0 \quad \text{on} \quad z = 0, 1 \ . \tag{6.12}$$

Periodicity is applied at the side boundaries (along x).

A sketch of the computational domain, together with a contour map of the concentration field at a given time instant $\tilde{t}$ and the indication of the boundary conditions, is shown in Fig. 6.1a. In Fig. 6.1b, the boundary conditions and the interpretation of the mixing length have been reported.

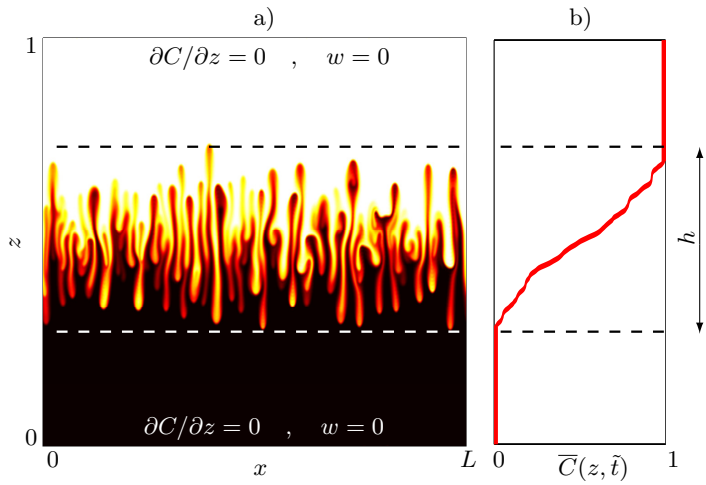

FIGURE 6.1 – Panel a) Sketch of the computational domain with explicit indication of the boundary conditions. The contour map of the solute concentration $C(x, z, t)$ at a given time instant $t = \tilde{t}$ is also shown to provide a view of the dynamics for the present configuration. Panel b) Horizontally-averaged concentration profile $\overline{C}(z, \tilde{t})$ for the same instant $\tilde{t}$ considered on panel a). The instantaneous mixing length h is represented as the extension of the tip-rear finger region (dashed lines, $--$).

6.2.2 Initial condition and code validation

Rayleigh-Taylor convection is usually initialized adopting a step-like concentration profile. According to the current configuration and dimensionless set of equations, the initial theoretical concentration field is:

$$C(x, z, t = 0) = \frac{1}{2}\left[1 + \mathrm{sgn}\left(z - \frac{1}{2}\right)\right] \quad . \tag{6.13}$$

In order to use a smoother profile to initialize the numerical simulations, we adopted a perturbed form of:

$$C_0(x, z, t = 0) = \frac{1}{2}\left[1 + \tanh\left[\beta\left(z - \frac{1}{2}\right)\right]\right] \tag{6.14}$$

being $\beta = 80$. This formulation is sufficient to mimic the step-like concentration profile described by Eq. (6.13). Several values of β have been tested, with $5 \leq \beta \leq 300$, and no significant changes in the evolution of the system appeared for $\beta \geq 80$. We decided to initialise the flow with the hyperbolic tangent rather than use the classical error function (also adopted in Chap. 4) in order to compare the results obtained in the present chapter with those obtained for immiscible fluids (Chap. 7). Indeed, in that case the concentration profile presents a stable solution defined by the function hyperbolic tangent.

The velocity field is initialized to zero everywhere and Eq. (6.9) simplifies to the form

$$\frac{\partial C}{\partial t} = \frac{1}{Ra_0}\frac{\partial^2 C}{\partial z^2} \ . \tag{6.15}$$

This partial differential equation can be solved applying boundary conditions (6.12), and the analytical solution is described by the Fourier cosine series:

$$C(z,t) = \sum_{n=0}^{\infty} A_n \cos(n\pi z)\, e^{-k(n\pi)^2 t} \ , \tag{6.16}$$

being A_n a coefficient defined as

$$A_n = \begin{cases} \int_0^1 C_0(z,t)dz & , \quad n = 0 \\ 2\int_0^1 C_0(z,t)\cos(n\pi z)\, dz & , \quad n \neq 0 \ . \end{cases} \tag{6.17}$$

Whatever the initial concentration profile C_0 is (erf, tanh, ecc.), the time-dependent profile provided by Eq. (6.16) represents an exact solution of Eq. (6.15), under the assumption of negligible convection. We used the solution of Eq. (6.16) to validate the code, and the results have been reported in Fig. 6.2a. The averaged concentration profiles obtained numerically (symbols, $\circ$) are in excellent agreement with the analytical solution (solid lines, $-$) in each of the time-steps considered.

Furthermore, in the early stage of the simulation, i.e. $h < 1$, the concentration profiles result to be self-similar if conveniently rescaled. According to Cook and Dimotakis (2001), we used the variable η, based on the mixing length h

$$\eta = \frac{1}{2}\left[1 + \frac{z - 1/2}{h/2}\right] \tag{6.18}$$

and we observed (Fig. 6.2b) that the self-similarity of the profiles is satisfied.

In this work, we investigated a wide range of Rayleigh-Darcy numbers Ra_0, from 10 to 19953, increased by a multiple factor of 10^a, where a is a constant parameter arbitrarily chosen to be 0.22. For low Rayleigh numbers, the flow is mainly controlled by diffusion. We are interested into focus on the whole dynamics involved into the dissolution process, and thus we considered for the analysis high-Ra_0 simulations (i.e. $Ra_0 > 3 \times 10^2$), which contain a rich variety of regimes.

Governing equations (6.7)-(6.9) have been solved through a pseudo-spectral Chebyshev-Tau method, which makes use of Discrete Fourier Transform (DFT) in horizontal direction, and Chebyshev polynomials in vertical direction. Further details on the numerical method can be found in Sec. 3.A and in Appendix A. The time step has been chosen to fully ensure the CFL condition. For instance, for $Ra_0 = 19953$ and $L = \pi/4$ we adopted 2048×1025 collocation points and a time step equal to $\Delta t = 5 \times 10^{-5}$.

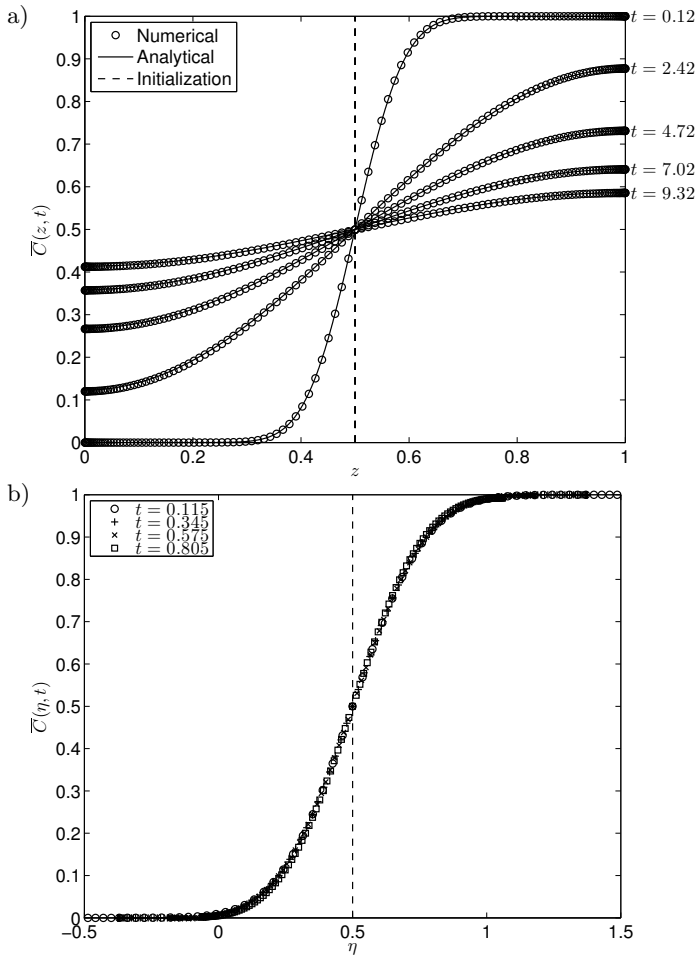

FIGURE 6.2 – Code validation. Panel a) Numerical (symbols, ∘) and analytical (Eq. (6.16), solid line, −) averaged concentration profiles for different times are reported. The initial theoretical concentration profile (dashed line, −−) is also shown. Panel b) Self-similar profiles in the early stages of the simulation with respect to the coordinate η, introduced in Eq. (6.18). All the profiles collapse on the same analytical solution. Profiles are shown for $Ra_0 = 46$.

6.3 Results

The Rayleigh number can be defined with respect to global or local properties, as discussed in Sec. 6.2.1. A convenient definition of the Rayleigh number is based on the mixing length h^*. In fact, the Rayleigh-Taylor convection can evolve independently on the walls if the fluid is initially unperturbed in the nearby of the boundaries. This is why many numerical

studies involving Rayleigh-Taylor convection are performed on periodic domains. Upon this observations, some variable can be conveniently defined in order to identify the characteristic parameters of the flow, such as the mixing Rayleigh number Ra and the Nusselt number Nu. The Rayleigh number based on the mixing length, or effective Rayleigh number, can be defined as:

$$Ra = \frac{g\Delta\rho^* k h^*}{\mu\Phi D} = Ra_0\, h \tag{6.19}$$

and due to the definition of h adopted, results $0 \leq Ra \leq Ra_0$.

The Nusselt number is commonly defined on h^*. A definition for porous media equivalent to that for pure fluids provided by Boffetta and Mazzino (2017) is the following

$$Nu = \frac{\beta\rho_s^* \langle w^* C^* \rangle h^*}{\Phi D \Delta\rho^*} \ , \tag{6.20}$$

where the angle brackets $\langle\cdot\rangle$ represent the average computed over all the domain and $\beta = \Delta\rho^*/(\rho_s^* C_s^*)$. We used this expression in order to highlight the density (i.e. concentration) difference across the layer. Considering that $\langle w^* \rangle = 0$ and using the equation of state, Eq. (6.4), the dimensionless expression for the calculation of the Nusselt number results:

$$Nu = \langle wC \rangle\, Ra \ , \tag{6.21}$$

being Ra the instantaneous Rayleigh number defined in Eq. (6.19).

In the following part of this section, we will provide a qualitative description of the evolution of the flow by considering some representative quantities that allow us to capture the main dynamics governing the system. Finally, in Secs. 6.3.2 and 6.3.3 we will describe the behaviour of the system before and after finger impingement on the walls.

In Fig. 6.3 a simulation characterized by $Ra_0 = 12023$ and $L = \pi/2$ is analysed. The concentration field is initialized as described in Sec. 6.2.2, i.e. the heavy (white) fluid layer initially stands over the light (black) fluid layer (Fig. 6.3a). This configuration is unstable and peculiar finger-like structures arise. The behaviour of the system is analysed in terms of mixing length h (Fig. 6.3b) and Nusselt number Nu (Fig. 6.3c). Moreover, an additional information on the finger position and dynamics is provided by the world lines (Figs. 6.3d-e), which represent the concentration field $C(x, z, t)$ measurements in correspondence of two cutting planes located at z_A (near-wall region) and z_B (half-channel height) reported in time along x.

Initially, the flow undergoes a slow evolution. The mixing length grows and the large number of fingers arising at half-domain decreases, due to merging. In Fig. 6.3e we observe qualitatively that for $10^{-1} \leq t \leq 10^0$ the merging process becomes more and more intensive. Afterwards, around $t \approx 2$, the light (dark) fingers impinge on the upper wall, and the near-wall region, previously unperturbed (Fig. 6.3d), is now affected by their

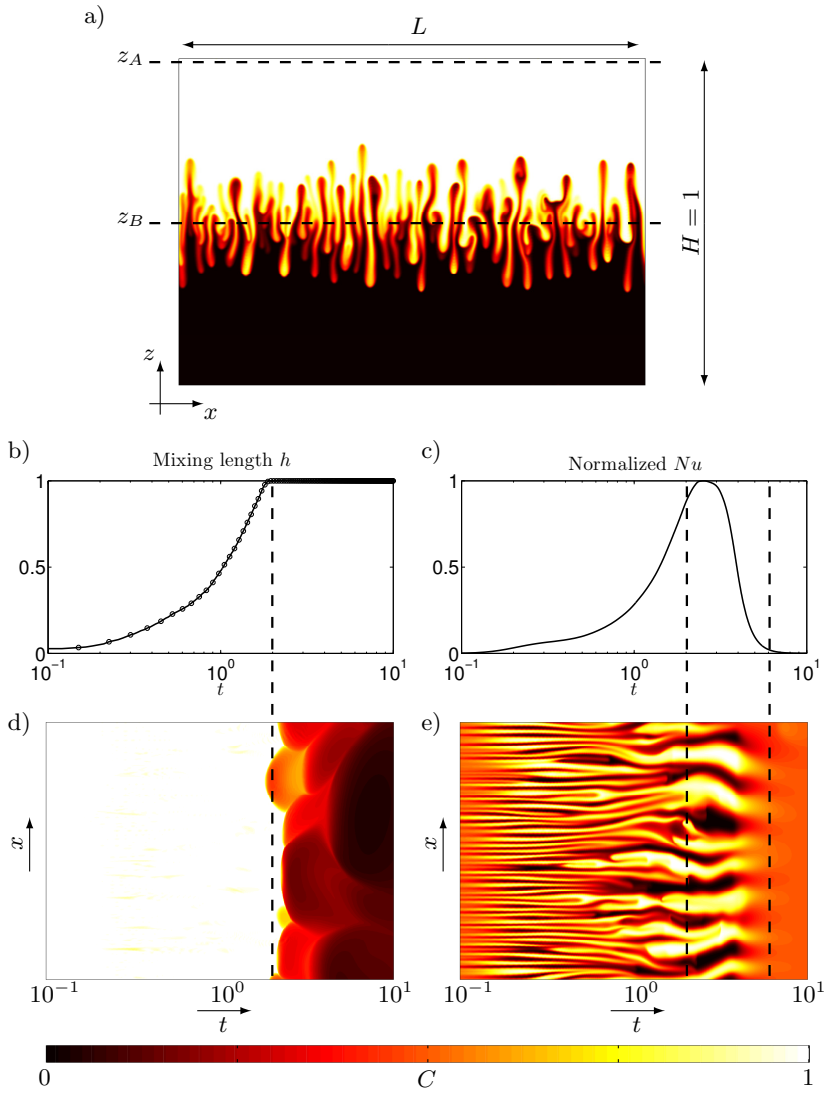

FIGURE 6.3 – Evolution of the system for $Ra_0 = 12023$. Panel a) Instantaneous concentration field. Domain dimensions are reported, as well as the position of the cutting planes z_A and z_B, 0.999 and 1/2 respectively. Panel b) Evolution of the mixing length h in time. The mixing zone grows up to the maximum space available ($h = 1$) reached at $t \approx 2$ (dashed line, $--$). Panel c) Nusselt number Nu normalized by its maximum value. The vertical dashed lines represent the impingement time of the fingers on the horizontal walls (i.e. $h = 1$, occurring at $t \approx 2$) and the time instant when Nu is sufficiently small to consider the dissolution process accomplished ($t \approx 6$) occurs. Panels d-e) World lines of the concentration field, plotted at z_A and z_B respectively. When the fingers reach the top boundary, plumes appear on the map d). When the dissolution process is completed, plumes disappear from map e).

presence. At this moment, the mixing length reaches its maximum value, i.e. $h = 1$, and the Nusselt number, almost immediately, experiences a drastic drop (Fig. 6.3c). Later, the portion of pure fluid in the inner part of the domain, still unmixed, is driven towards the walls by buoyancy and finally the mixing process shuts down ($t \approx 6$).

The steps of the mixing process described above, easy to follow at the beginning and chaotic towards the end, are recognisable also through the instantaneous horizontally-averaged concentration profiles reported in Fig. 6.4. The inner part of the domain is initially ($t < 1$) affected by finger motion, whereas a major proportion of it is unperturbed, i.e. $\overline{C}(z,t) = 0$ or $\overline{C}(z,t) = 1$ (Fig. 6.4a). Later, the mixing process becomes stronger and dominant till the finger reach the horizontal boundary, approximately at $t \approx 2$. After a chaotic transition, profiles slope finally diverts. For $t > 5$ the averaged profiles are linear and the configuration is a stably stratified (Fig. 6.4b). Hereinafter, the dissolution process will be driven by diffusion, which makes evolution considerably slower compared to the convective mixing described above. Indeed, there are just few small profile modifications from $t = 5.425$ to the last instant considered ($t \approx 11.121$).

The above mentioned dissolution process has been divided, for each high-Ra considered, in two parts: Ra-independent (or unbounded) and Ra-dependent (bounded) effects, respectively described in Sec. 6.3.2 and 6.3.3.

The numerical discretization adopted (Fourier-Chebyshev) allows a detailed investigation of the solid, horizontal boundaries effects, which are not considered with the approach commonly adopted (Fourier-Fourier) within the Rayleigh-Taylor instabilities simulations, based on periodic boundary conditions in both horizontal and vertical directions.

6.3.1 Importance of global Rayleigh number

The final Rayleigh-Darcy number, defined by Eq. (6.10), is based on the domain height H^*. Initially, all the domains are characterized by the same evolution, indeed the walls influence the dynamics only when the finger tips impact the horizontal bases. Moreover the Rayleigh-Darcy number can be interpreted as the dimensionless domain height (De Paoli et al., 2017; Slim, 2014), and in order to compare different Ra_0, i.e. domains with different sizes, we introduce a new length scale defined as the length over which advection is balanced by diffusion:

$$\mathcal{H}^* = \frac{\Phi D}{W^*} = \frac{H^*}{Ra_0} \ . \tag{6.22}$$

Rescaling by $\mathcal{H}^*$ all the quantities previously defined on the vertical domain height H^* (i.e. h, t, Nu), all the simulations can be easily compared and the influence of Ra_0 can be discussed. In order to simplify the notation, we keep the same variables introduced in Sec. 6.2.1 and we explicitly write the

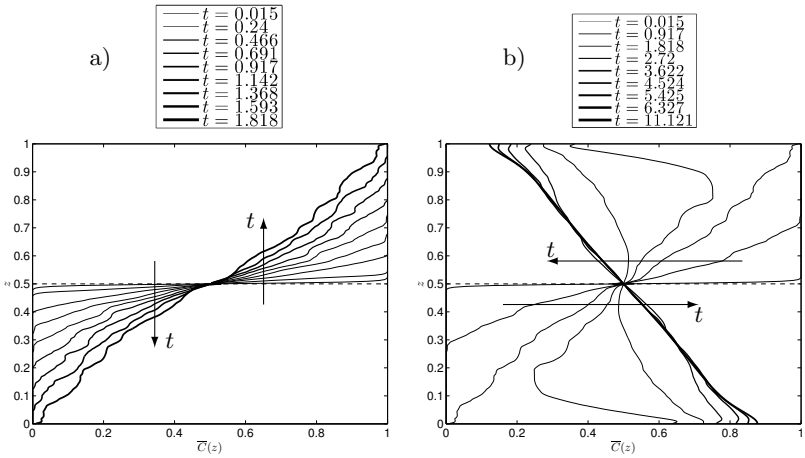

FIGURE 6.4 – Instantaneous horizontally-averaged concentration profiles $\overline{C}(z)$ at different times for $Ra_0 = 12023$ and $L = \pi/2$. Panel a) Before fingers impingements on the walls (i.e. $h < 1$). Panel b) Over the whole mixing process. The simulation and the instants considered are the same represented in Figs. 6.5 and 6.8. Profiles have been symmetrized with respect to the half channel plane. Direction of time is also reported.

relationship with Ra_0. For instance, in the case of the mixing length, we consider $h \times Ra_0$.

6.3.2 Rayleigh-independent results

A qualitative description of the flow dynamics before the finger impingement on the walls, is reported in Fig. 6.5. The flow is initially dominated by diffusion, and the theoretical solution given by Eq. (6.15) fully describes the concentration field until strength of convection is negligible, i.e. when no finger arises (Fig. 6.5a). Then, small fingers born (Fig. 6.5b) at half-channel height ($z = 1/2$). According to previous studies (Slim, 2014; De Paoli et al., 2017), we found in preliminary simulations that the dominant wavelength during the initial diffusive stage is strongly influenced by the initial perturbation (see Slim (2014) for a detailed analysis of the influence of the perturbation amplitude on such a configuration). Hereinafter, the plume number decreases due to finger merging processes (Fig. 6.5c-e). For $1 < t < 2$, the finger number remains almost constant (Fig. 6.5f-i) whereas their tip moves towards the walls, until they collide on the horizontal boundaries. A quantitative estimate of the plume number is provided with the power averaged mean wave number, which is discussed in Sec. 6.3.3.

Mixing length The flow is initially dominated by diffusion, due to the initial condition adopted for the velocity, i.e. $\mathbf{u}(t = 0) = 0$. In order to compare the simulations performed, involving different Ra_0, i.e. different space

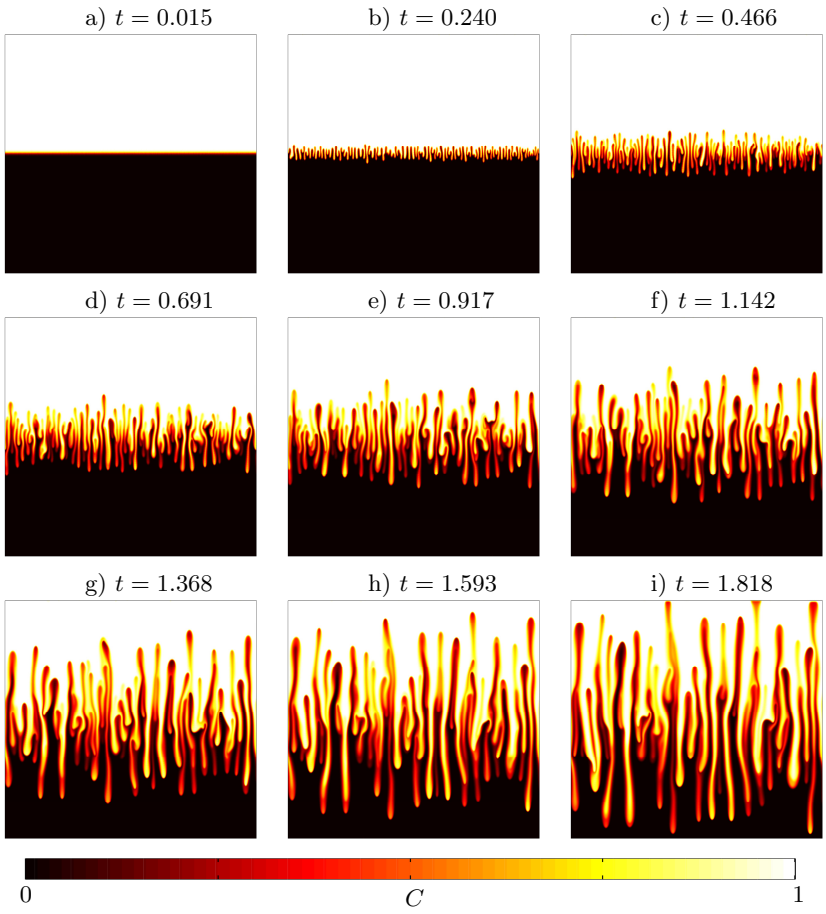

FIGURE 6.5 – Snapshots of the concentration field for $Ra_0 = 12203$ and aspect ratio $\pi/2$ before the impingement of the fingers on the walls. Instantaneous horizontally-averaged concentration profiles related to this snapshots are plotted in Fig. 6.4a.

and time scales, we rescale the time according to Eq. (6.22). The theoretical evolution of the mixing length of a domain initialized with a step-like profile, is proportional to $t^{1/2}$ that represents the initial dispersive growth. In Fig. 6.6 we report the rescaled mixing length $h \times Ra_0$, calculated for all the Rayleigh numbers considered ($347 \leq Ra_0 \leq 19953$) and several values of the aspect ratio ($\pi/4 \leq L \leq \pi/2$). For the sake of clarity, we rewrite the scaling law in terms of h rather than in terms of $h \times Ra_0$. As mentioned above, the flow is initially dominated by diffusion ($h \sim t^{1/2}\, Ra_0^{-1/2}$). Later, the mixing length grows with $h \sim t^{7/5}\, Ra_0^{2/5}$ and finally according to $t^{6/5}\, Ra_0^{1/5}$. The best fit exponents are 0.4806 ± 0.0176, 1.405 ± 0.03 and 1.206 ± 0.009, corresponding to diffusive, intermediate and final scaling re-

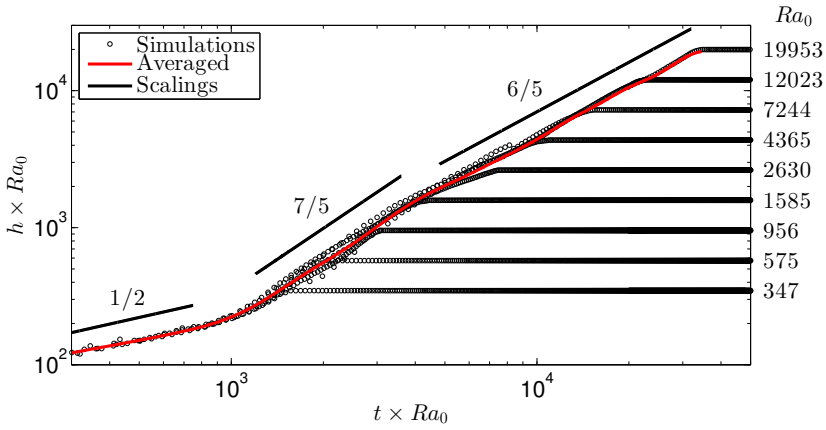

FIGURE 6.6 – Evolution in time of the mixing length h for different values of the global Rayleigh number Ra_0. All the simulations (symbols, ∘) have been performed with $L = \pi/2$ with the exception of $Ra_0 = 19953$, computed with $L = \pi/4$. The mixing length averaged over all the simulations is also reported (red, solid line) as well as the scalings (black, solid lines). The theoretical evolution $t^{1/2}$ is nicely followed by all the simulations during their initial-diffusive stage. The intermediate regime is characterized by an exponential behaviour (7/5) as well as the final regime (6/5), where the slope slightly decreases.

spectively. We observe in Fig. 6.6 that among the simulations performed, only for $Ra_0 \geq 4365$ the final scaling is sustained. Further investigations on this high-Ra_0 simulations will be presented in Sec. 6.3.3. In spite of the good agreement of the simulations during the first and the final stages, during the intermediate regime the mixing lengths slightly differ, even though the numerical fit provided by $t^{7/5}\, Ra_0^{2/5}$ is still good and recognisable. The finger number and distribution during this stage is affected by the initial perturbation. All these simulations have been performed on different grids, and in order to obtain identical curves for h, i.e. same number and position of the fingers, the same grid (or at least the same perturbation interpolated on each grid) should be adopted. This effect does not affect the initial diffusive stage (when fingers are absent) and the final stage occurring for high-Ra_0 (when the finger number is large). Further considerations on the importance of the scalings obtained above will be discussed in Sec. 6.4.1.

Nusselt number The Nusselt number, rescaled according to Eq. (6.22), is plotted in Fig. 6.7 as a function of the local Rayleigh number Ra. Simulations reported have been computed for different aspect ratios $\pi/4 \leq L \leq 2\pi$ and different Rayleigh numbers $347 \leq Ra_0 \leq 19953$, and adopting this revisited scaling all the curves match. As visible in Fig. 6.3c, after fingers impingement on the walls Nu suddenly reduces. In Fig. 6.7, we removed the diminishing part in each simulation. In other terms, each curve

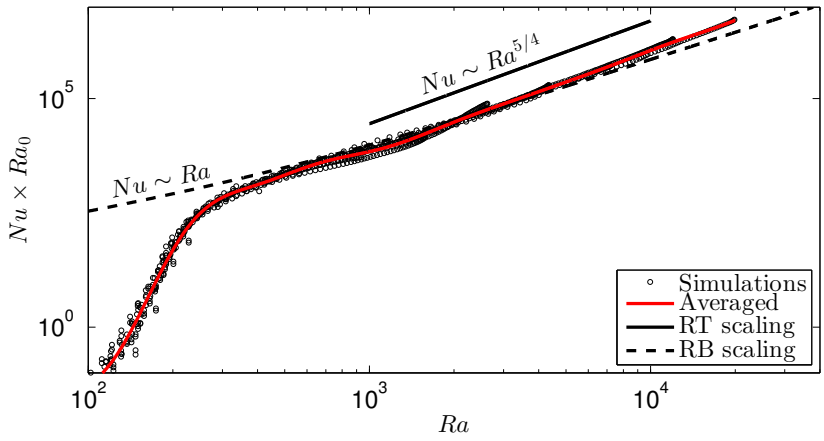

FIGURE 6.7 – The Nusselt number Nu, rescaled according to Eq. (6.22), is plotted as a function of the local Rayleigh number Ra. Simulations (symbols, ∘) have been computed for different values of the aspect ratio $\pi/4 \leq L \leq 2\pi$ and different Rayleigh numbers $347 \leq Ra_0 \leq 19953$. The rescaled Nusselt number averaged among all the simulations is also reported (red, solid line). To highlight the connection between the Rayleigh-Taylor and the Rayleigh-Bénard systems, the correlation for Nu proposed by De Paoli et al. (2016) and Hewitt et al. (2012) has also been plotted (black, dashed line). Finally, the scaling law found for the present configuration (black, solid line) is plotted.

ends when the first finger impinges on the walls (i.e. when $h \geq 1 - \varepsilon$ or $Ra \geq (1 - \varepsilon)\, Ra_0$, being $\varepsilon = 10^{-2}$ introduced in Sec. 6.2.1). The evolution can be divided in two distinct parts: the initial stage (where Nu increases rapidly, $Nu \times Ra_0 \sim Ra^{11}$) and the final stage (where Nu scales almost linearly, $Nu \times Ra_0 \sim Ra^{5/4}$). Finally, when Ra approaches Ra_0, we observe some deviations from the overall behaviour, which are due to the influence of the boundaries. During the intermediate regime, the simulations are in fair agreement even if not overlapped. We wish to remark once again that this apparently slight mismatching is due to the initial perturbation adopted.

The finger dynamics described here recalls the plume dynamics analysed during the Rayleigh-Bénard convection (De Paoli et al., 2016; Hewitt et al., 2012). If we focus on the half-channel height ($z = 1/2$), some typical fingers features can be identified. In particular, after the initial transition occurring when the fingers born, grow and merge, the number of finger remains constant and the bulk of the domain is controlled by these large structures persistent in time and space. This effect appears also in Fig. 6.3d, where for $2 < t < 6$ the flow is controlled by these megaplume-like structures.

This observations suggest that during the final stage, when the structures reflect the same behaviour experienced in the Rayleigh-Bénard configuration, the dimensionless dissolution rate Nu should also exhibit an analogue behaviour. In order to compare the results of all the simulations, we adopt

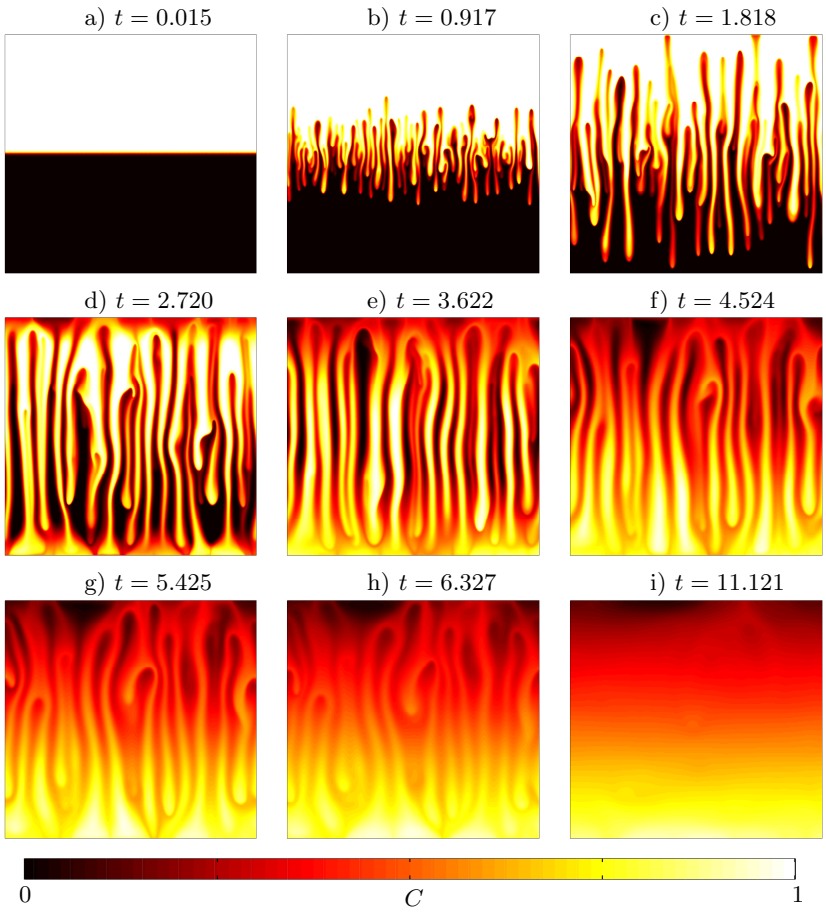

FIGURE 6.8 – Instantaneous concentration fields are reported at different instants, from the beginning (a) to the well-mixed domain (i). This fields are computed for $Ra_0 = 12203$ and aspect ratio $\pi/2$. Instantaneous horizontally-averaged concentration profiles related to these snapshots are plotted in Fig. 6.4b.

the scaling present in Eq. (6.22) and the results are shown in Fig. 6.7 (symbols, $\circ$). The scaling found in the Rayleigh-Bénard instability (Hewitt et al., 2012; De Paoli et al., 2016) is also reported (dashed line, $--$), and we observe that these two configuration are closely connected. The correlation defining this scaling is $Nu = 2.75 + 0.00688 \times Ra$ and provided that in the Rayleigh-Bénard case Ra and Ra_0 coincide.

6.3.3 Rayleigh-dependent results

As mentioned above, in this section we consider the effect of the walls on the dissolution process. To the best of our knowledge, this analysis has

never been presented, even though walls represent a remarkable effect on the flow dynamics and cannot be captured with the usual Fourier-Fourier discretization. We will first present a qualitative description of the dynamics of a confined domain, from initialization to the final stably-stratified configuration and then the effects of the walls on the dissolution process will be quantified.

In Fig. 6.8 some snapshots of the concentration field for $Ra_0 = 12203$ and $L = \pi/2$ are reported, related to several time instants. The corresponding horizontally-averaged concentration profiles are plotted in Fig. 6.4b. The flow, initially dominated by diffusion (Fig. 6.8a), is later driven by buoyancy. After the initial growth and merging regimes, presented in Sec. 6.3.2 (Fig. 6.8b-c), the first finger impinges on the horizontal boundary. Then, the core of the domain is populated by time- and space-persistent fingers (Fig. 6.8d-e). The boundaries presence information propagates across the domain and finally the bulk of the channel is influenced (Fig. 6.8f-h). The relative position of the fluids has changed, as confirmed by the averaged profiles in Fig. 6.4b for $t \geq 4.524$. The system is now dominated by diffusion and minor changes occur in the topology of the concentration field, indeed no remarkable modification in the finger position is visible (Fig. 6.8f-h). Finally, for very long times (Fig. 6.8i), the diffusion process continues and the averaged concentration profile becomes fully linear and stably stratified. Theoretically, we should obtain $\overline{C}(z, t \to \infty) = 1/2$, but due to the slowness of the diffusion process, we did not obtain it numerically by the end of the simulation.

Moreover, we are interested in to consider the efficiency of the dissolution process. We investigate the bounding effects taking into account two characteristic features: the time required to the light (heavy) fluid fingers to reach the top (bottom) boundary and the time required to the system to dissolve a considerable amount of solute (heavy fluid).

Time required to reach the boundaries: t_t The time required to the light (heavy) fluid fingers to reach the top (bottom) boundary is computed as a function of the mixing length h. In particular, it has been defined as:

$$t_t : \forall t \geq t_t \quad , \quad h(t) \geq 1 - \varepsilon \tag{6.23}$$

being ε defined in Sec. 6.2.1. Results reported in Fig. 6.9a exhibit an power scaling of t_t with Ra_0. The negative exponent of the correlation (-0.22) says that by increasing Ra_0, t_t decreases. These seemingly counter-intuitive effect could be easily explained by transporting both Ra_0 and t_t in the physical space (see Sec. 6.4.1).

Maximum dissolution time: t_m An other important parameter evaluated is the global amount of solute mixed into the domain. Due to the

solute conservation, the quantity defined by

$$\frac{1}{V}\int_V C(x,z,t)dV = \frac{1}{2} \tag{6.24}$$

is kept constant over the whole domain, being V the domain volume. The value $1/2$ is due to the initial condition adopted. We are interested into know, in time, the amount of CO_2+brine mixture (heavy fluid) dissolved in brine (light fluid). In order to evaluate it, we introduce the time-dependent dimensionless parameter D, defined as

$$D(t) = \frac{1}{V_t}\int_{V_t} C(x,z,t)dV_t \tag{6.25}$$

being V_t the upper half of the domain. Using Eq. (6.11), the dissolution parameter can be easily rewritten as

$$D(t) = \frac{1}{H/2}\int_{H/2}^{H} \overline{C}(z,t)dz \tag{6.26}$$

and due to the initial condition, is trivial to demonstrate that $D(t=0)=1$. Furthermore, for very long times, the whole domain has to reach the state of perfect mixing (i.e. $\overline{C}(z, t\to\infty) = 1/2$), when the solute contained into the heavy fluid ($C=1$) is completely dissolved into the pure fluid ($C=0$). As a consequence, $D(t\to\infty) = 1/2$. A typical behaviour for $D(t)$ is reported in Fig. 6.9. The value of $D(t)$ decreases suddenly, till reaching its minimum (lower than $1/2$), identified by the vertical dashed line ($--$), around $t \approx 20$. Then, D recovers its asymptotic value ($1/2$). In Fig. 6.9b, $D(t)$ is represented for $Ra_0 = 575$. By analysing the data obtained from the numerical simulations, we observe that the value of t_m decreases for increasing Ra_0, as well as the minimum value itself and the time required to recover the asymptotic value ($1/2$). In the range of values investigated, $t_m \sim Ra_0^{-0.27}$, i.e. t_m decreases if Ra_0 increases. We wish to remark once again that the reduction of t_m obtained by increasing the domain size, i.e. Ra_0, is only apparently counter intuitive as mentioned in the previous paragraph.

6.3.4 Regimes

In this section we provide an overview of the whole mixing/dissolution process. In particular, we quantify the finger number and we observe the finger evolution at half-channel height in order to classify the dissolution regimes.

Numerical identification of coherent structures is a recurrent problem in the investigation of buoyancy-driven flows, and many possibilities have been proposed (Ching et al., 2004; Paparella and von Hardenberg, 2012). One of the options consists in to identify a finger (or a plume) on the concentration field. In this section, we will follow the approach presented in Sec. 3.3.1

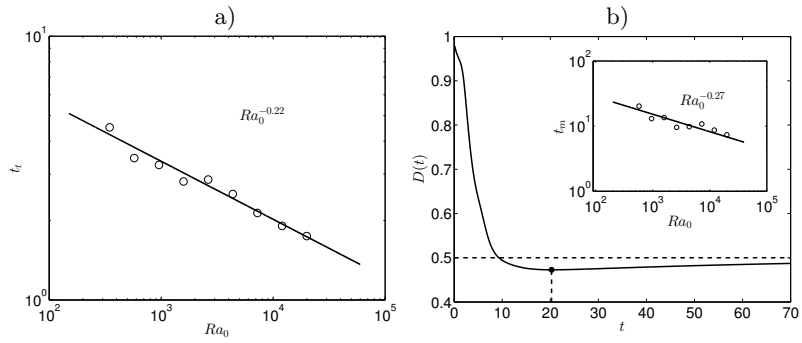

FIGURE 6.9 – Panel a) Time required to the fingers to reach the boundaries (t_t) as a function of Ra_0, well approximated by the correlation $15.3 \times Ra_0^{-0.22}$. In this figure, we consider $347 \leq Ra_0 \leq 19953$. Panel b) Main panel: evolution of the dissolution parameter D for $Ra_0 = 575$. Inset: behaviour of t_m, the time required to get the minimum value of $D(t)$, i.e. the maximum dissolution rate, as a function of Ra_0. We consider $347 \leq Ra_0 \leq 19953$ and we observe that t_m is in fair agreement with $97 \times Ra_0^{-0.27}$.

and we will define the border of a finger as the contour line $C(x, z) = 1/2$. Qualitative information about finger dynamics are provided by the world lines map reported in Fig. 6.10b. Here, the contour of the concentration field along the half-channel horizontal line $C(x, z = 1/2, t)$ is plotted, and the growth, elongation and merging phenomena are visible.

A quantitative estimate of the finger number is provided by the power averaged mean wave number (Zimmerman and Homsy, 1991; De Wit, 2004), described below. Consider the vertically-averaged concentration profile

$$\widetilde{C}(x,t) = \frac{1}{H}\int_0^H C(x,z,t)\ \mathrm{d}z \tag{6.27}$$

and its Fourier transform $\widehat{C}(k,t)$, being k_i the Fourier modes of $\widehat{C}(k,t)$. The power averaged mean wave number $\langle k(t)\rangle$ is defined as

$$\langle k(t)\rangle = \frac{\sum_i k_i \left|\widehat{C}(k,t)\right|^2}{\sum_i \left|\widehat{C}(k,t)\right|^2}\ . \tag{6.28}$$

Thus, we defined the power averaged mean number of fingers

$$\langle n(t)\rangle = \frac{L}{2\pi}\langle k(t)\rangle\ , \tag{6.29}$$

which can be easily compared with the number of fingers $N(t)$ computed using the plume detection algorithm presented in Sec. 3.3.1 and the comparison with $\langle n(t)\rangle$ is reported in Fig. 6.10b. Hereinafter we do not explicitly express the dependency of $\langle n\rangle$ and N on time t. Moreover, we express the

evolution of the system in terms of t/t_t. In this way, we clearly identify the finger impingement on the walls and the consequent effects.

Using the above mentioned observables and the analyses presented in Secs. 6.3.2 and 6.3.3, we provide here a description of the overall dissolution process. Initially, the flow is dominated by diffusion due to the initial condition adopted, $\mathbf{u}(t = 0) = 0$. The diffusive regime occupies a tiny portion of the overall dissolution process, and it is not explicitly indicated in Fig. 6.10. Later, newborn fingers grow. During this stage, finger number is large and dependent on the amplitude of the initial perturbation. Diffu-

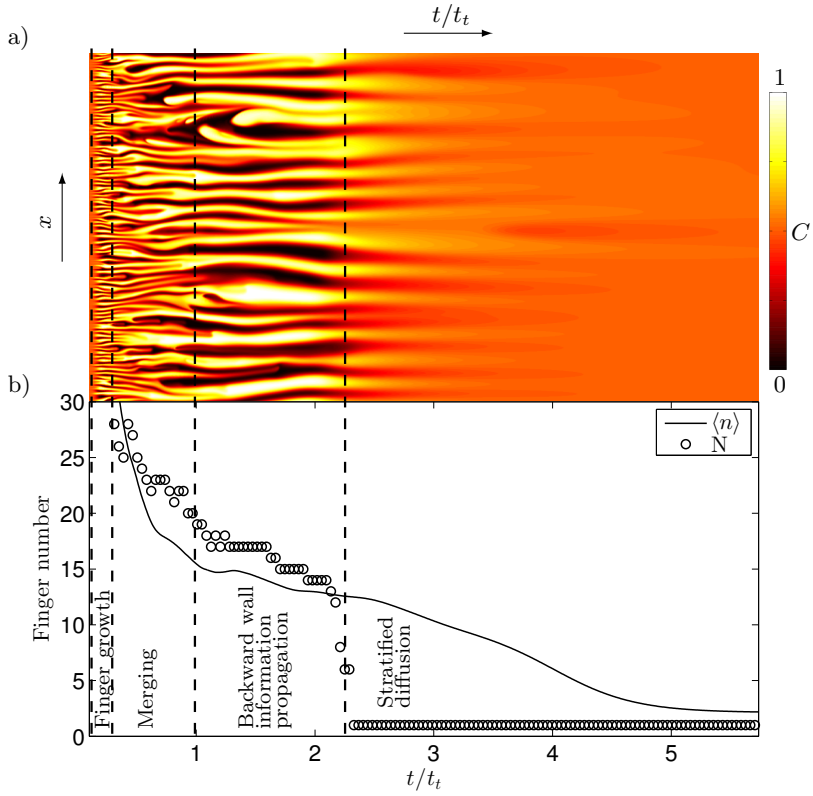

FIGURE 6.10 – Simulation performed with $Ra = 12023$ and $L = \pi/2$. Panel a) Contour map of the concentration field $C(x, z, t)$ computed along the half-channel height ($z = 1/2$) for all the simulation and reported as a function of t/t_t. Panel b) Power averaged mean wave number $\langle n \rangle$ computed as in Eq. (6.29) and plume number N, computed with the plume detection algorithm of De Paoli et al. (2016). Results show that after plume impingement ($t = t_t$) both $\langle n \rangle$ and N remain almost constant. When the boundaries presence information reaches the bulk of the domain ($t \approx 2.2 \times t_t$), N suddenly decreases to 1 whereas $\langle n \rangle$ decreases smoothly and the stratified diffusion dominates.

sion still dominates and this regime ends approximately around $t = t_t/4$. When the convective contribution becomes dominant, merging processes among the fingers occurs. The merging dynamics is recognisable in both Figs. 6.10a and 6.10b. In the latter, the finger number N along $z = 1/2$ (symbols, $\circ$) decreases. This process is similar to the one occurred in the one sided problem, described by Slim (2014), and goes on until plumes impinge on the walls ($t = t_t$). Starting from this moment, the system becomes Ra_0-dependent. The merging process is now arrested and the finger number is kept almost constant until boundaries presence information reaches the domain bulk. The higher the Ra_0, the later the instant in correspondence of which the bulk of the channel is influenced by the walls occurs. For the case considered in Fig. 6.10 ($Ra_0 = 12023$ and $L = \pi/2$), we obtained $t_t < t < 2.2 \times t_t$. An empirical observation of this phenomenon is provided by the comparison of N with $\langle n \rangle$. The finger number N computed at $z = 1/2$ and the power averaged finger number $\langle n \rangle$ decrease. Whereas the first suddenly decreases to 1, the latter lowers more smoothly. The stable diffusive regime overcomes the merging one. The averaged concentration profile $\overline{C}(z,t)$ becomes linear in z and stable ($\partial C/\partial z < 0$), and the convective transport stays aside to allow the diffusive completion of the dissolution process.

6.4 Conclusions

Rayleigh-Taylor convection in porous media is characterized by complex non-linear dynamics, which makes predictions on finger evolution and mixing efficiency hard to obtain. Furthermore, realistic geological formations are characterized by heights of tens of meters, and considered also the fluid properties, the corresponding Rayleigh numbers are of the order of 10^4. Unfortunately, high-Ra investigations are not available in literature.

In this chapter, we focused on the global Rayleigh number (Ra_0) effect on the flow features in homogeneous and isotropic porous media. With the aid of direct numerical simulations, we investigated the complex dynamics occurring in a two-dimensional satured porous layer. The numerical discretization adopted (Fourier-Chebyshev) allowed the investigation of the effect of impermeable walls on the finger dynamics. These results, not achievable with the classical double-periodic discretization (Fourier-Fourier), give a clear indication of the mixing process in presence of boundaries.

Moreover, through measurements of the local Nusselt number Nu, we linked plume the dynamics analysed in the present problem to that observed in the Rayleigh-Bénard configuration.

6.4.1 Implications for CO2 sequestration

Given the porous medium and fluid properties, all the scaling found in Sec. 6.3 can be analysed in the physical space, using the set of dimensionless variables introduced in Sec. 6.2.1.

Initially, the dissolution process is dominated by diffusion, indeed the evolution of the physical mixing length h^* results

$$h^* \sim (t^*)^{1/2} D^{1/2} \ . \tag{6.30}$$

For intermediate times the dimensionless mixing length evolves according $h \sim t^{7/5} Ra_0^{2/5}$. As above mentioned, this regime is strongly influence by the initial perturbation adopted. The corresponding dimensional form is given by

$$h^* \sim (t^*)^{7/5} \left(\frac{gk\Delta\rho^*}{\mu\Phi} \right)^{9/5} D^{-2/5} = (t^*)^{7/5} \left(\frac{W^*}{\Phi} \right)^{9/5} D^{-2/5} \ , \tag{6.31}$$

being W^* the buoyancy velocity, i.e. the velocity scale. Finally, for longer times, the asymptotic evolution is described by

$$h^* \sim (t^*)^{6/5} \left(\frac{gk\Delta\rho^*}{\mu\Phi} \right)^{7/5} D^{-1/5} = (t^*)^{6/5} \left(\frac{W^*}{\Phi} \right)^{7/5} D^{-1/5} \ . \tag{6.32}$$

These scalings provide a general idea of the advancement of the plume tips in a real geological formation.

Another important parameter is the finger impingement time ($t_t \sim Ra_0^{-0.27}$). We observed in Chap. 4 that the plume velocity was almost constant and independent of the domain size, even if it was influenced by the permeability ratio. In this case we end up with:

$$t_t^* \sim \left(\frac{gk\Delta\rho^*}{\mu\Phi} \right)^{-1.27} D^{0.27} \left(H^*\right)^{0.73} \sim \left(H^*\right)^{0.73} \ . \tag{6.33}$$

In other terms, the approximation of constant plume velocity is not valid anymore. Finally, we found that the maximum dissolution time t_m scales as $Ra_0^{-0.22}$. This suggests that the time required to dissolved a certain amount of CO_2 increases less than linearly with the domain size, i.e. $t_m^* \sim \left(H^*\right)^{0.78}$.

7

Rayleigh-Taylor convection: immiscible fluids

7.1 Introduction

In this chapter, we propose a Phase-Field Model for immiscible of fluids in porous media. This approach describes the interface between the fluids as a diffuse interface (Cahn and Hilliard, 1958), in contrast with other sharp interface (Kalisch et al., 2016) or free surface (Hirt and Nichols, 1981) methods available in literature.

Many attempts to model the interface between immiscible fluids can be found. In pure fluids, Celani et al. (2009) used a phase-field model and analyzed the linear and the weakly nonlinear stages in a Rayleigh-Taylor configuration, but in the frame of porous media few works only available. Unfortunately important differences occur when porous media are involved. Indeed immiscible fluids in porous materials are qualitatively described by the Darcy equation but a general upscale of the Navier-Stokes equation has not been achieved yet. The interface existing between two fluids is advected through the complex structure of the porous matrix, extremely irregular and heterogeneous, which makes approximations on the volume and scale of the pores hard to obtain. Only few works (Schmuck et al., 2012, 2013, 2014) propose rigorous derivations of the Darcy equation in porous media, provided that specific hypothesis are fulfilled. Moreover, few phenomenological descriptions are available in literature.

Lee et al. (2002) and Glasner (2002) proposed phase-field models in Hele-Shaw configurations. The firsts, considered incompressible and quasi-incompressible flows, whereas the latter analysed fluids characterized by high viscosity contrast. More recently, Chen and Yan (2015) investigated the effect of miscibility in radial geometries, whereas Cueto-Felgueroso and Juanes (2014) designed the free energy functional to include in the Cahn-Hilliard equation, but they do not account for the Korteweg stresses.

With the aid of direct numerical simulations, we investigated the evolu-

tion of two immiscible fluids in a fluid satured and isotropic porous slab. We adopted a pseudo-spectral method (Fourier-Chebyshev) which takes into account the effect of impermeable boundaries, in contrast with the usual discretizations proposed in literature (Fourier-Fourier). We focused on a Rayleigh-Taylor configuration characterized by an initial unstable density difference profile, which represents the archetypal system considered in the investigations of buoyancy driven flows. To the best of our knowledge, this is the first work where phase-field models in porous media are solved with pseudo-spectral methods.

The present chapter is built as follows. In Sec. 7.2, we will derive a model for the description of two immiscible fluids in a Hele-Shaw geometry. The flow field is described by the Darcy law, whereas the phase-field is treated with the Cahn-Hilliard equation, based on the Ginzburg-Landau free energy. In Secs. 7.3, the problem will be formulated in dimensionless terms will be discussed. In Sec. 7.4, the numerical procedure adopted will be described. The model is governed by three dimensionless parameters, and their significance and influence on the flow dynamics is illustrated in Sec. 7.5. Based on the numerical results observed in Chap. 6, we set the model in order to reproduce qualitatively the main dynamics observed in the miscible case, and the results will be described in Sec. 7.6. Finally, we will draw conclusions and highlight differences with the miscible case presented in Chap. 6.

7.2 The model

We assume that Hele-Shaw geometry mimics the behaviour of two immiscible fluids in an isotropic porous medium. Moreover we assume that the fluids have the same constant viscosity μ. Due to the incompressibility of the fluids, the flow obeys the continuity equation:

$$\nabla \cdot \mathbf{u}^* = 0 \ . \tag{7.1}$$

As mentioned above, the flow is governed by the Darcy law. According to this equations, the fluid velocity $\mathbf{u}^*$ is proportional to the pressure gradient ∇p^*. Moreover, we assume that the fluids are characterized by densities ρ_1^* and ρ_2^*, being $\rho_1^* > \rho_2^*$. We consider density variation effects non-negligible only in the buoyancy term within the Darcy equation (Oberbeck-Boussinesq approximation, see Chap. 2). The Korteweg stresses are the result of locally-steep concentration gradients which tend to stabilize the displacement (Chen et al., 2001). These stresses, together with the buoyancy, represent part of the coupling between the phase-field and the Darcy models.

Accounting for all the effects described above, Darcy equation becomes:

$$\frac{\mu}{k}\mathbf{u}^* = -\nabla p^* - \rho^* \mathbf{g} + \nabla \cdot \tau^* \tag{7.2}$$

where τ^* represents the Korteweg stress tensor (Lee et al., 2002) whereas $\mathbf{g}$ is the acceleration due to gravity, which contains the remaining part of the coupling between the models through the fluid density.

As previously mentioned, the phase-field model plays a key role in this chapter, indeed it describes the evolution of the phases. Both phases are identified by a single eulerian parameter ϕ^*, which is called phase variable. In this case, it describes the equivalent concentration (or normality). It is defined as $\tilde{n}_1 - \tilde{n}_2$, being $\tilde{n}_i$ the moles of the phase i divided by the volume of the solution. As a consequence, the phase variable ϕ^* is governed by the equation

$$\rho_0^* \left(\frac{\partial \phi^*}{\partial t^*} + \mathbf{u}^* \cdot \nabla \phi^* \right) = \nabla \cdot (M \nabla \eta^*) \tag{7.3}$$

where $\rho_0^* = (\rho_1^* + \rho_2^*)/2$ is the mean density and M is a mobility (or Onsager) coefficient, which can be a function of ϕ^*. In leading order, we assumed M as a constant. The chemical potential η^* is derived (Gurtin et al., 1996) from the Gibbs free-energy $E^*(\phi^*)$

$$E^*(\phi^*) = \int_D f(\mathbf{x}, \phi^*, \nabla \phi^*) d^3\mathbf{x} = E_H^*(\phi^*) + \frac{1}{2} \xi |\nabla \phi^*|^2 \tag{7.4}$$

being $\mathbf{x}$ a point of the domain D, f a function and ξ and a positive coefficient representing the mixing energy (source of surface tension). For further details on the Gibbs free energy, see Cahn and Hilliard (1958) and Lamorgese et al. (2011). Moreover the specific Helmoltz energy $E_H^*(\phi^*)$, also know as Ginzburg-Landau free energy, for immiscible fluids is defined (Yue et al., 2004) by

$$E_H^*(\phi^*) = \frac{\alpha}{4} \left(\phi^* - \sqrt{\frac{\beta}{\alpha}} \right)^2 \left(\phi^* + \sqrt{\frac{\beta}{\alpha}} \right)^2 \tag{7.5}$$

with α and β constants related to the interface properties. The definition of the specific Helmoltz energy is fundamental in order to account for the miscibility of the fluids. In order to consider immiscible fluids, we adopted the same (or equivalent) double-well potential used by Wylock et al. (2012) and Gunton et al. (1983) among the others. The potential adopted shows two minima corresponding to the two stable fluid phases. Nevertheless, by changing the expression of E_H^*, is possible to study miscible fluids. For instance, Chen and Yan (2015) suggest a detailed description of the possible expressions to adopt. Finally, we wish to remark that in the present model the miscibility of the fluids is allowed only along the interface, i.e. far from the mean concentration we are in presence of single phases.

The potential $E_H^*(\phi^*)$ is in the form of a double well potential or, in other terms, the minimum of this function corresponds to the values of ϕ^* identifying separated phases. Similarly to the mobility coefficient, ξ could be also described as a function of the phase variable ϕ^*, but in this

analysis we assume it as a constant. The chemical potential η^* is the variable that controls the interface behaviour. Using the functional derivative, we compute it as:

$$\eta^* = \frac{\delta E^*(\phi^*, \nabla\phi^*)}{\delta\phi^*} = \frac{\partial f}{\partial\phi^*} - \nabla\cdot\frac{\partial f}{\partial(\nabla\phi^*)} + \nabla^2\frac{\partial f}{\partial(\nabla^2\phi^*)} - \dots \tag{7.6}$$

and we obtain an expression similar to Mauri et al. (1996):

$$\eta^* = E_H'^*(\phi^*) - \xi\nabla^2\phi^* \ . \tag{7.7}$$

In the nearby of the interface, phenomena act in a way to minimize the value of the potential energy η^*.

The set of Eqs. (7.1)-(7.3), (7.5) and (7.7) completely describes the physical system considered.

7.3 Dimensionless equations

In literature, within the formulation of a Darcy-Boussinesq-Cahn-Hilliard problem (DBCH), few parameters (i.e. viscosity or permeability) are usually kept dimensional (Chen and Yan, 2015; Lee et al., 2002). In this work, we provide a coherent non-dimensional formulation for this model and the non-dimensionalitazion of the equation.

Continuity equation

First, we need to identify some dimensional quantities to make our equations dimensionless. Regarding the length scale, the most natural quantity to be used is the domain height H^*. The problem is initially driven by buoyancy, and the existing vertical density difference suggests to adopt H^* rather than L^* as a reference scale, as we did in the previous chapters. As velocity scale we adopt the buoyancy velocity, defined within the Darcy equation (Eq. (7.2)) by the equilibrium of the of the pressure term and the gravity term (i.e. neglecting Korteweg stresses and pressure gradient), by replacing the density with its maximum difference $\Delta\rho^* = \rho_1^* - \rho_2^*$, i.e. the difference between the pure fluids densities. This buoyancy velocity represents the rising velocity of a parcel of fluid with density ρ_2^* immersed in a volume of fluid with density ρ_1^*. This approach was also commonly adopted in previous works. In view of this, we obtain:

$$x^*, z^* \sim H^* \qquad , \qquad u^*, w^* \sim W^* = \frac{kg\Delta\rho^*}{\mu} \tag{7.8}$$

and the continuity equation (7.1) reduces to

$$\nabla\cdot\mathbf{u} = 0 \ . \tag{7.9}$$

Chemical potential

The energy density E^* and the phase variable ϕ^* can be scaled using E_0^* and ϕ_0^* respectively, defined as a function of the interface parameters α and β. At this point, we need a parameter that allows to measure the dispersion of the model (Chen and Yan, 2015), and this is the Cahn number Ch:

$$E^*(\phi^*) \sim E_0^* = \frac{\beta^2}{\alpha} \quad , \quad \phi^* \sim \phi_0^* = \sqrt{\frac{\beta}{\alpha}} \quad , \quad Ch = \frac{\xi(\phi_0^*)^2}{(H^*)^2 E_0^*} \ . \tag{7.10}$$

It is possible to show that Ch represents also a measure of the interface thickness (Lee et al., 2002). From Eq. (7.4) results:

$$E(\phi) = E_H(\phi) + \frac{1}{2} Ch \left|\nabla\phi\right|^2 \ . \tag{7.11}$$

Using then the following dimensionless quantity

$$\eta^* \sim \eta_0^* = \frac{E_0^*}{\phi_0^*} \tag{7.12}$$

from Eq. (7.7) we obtain for the potential

$$\eta = E'_H(\phi) - Ch\,\nabla^2\phi \tag{7.13}$$

or, in other terms:

$$\eta = \phi^3 - \phi - Ch\,\nabla^2\phi \ . \tag{7.14}$$

Cahn-Hilliard equation

The interface is governed by Eq. (7.3), also know as Cahn-Hilliard equation (Cahn and Hilliard, 1958). Assuming that the mobility coefficient M is independent of ϕ^*, the r.h.s. of Eq. (7.3) can be rewritten as the laplacian of the chemical potential η^*. The time scale used to make this equation dimensionless is a combination of the velocity and length scales previously introduced. Furthermore, we need also a parameter (Chen and Yan, 2015; Lee et al., 2002) accounting for the model dissipation (i.e. it has a numerical but not an explicit physical interpretation), and this is the diffusive Peclet number Pe. We finally use the mean density ρ_0^* (introduced in Sec. 7.2) and results:

$$t^* \sim T^* = \frac{H^*}{W^*} \qquad , \qquad Pe = \frac{\rho_0^* (H^*)^2 (\phi_0^*)}{M\eta_0^* T^*} \ . \tag{7.15}$$

Eq. (7.3) in dimensionless terms results:

$$\frac{\partial\phi}{\partial t} + \mathbf{u}\cdot\nabla\phi = \frac{1}{Pe}\nabla^2\eta \tag{7.16}$$

and also in this case the density variation was neglected.

Darcy-Boussinesq equation

Finally, the velocity field is governed by Eq. (7.2). The dimensionless pressure adopted to rescale the pressure term is:

$$p^* \sim p_0^* = \frac{\mu W^* H^*}{k} \ . \tag{7.17}$$

The buoyancy term $\rho^* \mathbf{g}$ depends on the quantity of both phases, i.e. on the phase variable ϕ^*, as follows:

$$\rho^* = \frac{1}{2}\left[\left(1+\frac{\phi^*}{\phi_0^*}\right)\rho_1^* + \left(1-\frac{\phi^*}{\phi_0^*}\right)\rho_2^*\right] = \frac{\partial(\rho_0^* z^*)}{\partial z^*} + \frac{\Delta\rho^*}{2}\phi \tag{7.18}$$

and according to this formulation, the vertical gradient $\partial(\rho_0^* z^*)/\partial z^*$ is easily included into the pressure gradient. Similarly, the Korteweg term can be rewritten as follows (see also Appendix 3.A):

$$\nabla \cdot \tau^* = -\xi \nabla \cdot (\nabla\phi^* \otimes \nabla\phi^*) \tag{7.19}$$

$$= -\xi\left[\nabla^2\phi^*\nabla\phi^* + \nabla\left(\frac{1}{2}\left|\nabla\phi^*\right|^2\right)\right] \tag{7.20}$$

$$= [\eta^* - E_H'^*(\phi^*)]\nabla\phi^* - \nabla\left[\frac{1}{2}\xi\left|\nabla\phi^*\right|^2\right] \tag{7.21}$$

$$= \eta^*\nabla\phi^* - \nabla\left[\frac{1}{2}\xi\left|\nabla\phi^*\right|^2 + E_H^*(\phi^*)\right] \ . \tag{7.22}$$

At this point, it results numerically convenient to define a modified pressure P^*:

$$P^* = p^* + \rho_0^* g z^* + \frac{1}{2}\xi\left|\nabla\phi^*\right|^2 + E_H^*(\phi^*) \tag{7.23}$$

and Eq. (7.2), reduces to the dimensional form:

$$\frac{\mu}{k}\mathbf{u}^* = -\nabla P^* - \phi\frac{\Delta\rho^*}{2}\mathbf{g} + \eta^*\nabla\phi^* \ . \tag{7.24}$$

In this problem, the scaling is done comparing forces due to buoyancy and interface, and as a consequence we take into account the surface tension σ. The dimensionless group that refers to the relative importance of these two contributions is the Bond (or Eötvös) number Bo, defined as:

$$Bo = \frac{g\Delta\rho^*\left(H^*\right)^2}{\sigma} \tag{7.25}$$

where the surface tension σ was computed as in Yue et al. (2004) and results:

$$\sigma = \xi\int_{-\infty}^{+\infty}(\nabla\phi^*\cdot\mathbf{n})^2 d\mathbf{n} = \frac{2\sqrt{2}}{3}\sqrt{\xi E_0^*(\phi_0^*)^2} \ , \tag{7.26}$$

being $\mathbf{n}$ the unit vector normal to the interface. Similarly, we define the z-direction unity vector $\mathbf{k}$ and the dimensionless form of Eq. (7.24) finally becomes:

$$\mathbf{u} = -\nabla P + \frac{\phi}{2}\mathbf{k} + \frac{3\sqrt{2}}{4}\frac{1}{Bo\sqrt{Ch}}\eta\nabla\phi \ . \tag{7.27}$$

The set of Eqs. (7.9), (7.14), (7.16) and (7.27) represents the DBCH model.

7.4 Methodology

In this section, we will summarize numerical strategy and initial conditions. Moreover, we will provide some theoretical details on the equilibrium solution of the concentration field in a simplified configuration.

7.4.1 Numerical scheme

We solved Eqs. (7.9), (7.14), (7.16) and (7.27) using a pseudo-spectral Chebyshev-Tau method. The numerical algorithm adopted for the solution of the Eq. (7.27), i.e. for the determination of the flow field, is the same presented in Appendix 3.A.1, with the exception of the Korteweg term, which is included into the non-linear term. Indeed, the velocity field $\mathbf{u}$ can be explicitly determined as well as the chemical potential η, from Eqs. (7.27) and (7.14) respectively. Finally, the phase variable ϕ is computed. Details on the method adopted to solve Eq. (7.16) and on the time advancement scheme are provided in Appendix 7.A.2.

7.4.2 Equilibrium solutions

The relative concentration equilibrium profile across the interface is given by the competition of two terms appearing in the free energy formulation, and can be determined by minimizing the free energy functional defined by Eq. (7.11), i.e. $E[\phi(\mathbf{x})]$. Consider a flat and horizontal interface between two fluid layers. In this configuration, the concentration profile is simply given by the one-dimensional solution of Eq. (7.14)

$$\frac{\delta E[\phi]}{\delta\phi} = 0 \rightarrow \phi^3 - \phi - Ch\frac{\partial^2\phi}{\partial z^2} = 0 \tag{7.28}$$

which has a particular solution:

$$\phi(z) = \tanh\left(\frac{z - 1/2}{\sqrt{2\,Ch}}\right) \tag{7.29}$$

and two constant solutions ($\phi = \pm 1$). Eq. (7.29) represents the concentration profile at the equilibrium.

7.4.3 Initial/boundary conditions and validation

With the exception of the particular one-dimensional solution provided in Sec. 7.4.2, the Cahn-Hilliard equation has no trivial solution, which makes code validation hard to obtain. We used three different initial conditions: symmetric stable, symmetric unstable and non-symmetric initial concentration profiles, and we check if the final attained state is recovered. Moreover, we used some global quantities to evaluate the accuracy of the results.

In the symmetric stable condition, we initialize the flow with the concentration profile perturbed:

$$\phi(x,z) = -\tanh\left(\frac{z-1/2}{\sqrt{2}\,Ch}\right) + \varepsilon(z) \tag{7.30}$$

being

$$\varepsilon(z) = \begin{cases} 0 & , \quad \text{if } z \neq 1/2 \\ \psi & , \quad \text{if } z = 1/2 \end{cases} \tag{7.31}$$

where ψ represents a random value with $|\psi| < 0.05$ and the phase-field has to remain unaltered (stable stratification). In other terms, we perturb the concentration field at half-channel height, whereas $\mathbf{u}(t=0) = 0$ everywhere. Then, an unstable symmetric density profile, defined by

$$\phi(x,z) = \tanh\left(\frac{z-1/2}{\sqrt{2}\,Ch}\right) + \varepsilon(z) \tag{7.32}$$

has been considered and, for very long times, the stable configuration of Eq. (7.29) is recovered. Finally, we initialized the flow with a non-symmetric unstable configuration, where the volume of the heavy fluid is one fourth of the total volume, i.e. the interface is initially at $z = 3/4$. Even in this case the stable configuration corresponding to the position of the interface at $z = 1/4$ is recovered for very long times.

In order to evaluate the accuracy of the results, we computed throughout all the simulations some quantities that account for the volume conservation of each single fluid and of the total volume of fluids. We are interest in to evaluate, in each time instant t, the mass conservation of the whole phase variable ϕ:

$$I(t) = \frac{1}{V}\int_V \phi(\mathbf{x},t)dV = \frac{1}{H}\int_H \overline{\phi}(\mathbf{x},t)dz \tag{7.33}$$

being $V = [0;L]\times[0;H]$ the volume of fluid and $\overline{\phi}$ the horizontally-averaged concentration profile. Moreover, it is important to ensure that each phase is conserved, i.e. $I(t) = 0$, $\forall t \geq 0$ when the two fluids have initially the same volume $V/2$. With respect to each single phase, we are also interested in to measure the conservation of volume. For instance, for the heavy fluid (ρ_1^*), which initially occupies a volume V_1, the quantity

$$I_1(t) = \frac{1}{V_1}\int_{V_1} \phi(\mathbf{x},t)dV_1 \tag{7.34}$$

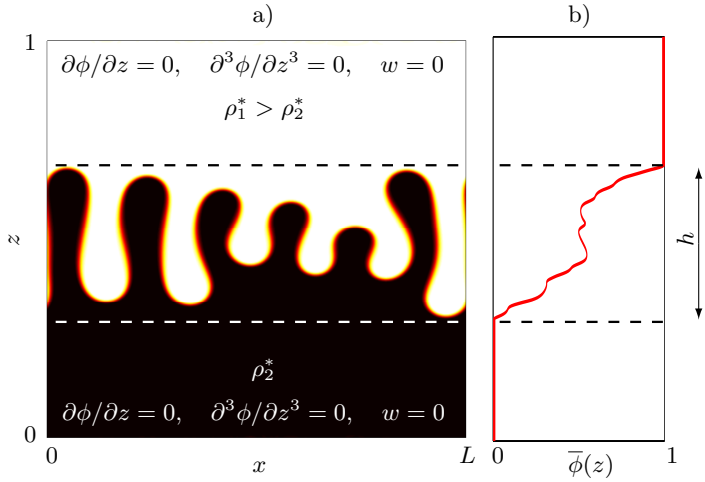

FIGURE 7.1 – Panel a) Sketch of the computational domain with explicit indication of the boundary conditions employed. The contour map of the solute concentration ϕ at a given time instant t is also shown to provide a flow visualization of the dynamics for the present physical configuration (heavy fluid layer standing above a lighter one, white and black respectively). Panel b) Horizontally-averaged concentration profile $\overline{\phi}(z)$. The instantaneous mixing length h is represented as the extension of the tip-rear finger region (dashed lines $--$).

has to be kept constant during the simulation. Moreover we analysed the evolution of $I_1(t)$ with respect to the initial values, $I_1(0)$, and we consider the quantity:

$$G_1(t) = \frac{I_1(t) - I_1(0)}{I_1(0)} \ . \tag{7.35}$$

An example of the behaviour of $G_1(t)$ is reported in Sec. 7.5. This quantity has be as small as possible. We investigated the influence of the parameters Bo, Pe and Ch on the volume conservation using the tools above mentioned in order to calibrate the grid on the chosen parameters.

The initial condition adopted for the simulations is the unstable density configuration, reported in Eq. (7.32). Moreover, the horizontal boundaries are impermeable ($\partial\phi/\partial z = 0$) and no penetration condition is assume ($w = 0$). Finally, the contact angle is $\pi/2$ rad, which after some algebra yields $\partial^3\phi/\partial z^3 = 0$. Boundary condition and initial flow configuration are summed up in Fig. 7.1a.

A relevant parameter involved in the study of flows with interface is the mixing length h, which has been introduced in Sec. 6.2.1, and we recall here briefly. It represents the distance between the rear and the tip of the fingers-like structures. According to De Wit (2004), we choose to identify the mixing zone, whose dimensionless extension is h, as the portion of the domain where $-1 + 2\varepsilon < \overline{\phi}(z,t) < 1 - 2\varepsilon$, with $\varepsilon = 10^{-2}$ and being $\overline{\phi}(z,t)$

the horizontally-averaged concentration profile, defined as:

$$\overline{\phi}(z,t) = \frac{1}{L}\int_0^L \phi(x,z,t)dx \ . \tag{7.36}$$

A physical interpretation of the mixing length is provided in Fig. 7.1b, where an instantaneous horizontally-averaged concentration profile is also plotted $\overline{\phi}(z)$.

We performed two-dimensional direct numerical simulations exploring a wide range of values for the parameters Pe, Ch and Bo. In Sec. 7.5, we will analyse the influence of the parameters on the flow dynamics. Finally, in Sec. 7.6 we will report the results obtained by tuning the parameters in order to have the same macroscopic behaviour observed for the miscible fluid configuration in Chap. 6.

7.5 Influence of the parameters

The analysed flow follows a complex time-dependent evolution, strongly related to the initial perturbation. The aim of this section is to study the effect of the governing parameters on the flow topology and on the evolution in time of the finger-like structures. In order to account only the influence of the parameters, we fixed a grid (1024×513 collocation points) and explored a range of values of Pe, Ch and Bo compatible with the grid given. In such a way, the initial perturbation is exactly the same in each simulation considered.

Bond number effect

We recall here that the Bond Number measures the relative strength of gravitational (proportional to $\Delta\rho^*$) and surface tension (σ) forces (Lee et al., 2002). If the Bond number increases, the intensity of surface tension forces

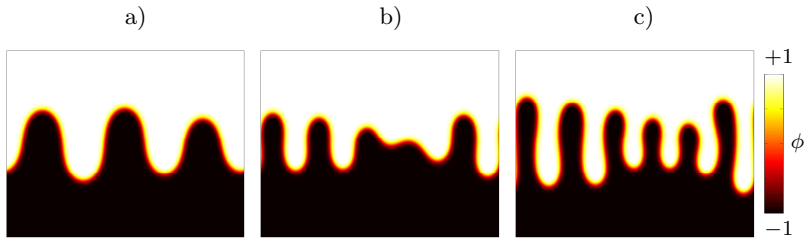

FIGURE 7.2 – Effect of the Bond number on fingers number. In these panels the phase-field ϕ is represented. Simulations have been performed at $Pe = 250$ and $Ch = 2\times10^{-4}$ by increasing the Bond number, i.e. decreasing the relative importance of the surface tension with respect to the buoyancy. Panel a) $Bo = 10^2$ and $t = 7.4$. Panel b) $Bo = 5 \times 10^2$ and $t = 4.4$. Panel c) $Bo = 10^3$ and $t = 4.4$.

decreases and the interface between the fluids becomes more deformable (see Lamorgese and Mauri (2015) for further details). The curvature of the structures increases as well as the computational cost required to fully describe the interface. On the other hand, the structures have a smaller characteristic size (Fig. 7.2a-c). We wish to remark that all these simulations have been performed on the same grid and with the same initial perturbation ε. In this way, the effect of the single parameters is straightforward.

On the other hand, when the Bond number exceeds a certain value, depending also on the value of the parameters Pe and Ch, its influence on the structures size is negligible. We observed this phenomenon further increasing the Bond number up to 2×10^4, but keeping constant values for $Pe = 250$ and $Ch = 2 \times 10^{-4}$.

Peclet number effect

The Peclet number Pe has important effects on the simulation, both on the numerical and physical point of view. It is inversely proportional to the diffusion coefficient in Eq. (7.16).

On the numerical point of view, for given Bo and Ch, to increase the Peclet number means to increase considerably the mass loss. In particular, many simulations for a wide range of values of the parameters ($25 \times 10^{-6} \leq Ch \leq 1 \times 10^{-4}$, $4 \times 10^3 \leq Bo \leq 10^5$ and $250 \leq Pe \leq 16 \times 10^3$) have been performed, varying Pe for couples of values of Bo and Ch. This series of simulations confirm the negative influence of the Peclet number increase on the mass loss. On the other hand, an increase of Pe makes the overshoot (Gibbs phenomena) larger, but more localized in space.

On the physical point of view, the structures size is also affected by the Peclet number. In particular, we observe that for $Bo = 10^5$, if Pe increases, the dominant wavelength calculated at half channel decreases. For $Bo \sim 10^4$, this effect strongly is reduced in intensity, and the wavelength remains unchanged. On the other hand, the flow develops faster for increasing Pe.

Cahn number effect

The Cahn number Ch is proportional to the ratio of the interface thickness to the domain height. In turbulence, the value Ch is usually considered as small as possible, compatibly with the grid adopted, due to the fact that the interface is, practically, very thin compared to the problem size. This is the case of a bubble, which has an interface thickness ($\sim 10^{-7}$ m) many orders of magnitude smaller compared to the bubble diameter ($\sim 10^{-2}$ m). Due to computational limits, Ch will never be small enough to describe the real thickness. However, we choose Ch in a way to have an accurate numerical description of the phenomena in the interface region. We performed a number of simulations by keeping Bo and Pe constants and varying Ch, and the results show that the smaller Ch, i.e. the smaller

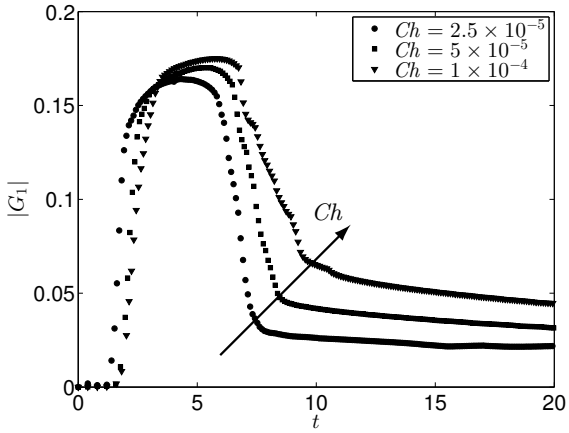

FIGURE 7.3 – Mass loss computed as in Eq. (7.35) for three different values of the Cahn number, with $Bo = 10^5$ and $Pe = 250$. Increasing Ch, the mass loss $|G_1|$ increases and, in order to reduce this effect, we choose the smallest Ch possible and compatible with a given grid.

interface thickness, the lower the mass loss. In Fig. 7.3 this situation is represent, and the higher the Cahn number, the higher the mass loss. The mass loss is considerably high here, and this is due to the small Peclet number ($Pe = 250$) adopted during these tests, mentioned in Sec. 7.5.

7.6 Results

In this section, we provide a complete analysis of the results obtained for different values of the parameters Bo, Ch and Pe. The simulations performed and analysed in detail, marked as "S1, S2 ... S9", are summed up in Tab. 7.1. In order to compare the results obtained using the Phase-Field Model (present chapter) with those obtained with the classical advection-diffusion equation (Chap. 6), we set a Cahn number $Ch = 7.8125 \times 10^{-5}$ for S6-S9, which provides an equivalent initial concentration profile between the two classes of simulations (i.e. equivalence of the concentration profiles given by Eqs. (6.14) and (7.32)). All the simulations have been performed on the same grid (1024×513 collocation points.)

In Sec. 7.6.1 the overall evolution of the flow will be described. In Sec. 7.6.2, the simulations S1-S9 will be presented, and some important quantities will be discussed more in detail, with particular attention to the dependency of this quantities on the Bond number.

7.6.1 Qualitative analysis

Here we provide a qualitative description of the evolution of a representative system (simulation S4 in Tab. 7.1). Then, a semi-quantitative and a

TABLE 7.1 – Simulations performed: we consider two different combinations of Pe and Ch and for each of them we investigated different values of Bo.

Name	Bo	Pe	Ch
S1	1×10^3	5×10^4	5×10^{-5}
S2	2×10^3	5×10^4	5×10^{-5}
S3	5×10^3	5×10^4	5×10^{-5}
S4	1×10^4	5×10^4	5×10^{-5}
S5	2×10^4	5×10^4	5×10^{-5}
S6	5×10^2	2×10^4	7.8×10^{-5}
S7	1×10^3	2×10^4	7.8×10^{-5}
S8	2×10^3	2×10^4	7.8×10^{-5}
S9	8×10^3	2×10^4	7.8×10^{-5}

quantitative analysis will be also considered, where mixing length and other relevant observables are investigated.

In Fig. 7.4, instantaneous concentration fields are plotted for different time instants. The interface is initially flat (Fig. 7.4a) but the Bond number is not large, i.e. the Korteweg stresses strength is not sufficient to contrast the gravitational counterpart, and finger like instabilities arise (Fig. 7.4b). Due to the immiscibility of the fluids, the number of fingers remains constant throughout the simulation (Figs. 7.4c-h). However, some merging phenomena occur just above half-channel height in Figs. 7.4h-i. After a while, around $t \approx 3$, the finger impinge on the boundaries. Before this event the system was independent of the walls, i.e. independent of H^*. Since this moment its evolution becomes H^*-dependent. This is in agreement with the arguments discussed in Sec. 6.3.3 and related discussion. Indeed, we will analyse the same characteristic quantities (for instance the time required to the fingers to reach the walls) and we will compare these quantities obtained with the two different models adopted.

An important feature of the analysis performed is that we take into account the presence of the boundaries, due to the discretization adopted (Fourier-Chebyshev). Indeed, most of the studies regarding Rayleigh-Taylor convection, both in miscible or immiscible porous fluids, are performed on periodic domains in vertical and horizontal directions (Fourier-Fourier). This represents an important achievement, which allows to obtain precise information of the flow dynamics in the nearby of the boundaries.

A more quantitative estimate of the system is given by the horizontally-averaged concentration profiles reported in Fig. 7.5. These profiles refer to same instants shown in Fig. 7.4. The interface between the fluids is initially flat (dashed line, $--$). Then, close to the interface the domain is perturbed. This perturbation propagates towards the horizontal boundaries. Consider, for instance, the instant $t = 1.36$. From Fig. 7.5 we observe that the profile is unperturbed for approximately $z < 0.4$ and $z > 0.6$. The extension of this zone corresponds roughly to the instantaneous mixing length $h(t = 1.36)$.

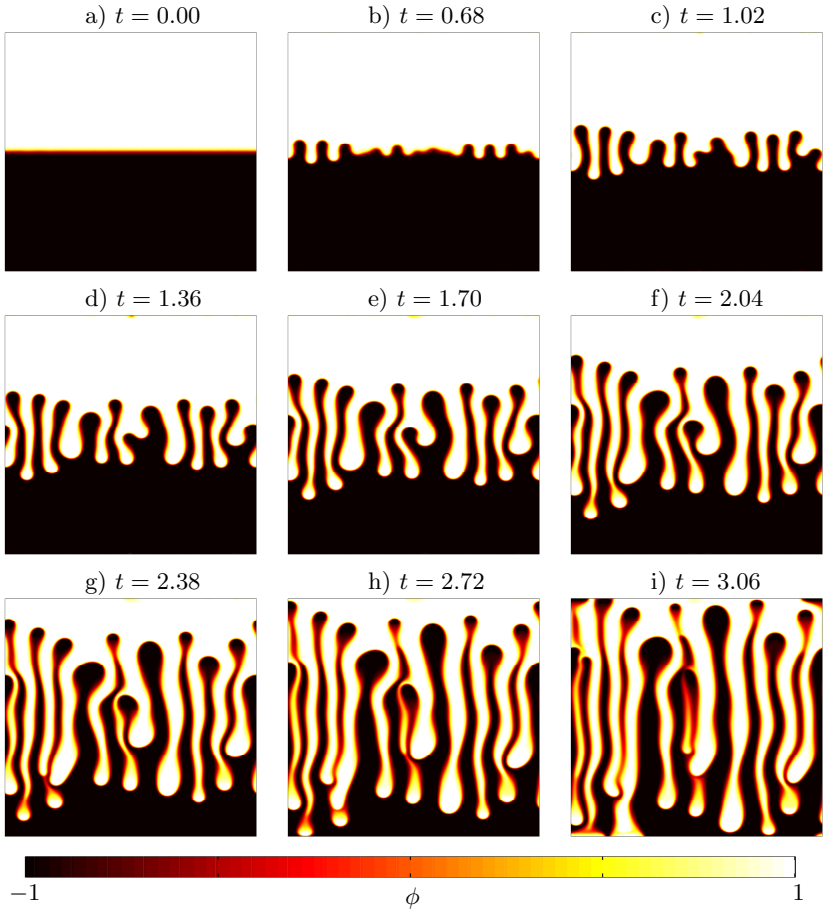

FIGURE 7.4 – Instantaneous concentration fields have been reported at different instants, before the impingement of the fingers on the walls. This fields are computed for $Bo = 10^4$, $Pe = 5 \times 10^4$ and $Ch = 5 \times 10^{-5}$ (S4 in Tab. 7.1). The aspect ratio is $L = \pi/4$. Instantaneous horizontally-averaged concentration profiles are plotted in Fig. 7.5.

Finally, for $t > 3$, fingers impinge on the channel walls and the averaged profiles are perturbed everywhere.

The evolution of such a system can be investigated using world lines contour maps of the concentration field ϕ, following the approach adopted in previous chapters (Fig. 7.6). The world lines measurements of ϕ are made along two horizontal slices located at the centerline of the domain, i.e. $z = 1/2$ (panel a), and close to the upper boundary, i.e. at $z = 0.98$ (panel b). Finally, on panel c), the number of finger N computed with the plume detection algorithm and the power averaged mean number of fingers $\langle n \rangle$ (see Secs. 3.3.1 and 6.3.4 respectively) are shown. In this way, we are

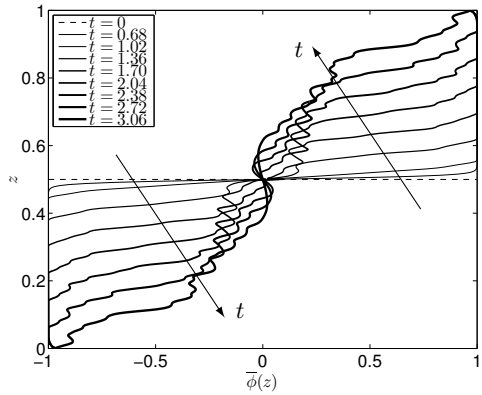

FIGURE 7.5 – Instantaneous horizontally-averaged concentration profiles $\overline{\phi}(z)$ at different times before the impingements of the fingers on the walls, i.e. $h < 1$ (simulation S4). The simulation and the instants considered are the same represented in Fig. 7.4. Profiles are have been symmetrized with respect to the half-channel plane. Direction of time is also reported.

able to analyse the dynamics occurring at the channel height and in the nearby of the upper wall (and likewise at the lower boundary) both on the qualitative and semi-quantitative point of view. The exemplar simulation considered is S4.

First, we observe that important flow modifications occur in correspondence of the cutting planes. In particular, at half-channel height (Fig. 7.6a), is clearly visible a change in the plume number. Around $t \approx 0.75$, the fingers are well defined, and this reflects a sudden increase of the finger number N. We define this as the onset of convection, occurring at time t_o.

Then fingers grow towards the walls. During this elongation-phase no relevant merging phenomenon occurs, indeed $\langle n \rangle$ and N are both constant. Finally the fingers reach the upper wall at the time t_t, and a footprint is registered on the map reported in Fig. 7.6b. Moreover, an additional information is provided by this map. Indeed the track diameter increases in time, which reflects a narrow shape for the fingers in the nearby of the walls, due to the redistribution of the light fluid. This redistribution effects are strongly influenced by the porous medium permeability tensor, as show in Sec. 4.4 and the effect of anisotropy should be consistent and will probably modify the following dynamics.

The relevant observables described in the previous analyses (the mixing length h, the onset time t_o and the impingement time t_t) will be considered quantitatively and on a wide range of value of the Bond number Bo in the following section.

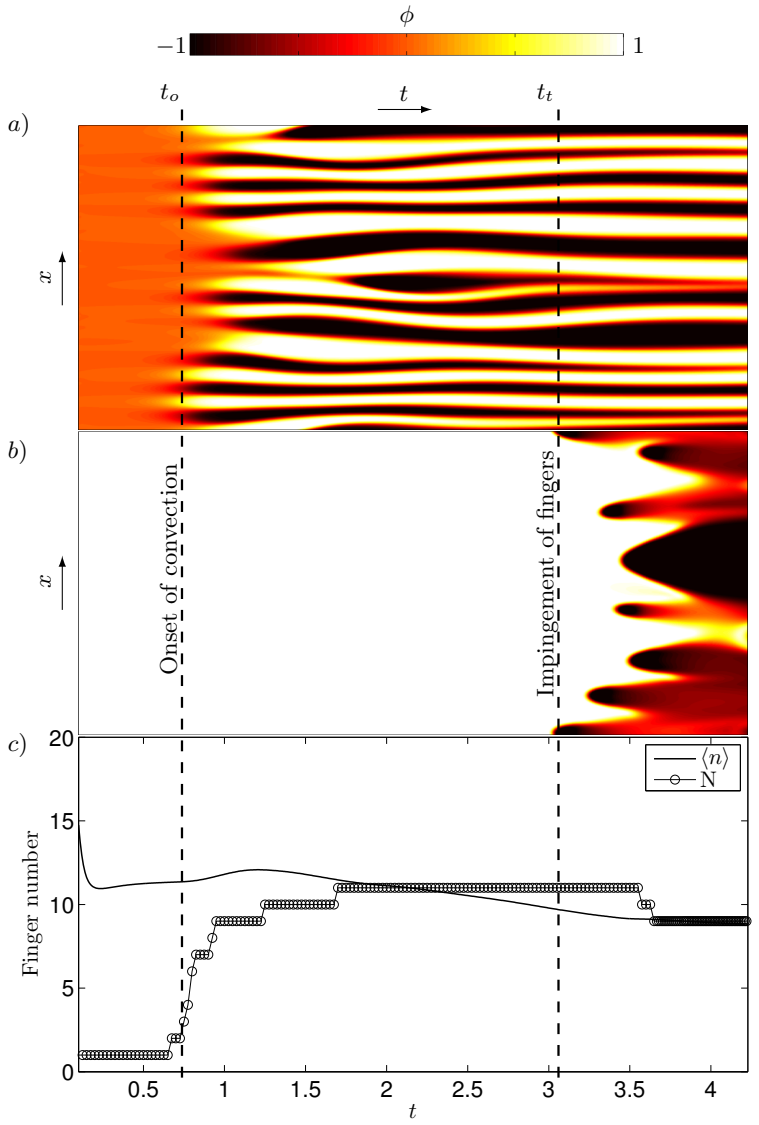

FIGURE 7.6 – Panels a) and b) World lines measurements of ϕ along two horizontal slices located at half channel height, i.e. $z = 1/2$ (a), and close to the upper boundary, i.e. $z = 0.98$ (b). Panel c) The power averaged mean finger number (solid line, $-$), $\langle n \rangle$, and the finger number computed with the plume detection algorithm (symbols, $\circ$), N, are also plotted as a function of time t. The onset of convection t_o and the instant in correspondence of which the finger impinge on the walls t_t are also reported (dashed lines, $--$). The simulation considered is S4.

7.6.2 Quantitative analysis

In this section, we will present the results related to the simulations S1-S9. We will focus on the Bond number. According to the analyses presented in Secs. 7.5 and 7.5, the Cahn number is the smallest possible compatible with a given grid, whereas the Peclet number should be the highest possible, in order to reduce the dispersion of the model. Both these parameters are strictly connected with the grid resolution, indeed some expressions providing Pe as a function of Ch for pure fluids are available in literature (Magaletti et al., 2013). These is a clear indication of the fact that the parameters Pe and Ch have mainly a numerical meaning in the context of the phase-field models. Therefore, we chose to study the simulations as a function of the Bond number for a given set of Peclet and Cahn numbers.

In the frame of CO_2 sequestration, the fluid parameters are usually known, as well as the interface properties, which depend on to the fluids adopted. Therefore, the domain size H^* is the only relevant parameter. From Eq. (7.25) we end up with $Bo \sim (H^*)^2$ or, in other terms, $H^* \sim \sqrt{Bo}$. Moreover, in Sec. 7.6.1 we discussed the independence of the flow with respect to the domain boundaries until the finger reach the walls. Thus, we assume that for a given pair of Ch and Pe, the evolution of the flow should be the same until the first finger impinges on the upper/lower boundary.

The mixing length is the parameter that provides a clear indication of the evolution of the system in this terms. According to the above mentioned scaling, we plot the evolution of $h \times \sqrt{Bo}$ in time for all the simulations S1-S9 considered, and the results are shown in Fig. 7.7. First, we observe that upon this scaling, the agreement among the simulations is excellent. Moreover, this behaviour reflects the fact that within the range of Ch and Pe considered, the influence of these parameters is limited. Indeed, the difference between S1-S5 ($Pe = 5 \times 10^4$ and $Ch = 5 \times 10^{-5}$) compared to S6-S9 ($Pe = 2 \times 10^4$ and $Ch = 7.8 \times 10^{-5}$) is negligible.

Furthermore, we observed that the evolution of the system can be essentially divided in two distinct regimes:

- after the onset, the rescaled mixing length evolves according to $h \sim (t\sqrt{Bo})^5$. In other terms, rewriting the scaling law for the mixing length, we get
$$h \sim t^5 \, Bo^2 \quad . \tag{7.37}$$
- later, the mixing length grows as
$$h \sim t^{3/2} \, Bo^{1/4} \quad . \tag{7.38}$$
During this stage, each single simulation departs form the asymptotic behaviour as soon as it reaches the wall (i.e. $h = 1$), indeed the horizontal lines in Fig. 7.7 correspond to the values $\sqrt{Bo}$.

We also observe that with the exception of S5 and S9, which depart from overall trend, all the simulations exhibit a nice agreement during the whole

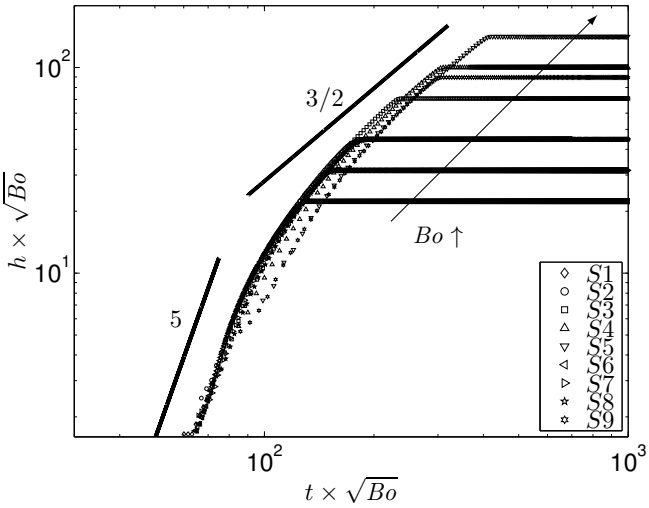

FIGURE 7.7 – The mixing length h is plotted as a function of time, both rescaled by $\sqrt{Bo}$. Two different regimes are identified: when the onset occurs, the interface evolves initially as $h \sim t^5\, Bo^2$, then the growth follows the scaling $h \sim t^{3/2}\, Bo$.

evolution. The reason why the behaviour of S5 and S9 slightly differs from the others is unclear.

Finally, two more quantitative parameters in which we are interested in, are the onset time (t_o) and the time required to the fingers to reach the walls (t_t), both introduced in Sec. 7.6.1 and reported as a function of the Bond number in Fig. 7.8. The onset time is defined as the time required to the mixing length to be greater then $h_0 + \epsilon$, being h_0 the initial mixing length, derived from Eq. (7.29), and $\epsilon = 10^{-2}$. Similarly, t_t is the time required to the mixing length to become grater than $1 - \epsilon$.

Once again, we observe in Fig. 7.8 that range of Pe and Ch considered does not involve important changes in terms of onset and impingement. Indeed, at low Bond numbers ($Bo = 10^3$ and $Bo = 2 \times 10^3$) both t_o and t_t coincide for the values of Ch and Pe considered. Furthermore, the agreement is kept for higher Bo and the data are well fitted by the correlations:

$$t_o \sim Bo^{-0.38} \quad , \quad t_t \sim Bo^{-0.19} \quad . \tag{7.39}$$

7.7 Conclusions

In this chapter, Rayleigh-Taylor convection of immiscible fluids in porous media is analysed. This unstable flow is characterized by complex nonlinear dynamics, which makes predictions on mixing length and interface deformation hard to obtain.

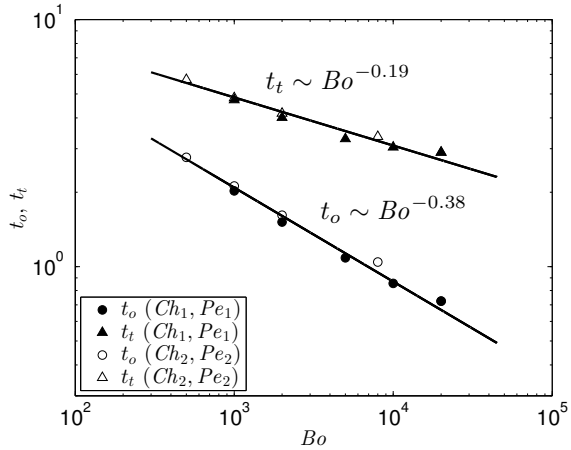

FIGURE 7.8 – The onset time t_o (●, ○) and the time required to the fingers to impact on the horizontal boundaries t_t (▲, △) are plotted as a funtion of the Bond number (Bo). Filled symbols refer to $Ch_1 = 5 \times 10^{-5}$ and $Pe_1 = 5 \times 10^4$, empty symbols refer to $Ch_2 = 7.8 \times 10^{-5}$ and $Pe_2 = 2 \times 10^4$. These quantities are well approximated by power laws reported.

First, we developed a model based on the diffuse interface approach (Cahn-Hilliard equation). In this model, the fluids are miscible along the interface only, whereas far from it the fluids are considered as pure. In spite of some particular cases, a general mathematical derivation of the Darcy equations as upscale of the Navier-Stokes equation, including Korteweg stress, is not available. Thus, the system analysed in the present chapter should be considered as a simplified model of two immiscible fluids in porous media.

With the aid of direct numerical simulations, we investigated the effects of the parameters involved (Bond, Peclet and Cahn number) on the flow features. We considered a Hele-Shaw cell, which mimics the flow in an isotropic and homogeneous porous layer. Finally, we investigated the effects of the domain size on the evolution of the flow in terms of mixing length and impingement time of the fingers.

The numerical discretization adopted (Fourier-Chebyshev) allowed the investigation of the effect of impermeable walls on finger dynamics. These results, not achievable with the classical periodic discretization (Fourier-Fourier), given a clear indication of the mixing process in presence of boundaries. To the best of our knowledge, this is the first work where phase-field models in porous media are solved with pseudo-spectral methods.

Finally, additional information are provided by the analysis of the flow structures. The finger number is investigated and a regime classification, motivated by the modifications of the flow topology, is provided.

7.7.1 Comparison with miscible fluids

In this chapter, fluids miscibility is limited along the interface. We derived some scaling laws in order to describe the onset time t_o, the impingement time t_t and the mixing length h, with respect to the most physically-relevant parameter, the Bond number Bo. It is interesting to compare these results with the corresponding miscible counterparts, presented in Chap. 6.

We found that the impingement and onset times are associated to negative exponents of Bo. However, this does not imply that increasing the Bond number, i.e. increasing the domain height, corresponds to a decrease of the physical onset (impingement) time. Indeed, to get the physical time t^*, we need to multiply t by H^*/W^* (see Sec. 7.3). In dimensional terms, the physical onset and impingement times scale with H^* as:

$$t_o^* \sim (H^*)^{0.24} \quad , \quad t_t^* \sim (H^*)^{0.72} \ . \tag{7.40}$$

The impingement time exhibits an excellent correspondence with the miscible case. Indeed, the scaling presented in Eq. (7.40) is closely related to the one obtained for miscible fluids ($t_t \sim (H^*)^{0.73}$). Thus we conclude that in the range of parameters investigated, the structures involved in the Rayleigh-Taylor flow exhibit the same asymptotic evolution, independently on the miscibility description considered.

We can estimate the asymptotic scaling of the physical mixing length h^* as a function of the physical time t^*. From Eq. (7.40), we expect that for long times $h^* \sim (t^*)^{1/0.72} \sim (t^*)^{1.39}$. On the other hand, the scaling law derived in the asymptotic regime of Fig. 7.7 reads:

$$h^* \sim (t^*)^{3/2} \ , \tag{7.41}$$

which is in fair agreement with the estimated value ($3/2 \approx 1.39$). In turn, during the initial stage the system evolution is faster ($h^* \sim (t^*)^5$).

7.A Appendix

Here the algebraic notions required to obtain the model (App. 7.A.1) and details on the specific solution of the Cahn-Hilliard equation (App. 7.A.2) will be provided.

7.A.1 Notions on tensors

In this appendix, we will derive some equations of the DBCH model and provide some definitions on tensors.

Diadic product The diadic product is represented with $\otimes$ and refers to a vectorial product between two elements, $\mathbf{A}, \mathbf{B} \in \mathbb{R}^n$, where the first is

multiplied by the second transposed, as follows:

$$\mathbf{A} \otimes \mathbf{B} = \mathbf{A}\mathbf{B}^T \Rightarrow (\mathbf{A} \otimes \mathbf{B})_{ij} = \mathbf{A}_i \mathbf{B}_j \ . \tag{7.42}$$

Divergence of a tensor If $\mathbf{C}$ is a tensor defined as $\mathbf{C} \in \mathbb{R}^{3\times3}$, its divergence is given by the vector:

$$\nabla \cdot \mathbf{C} = \begin{pmatrix} \frac{\partial C_{11}}{\partial x_1} + \frac{\partial C_{12}}{\partial x_2} + \frac{\partial C_{13}}{\partial x_3} \\ \frac{\partial C_{21}}{\partial x_1} + \frac{\partial C_{22}}{\partial x_2} + \frac{\partial C_{23}}{\partial x_3} \\ \frac{\partial C_{31}}{\partial x_1} + \frac{\partial C_{32}}{\partial x_2} + \frac{\partial C_{33}}{\partial x_3} \end{pmatrix} \ . \tag{7.43}$$

Korteweg stresses calculation The Darcy equation in coupled with the Cahn-Hilliard model through the Korteweg term, as reported in Eq. (7.2). The first component of this term is given by:

$$\begin{aligned} \nabla \cdot (\nabla\phi \otimes \nabla\phi)_1 &= \frac{\partial}{\partial x_1}\left(\frac{\partial \phi}{\partial x_1}\right)^2 + \frac{\partial}{\partial x_2}\left(\frac{\partial \phi}{\partial x_1}\frac{\partial \phi}{\partial x_2}\right) + \frac{\partial}{\partial x_3}\left(\frac{\partial \phi}{\partial x_1}\frac{\partial \phi}{\partial x_3}\right) \\ &= \frac{\partial \phi}{\partial x_1}\nabla^2\phi + \frac{1}{2}\frac{\partial}{\partial x_1}\left[\left(\frac{\partial \phi}{\partial x_1}\right)^2 + \left(\frac{\partial \phi}{\partial x_2}\right)^2 + \left(\frac{\partial \phi}{\partial x_3}\right)^2\right] \\ &= \frac{\partial \phi}{\partial x_1}\nabla^2\phi + \frac{1}{2}\frac{\partial}{\partial x_1}|\nabla\phi|^2 \end{aligned}$$

and considering all the components, the Korteweg stress can be rewritten in vectorial notation as:

$$\nabla \cdot (\nabla\phi \otimes \nabla\phi) = \nabla\phi\nabla^2\phi + \frac{1}{2}\nabla(|\nabla\phi|^2) \ . \tag{7.44}$$

7.A.2 Discretization of Cahn-Hilliard equation

The solution of the Cahn-Hilliard equation (Eq. (7.16)) requires robust numerical schemes due to the high order operators that it involves; expanding Eq. (7.16), a 4^{th}-order operator is highlighted:

$$\frac{\partial \phi}{\partial t} = -\mathbf{u} \cdot \nabla\phi + \frac{1}{Pe}\left(\nabla^2\phi^3 - \nabla^2\phi - Ch\,\nabla^4\phi\right) \ . \tag{7.45}$$

To reduce the stability requirements and adopt the same pseudo-spectral solution involved for the momentum equations, Eq. (7.45) is rewritten in the following way:

$$\frac{\partial \phi}{\partial t} = S_\phi + s\frac{Ch}{Pe}\nabla^2\phi - \frac{Ch}{Pe}\nabla^4\phi \ . \tag{7.46}$$

The operator splitting $\nabla^2\phi = \nabla^2\phi(s\,Ch + 1) - s\,Ch\,\nabla^2\phi$ is similar to that adopted by Yue et al. (2004) and is obtained through a positive coefficient

s that is chosen considering the temporal discretization. The convective term, the non-linear term and the terms rising from the operator splitting are collected in the S_ϕ term:

$$S_\phi = -\mathbf{u}\cdot\nabla\phi + \frac{1}{Pe}\nabla^2\phi^3 - \frac{(s\,Ch+1)}{Pe}\nabla^2\phi\ . \tag{7.47}$$

Eq. (7.46) is discretized in space adopting the Fourier-Chebyshev spectral representation (discussed in detail in Appendix A, and results:

$$\begin{aligned}\frac{\partial\widehat{\phi}}{\partial t} &= \widehat{S}_\phi + s\frac{Ch}{Pe}\left(\frac{\partial^2}{\partial z^2}-k_{xy}^2\right)\widehat{\phi} \\ &- \frac{Ch}{Pe}\left(\frac{\partial^2}{\partial z^2}-k_{xy}^2\right)\left(\frac{\partial^2}{\partial z^2}-k_{xy}^2\right)\widehat{\phi}\ ,\end{aligned} \tag{7.48}$$

where the hat represents the Fourier coefficient and $k_{xy} = k_x^2 + k_y^2$, with k_x and k_y modal coordinates. The Cahn-Hilliard equation solutions are characterized by the presence of high frequency harmonics, that need to be damped in order to keep the solution bounded. The adoption of weakly damping schemes, such as the Crank-Nicholson adopted for the velocity field equations leads to aliased solutions (Ascher et al., 1995). For this reason, following Yue et al. (2004), a 1^{st}-order Backward Difference Formula (BDF) is adopted. In particular the non linear convective S_ϕ term is discretized adopting a 2^{nd} order Adams-Bashforth:

$$\begin{aligned}\frac{\widehat{\phi}^{n+1}-\widehat{\phi}^{n}}{\Delta t} &= \frac{3}{2}\widehat{S}_\phi^n - \frac{1}{2}\widehat{S}_\phi^{n-1} + s\frac{Ch}{Pe}\left(\frac{\partial^2}{\partial z^2}-k_{xy}^2\right)\widehat{\phi}^{n+1} \\ &- \frac{Ch}{Pe}\left(\frac{\partial^2}{\partial z^2}-k_{xy}^2\right)\left(\frac{\partial^2}{\partial z^2}-k_{xy}^2\right)\widehat{\phi}^{n+1}\ ,\end{aligned} \tag{7.49}$$

being $n-1$, n and $n+1$ the time instants. Introducing the coefficient $\gamma_\phi = (\Delta t\ Ch)/\ Pe$, Eq. (7.49) yields:

$$\left[\frac{1}{\gamma_\phi} - s\left(\frac{\partial^2}{\partial z^2}-k_{xy}^2\right) + \left(\frac{\partial^2}{\partial z^2}-k_{xy}^2\right)^2\right]\widehat{\phi}^{n+1} = \frac{\widehat{H}_\phi}{\gamma_\phi}\ , \tag{7.50}$$

where the historical term $\widehat{H}_\phi$ has been used:

$$\frac{\widehat{H}_\phi}{\gamma_\phi} = \frac{1}{\gamma_\phi}\left(\widehat{\phi}^n + \frac{3\Delta t}{2}\widehat{S}_\phi^n - \frac{\Delta t}{2}\widehat{S}_\phi^{n-1}\right)\ . \tag{7.51}$$

Defining the auxiliary variable $\theta_\phi = \lambda_\phi\phi + \nabla^2\phi$, the 4^{th}-order Eq. (7.50) can be split in two 2^{nd} order equations:

$$\left(\frac{\partial^2}{\partial z^2} - k_{xy}^2 + \lambda_\phi - \frac{s}{Ch}\right)\widehat{\theta}_\phi = \frac{\widehat{H}_\phi}{\gamma_\phi}\ , \tag{7.52}$$

$$\left(\frac{\partial^2}{\partial z^2} - k_{xy}^2 - \lambda_\phi\right)\widehat{\phi}^{n+1} = \widehat{\theta}_\phi \ . \tag{7.53}$$

In order to recovery Eq. (7.48), the coefficients λ_ϕ yields to the following:

$$\lambda_\phi = \frac{s}{2}\left(-1 - \sqrt{1 - \frac{4}{\gamma_\phi s^2}}\right) \ , \tag{7.54}$$

where $s \geq \sqrt{4\,Pe\,/\Delta t\,Ch}$. Eq. (7.53) is solved imposing the following boundary conditions that emerge from a normal contact angle for the interface at the horizontal boundaries:

$$\frac{\partial\widehat{\phi}^{n+1}}{\partial z}(\pm 1) = 0 \ , \qquad \frac{\partial^3\widehat{\phi}^{n+1}}{\partial z^3}(\pm 1) = 0 \ . \tag{7.55}$$

Eq. (7.52) and Eq. (7.53) are solved through a Chebyshev-Tau algorithm and the resulting tridiagonal linear system is solved by Gauss elimination.

Conclusions and Appendices

8

Conclusions

In this thesis solute convection in homogeneous and two-dimensional porous media has been studied. When convection occurs in porous media flows, it is characterized by a complex non-linear evolution, which makes predictions on structures dynamics hard to obtain. Moreover, real geological sequestration sites are considered as anisotropic, inhomogeneous and three-dimensional porous formations.

In Part I of this thesis, we focused on the effect of anisotropic permeability on porous media convection. This represents the realistic case of sedimentary rocks, which are characterized by a vertical-to-horizontal permeability ratio γ, being $0 < \gamma \leq 1$. With the aid of Direct Numerical Simulations, we analysed the effect of anisotropy on the dissolution rate in a Rayleigh-Bénard-like configuration.

In Chap. 3, we investigated the classical Rayleigh-Bénard problem (also called two-sided configuration), in which solute transport occurs between a heavier layer (upper boundary) and a lighter layer (lower boundary). We characterized the flow dynamics in a wide range of Rayleigh numbers. Supported by the analysis of the flow topology, we demonstrated that in the range of γ considered the anisotropy has a positive effect, i.e. the dissolution rate increases up to 40% with $\gamma = 1/4$. We shown that the Rayleigh-Bénard configuration is computationally expensive, and no possibility to reduced this system to a lower-dimensional problem is feasible at high regimes. Furthermore, using these results we developed a theoretical model, in order to predict the time-dependent dissolution rate, which occurs in a one-sided domain during the so called shutdown regime, i.e. when convection is inhibited.

In the classical two-sided configuration (Rayleigh-Bénard), convective transport occurs away from both upper and lower boundaries. Solutal convection inside geological reservoirs tends instead to be driven by a source of buoyancy occurring on one boundary only (the top wall), a situation that induces a complex dynamics characterized by a sequence of different regimes changing in time (time dependent dynamics). A domain represented by this configuration is indicated as one-sided, and the transient dynamics occur-

ring in the aforementioned set up have been considered in Chap. 4. The role of anisotropic permeability throughout the dissolution process was singled out: the entire dissolution process was investigated, from the initial diffusion regime up to the final convection-dominated and shutdown stages. The purpose of this chapter was to provide a unified picture of the solute dynamics in anisotropic porous media at high Rayleigh numbers. In particular, we observed that anisotropy has a positive effects also in this configuration. Indeed, the onset occurs earlier compared to the isotropic case, and the dissolution rate during the constant flux regime takes advantage from the flow modifications induced by the porous medium anisotropy. A simple theoretical model, based on numerical results and on physical observations, has been developed and the dissolution rate has been parametrized in time. Moreover, these results have been included in a large-scale model, in which the evolution of buoyant injected CO_2 is influenced by the heavy satured-brine current. We show that also in this case, the beneficial effect of anisotropy persists in both large and small-scale injection projects.

Carbon dioxide is only partially miscible in brine, up to 3%, and the classical advection-diffusion approach may be not precise. Moreover, all the fluxes exchanged between the two phases pass through the fluids interface, and an accurate description of the phenomena occurring in the nearby of the interface itself is required with the aim of modelling further physical features. Following this motivation, the effect of fluid miscibility has been investigated in Part II.

We considered a fixed amount of satured brine mixture overlying a pure brine layer. When both top and bottom boundaries are assumed impermeable to fluid and solute fluxes, this conceptual setup is defined as Rayleigh-Taylor configuration. If we consider fully miscible fluids, time-dependent finger-like structures arise. The behaviour of these structures is, in a certain way, similar to that observe in the Rayleigh-Bénard problem. In Chap. 6, we highlighted some of the similarities that these two systems share. Using the same advection-diffusion model adopted in Part I but on a Rayleigh-Taylor configuration, we analysed the evolution of two miscible fluids in an isotropic porous layer. In particular, we have shown that provided an appropriate scaling, the dimensionless dissolution rate computed in correspondence of different domain sizes reduces to the same scaling law observed in the isotropic Rayleigh-Bénard problem. Moreover, we computed some relevant quantities influenced by the presence of impermeable boundaries. We observed, for instance, that the asymptotic evolution of the mixing length in time is more than linear.

However, as mentioned above, CO_2 is not fully miscible, and an alternative approach could describe in a more consistent way the transfer mechanisms occurring through the interface. In Chap. 7, we developed a phase-field model for isotropic porous media, in which the miscibility of the fluids is admitted along the interface only, whereas in the core of the phases fluids are considered as pure. This model, based on the Cahn-Hilliard equa-

tion and thus thermodynamically consistent, depends on three parameters. First, we investigated the significance of these parameters and their influence on the flow features. Then, we focused on the effect of one of these parameters, the Bond number, which represents a measure of the relative importance of buoyancy forces compared to surface tension. Indeed, we observed that the Bond number is the only parameters characterized by a purely physical interpretation, in spite of the others (Cahn and Peclet numbers) which are more related to the numerical procedure adopted to solve the equations. Finally, we analysed the same observables (mixing length and plume tip velocity) considered in the miscible case, and we concluded that in both these systems the macroscopic mixing properties evolve in time according to the same scaling.

8.1 Future developments

In this work, we have provided a description of the flow features and of the dissolution phenomena in porous media convection. Real geological formations are characterized by heterogeneous, three-dimensional and anisotropic porous media.

In this work, we filled the gap existing in literature between isotropic and anisotropic convection at high Rayleigh numbers and two dimensional porous medium. Indeed, we have furnished a description of the modifications of flow topology and the beneficial effects of anisotropy on the dissolution rate. However, porous medium are naturally three-dimensional, and a systematic analysis of the influence of anisotropic permeability of the dissolution rate in three-dimensional domains should be considered. Hewitt et al. (2014) and Pau et al. (2010) observed that in isotropic convection, the dissolution rate increases up to 40% with respect to the two-dimensional configuration, and a similar trend is expected for the anisotropic case.

The effects of heterogeneities on the CO_2 dissolution rate remains a debated issue, and only few works are available. However, Green and Ennis-King (2014) have shown that the constant flux regime is not significantly influenced by an heterogeneous permeability fields, and the influence of anisotropy is dominant.

We improved the fluid interface description with a phase-field model, which is supposed to mimic the miscibility of CO_2-satured and pure brine. These results refer to two-dimensional, homogeneous and isotropic porous medium, which consists of a simplified representation of a real geological formation. The analyses proposed represent a first, fundamental step in the modelling of immiscible fluids in porous media. However, anisotropy, heterogeneities and three-dimensionality should be simultaneously considered in order to analyse the interaction among these different features.

Finally, an intriguing possible development of the present work is represented by the analysis of the CO_2-dissolution enhancement due to chemical

reactions (Loodts et al., 2014) and its interactions with the above mentioned porous medium properties.

A

Appendix: Numerical details

In this appendix numerical details on the procedure and on the parallelization strategy adopted are reported. In spite of the two-dimensional simulations performed in the present work, the code has been developed to resolve three-dimensional simulations. The equations presented throughout this thesis have been solved adopting a pseudo-spectral spatial discretization: solutions are approximated by Discrete Fourier Transforms (DFT) along the periodic directions of the channel geometry (x, y), whereas Chebyshev polynomials are adopted along the wall-normal direction (z).

A.1 Spectral approximation

In order to avoid convolutions in the Fourier-Chebyshev space, the multiplication of spectral variables (i.e. convective terms) is obtained by transforming back the variables to the physical space, taking the multiplications and the re-transforming to the Fourier-Chebyshev space. For this reason, these class of algorithms is also known as "pseudo-spectral algorithms". A complete review of these methods can be found in Boyd (2001).

A signal $g(x, y, z)$ defined in the physical space and projected onto the Fourier space along the periodic directions x and y, can be represented by the following sum of harmonics:

$$g(x,y,z) = \sum_{n_x=N_{x_1}}^{N_x/2} \sum_{n_y=N_{y_1}}^{N_y/2} \hat{g}(k_x,k_y,z) e^{j(k_x x + k_y y)} \ , \tag{A.1}$$

where $j = \sqrt{-1}$ is the imaginary unit of the complex representation, $\hat{g}$ is the Fourier coefficient of the signal in the modal coordinates (k_x, k_y) and $N_{x_1} = -N_x/2 + 1$, $N_{y_1} = -N_y/2 + 1$, being N_x and N_y the Fourier modes number in x and y directions respectively. The two periodic directions are treated with a Fast Fourier Transform (FFT) algorithm by imposing periodicity lengths of L_x and L_y and projecting the velocity vector onto N_x and N_y Fourier modes. Through the Fourier transform, unknown variables

are mapped on a uniform grid in the physical space, whose nodes spacing is:

$$\Delta x = \frac{L_x}{N_x - 1} \ , \qquad \Delta_y = \frac{L_y}{N_y - 1} \ . \tag{A.2}$$

The signal is decomposed in a sum of periodic functions characterized by wave number and amplitude; the former represents the frequency of the corresponding harmonic, whereas the latter is the magnitude of the harmonic. Each mode n_x or n_y is characterized by the following wave numbers:

$$k_x = \frac{2\pi n_x}{L_x} \ , \qquad k_y = \frac{2\pi n_y}{L_y} \ . \tag{A.3}$$

Since the Fourier basis is orthogonal, the Fourier transform $\hat{g}$ can be obtained as follows:

$$\hat{g}(k_x, k_y, z) = \frac{1}{N_x N_y} \sum_{n_x = N_{x_1}}^{N_x/2} \sum_{n_y = N_{y_1}}^{N_y/2} g(x, y, z) e^{-j(k_x x + k_y y)} \ . \tag{A.4}$$

At this point, the dependence on the physical coordinate z is still present. Along the wall normal direction z, the transformed signal $\hat{g}(k_x, k_y, z)$ is approximated through the sum of Chebyshev polynomials $T_n(z)$:

$$\hat{g}(k_x, k_y, z) = \sum_{n_z = 0}^{N_z'} h(k_x, k_y, n_z) T_n(z) \ , \tag{A.5}$$

where the prime indicates the first term halving. The Chebyshev polynomial of order n_z in z is defined as follows:

$$T_{n_z}(z) = \cos\left[n_z \arccos(z)\right] \ , \tag{A.6}$$

where n_z is one of the N_z Chebyshev modes and $-1 \leq z \leq 1$. Orthogonality property holds also for the Chebyshev polynomials and the inverse transform is:

$$\hat{h}(k_x, k_y, n_z) = \frac{2}{N_z} \sum_{n_z = 0}^{N_z'} \hat{g}(k_x, k_y, z) T_n(z) \ . \tag{A.7}$$

Variables represented in the Chebyshev space are mapped in the physical space according to:

$$z = \cos\left(\frac{n_z \pi}{N_z}\right) \ . \tag{A.8}$$

With adoption of Chebychev polynomials for the approximation of the solution along the wall-normal direction, the spatial discretization is characterized by a high resolutions close the walls (see Fig. A.1a), where large velocity (or solute) gradients need to be resolved.

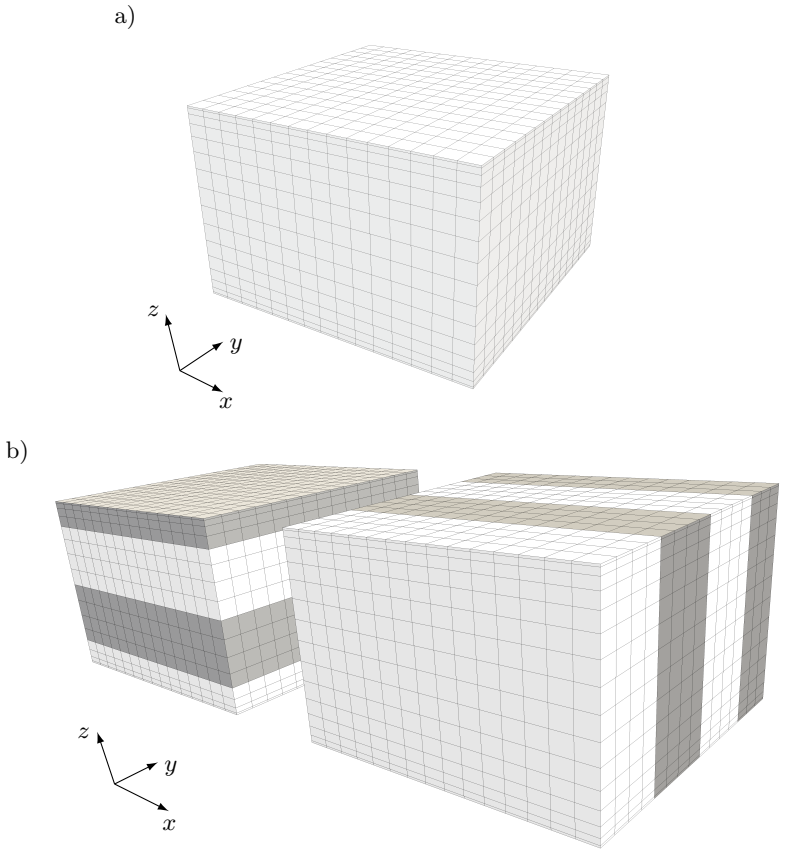

FIGURE A.1 – Schematic representation of the domain in an exemplar three-dimensional configuration. Panel a) The grid results uniform in the periodic directions (x, y), whereas it is non-uniform along the wall-normal direction (z), due to the Chebyshev discretization adopted. Panel b) One-dimensional domain decomposition used to distribute the computational load among the task. First FFT is performed (horizontal slices), then Chebyshev transform is calculated (vertical slabs). In this example, the computation is shared among four processes.

Finally, performing the transformations of Eqs. (A.1) and (A.5), the spectral representation of the time-dependent signal $g(x, y, z, t)$ defined in the three-dimensional space reads:

$$g(x,y,z,t) = \sum_{n_x=N_{x_1}}^{N_x/2} \sum_{n_y=N_{y_1}}^{N_y/2} \sum_{n_z=0}^{N_z'} \hat{h}(k_x,k_y,n_z,t) T_{n,z}(z) e^{j(k_x x + k_y y)} \ . \quad \text{(A.9)}$$

Due to the presence of products taken into the physical space (non-linear convective term), the computational algorithm requires the introduction

of dealiasing procedures also in the Chebyshev transforms; following Boyd (2001), the "2/3 rule" is applied, keeping only the first two thirds of the modes after the application of the pseudo-spectral multiplications.

A.2 Parallelization

In order to reduce the time required for the simulations, the code developed has been parallelized with a Message Passing Interface (MPI) paradigm and up to 512 CPUs have been used.

A schematic representation of the two-dimensional domain decomposition adopted is reported in Fig. A.1b). The domain is initially divided in horizontal slices along the wall-normal direction (z). At this moment, Fast Fourier Transform is performed in periodic directions (x, y). Finally, when the Chebyshev transform is required, the field is assembled and redistributed to the processes in vertical slabs along the y direction.

The simulations analysed throughout this thesis have been performed on several clusters (see also Sec. B.3) and a large amount of data ($\approx$ 15 TB) has been produced.

B

Publications, courses and projects

B.1 Referred Journals

J1 **De Paoli, M.**, Zonta, F. and Soldati, A. (2016). Influence of anisotropic permeability on convection in porous media: Implications for geological CO2 sequestration, *Physics of Fluids (1994-present)*, Volume 28 (Issue 5) (De Paoli et al., 2016).

J2 **De Paoli, M.**, Zonta, F. and Soldati, A. (2017). Dissolution in anisotropic porous media: Modelling convection regimes from onset to shutdown, *Physics of Fluids (1994-present)*, Volume 29 (Issue 2) (De Paoli et al., 2017).

J3 **De Paoli, M.**, Zonta, F. and Soldati, A. (2017). Rayleigh-Taylor instability in porous media: Miscible fluids, *Physical Review Fluids* (to be submitted).

J4 **De Paoli, M.**, Zonta, F. and Soldati, A. (2017). Rayleigh-Taylor instability in porous media: Immiscible fluids (in preparation).

B.2 Referred Conferences

C9 **De Paoli, M.**[†], Zonta, F. and Soldati A., (2016) Solute dissolution in anisotropic porous media: Modelling convection regimes from onset to shutdown. *APS-DFD Annual Meeting*, Portland (OR, USA), November 20-22, 2016.

C8 **De Paoli, M.**[‡], Zonta, F. and Soldati A., (2016) Lightning storm: Flow topology in porous media. Gallery of Fluid motion at *APS-DFD Annual Meeting*, Portland (OR, USA), November 20-22, 2016.

C7 **De Paoli, M.**, Zonta, F. and Soldati A.†, (2016) Influence of anisotropic permeability on convection in porous media: Implications for geological CO2 sequestration. *European Fluid Mechanics Conference 2016*, Seville (Spain), September 12-16, 2016.

C6 **De Paoli, M.**,† Zonta, F. and Soldati A., (2016) Influence of anisotropic permeability on convection in porous media: Implications for geological CO2 sequestration. *International Conference on Multiphase Flow*, Florence (Italy), May 22-27, 2016.

C5 **De Paoli, M.**,‡ Zonta, F. and Soldati A., (2016) Reduction of greenhouse effect: Direct numerical simulation of geological CO2 sequestration. *PRACE Days 2016*, Prague (Czech Republic), May 10-12, 2016.

C4 **De Paoli, M.**,† Zonta, F. and Soldati A., (2015) Numerical and analytical study of carbon dioxide sequestration in anisotropic porous medium. *ERCOFTAC ADA Pilot Centre Meeting*, Ljubljana (Slovenia), November 13, 2016.

C3 **De Paoli, M.**,† Zonta, F. and Soldati A., (2015) Global warming: To tackle the problem at its roots. *International HPC Summer School 2015*, Toronto (ON, Canada), June 21, 2015.

C2 **De Paoli, M.**,† Zonta, F. and Soldati A., (2015) Numerical and analytical study of carbon dioxide sequestration in anisotropic porous medium. *ERCOFTAC Dottorandi Italian Pilot Centre Meeting*, Rome (Italy), December 9, 2014.

C1 **De Paoli, M.**,† Zonta, F. and Soldati A., (2014) Fluid mechanics of supercritical CO2 into geological reservoir. *ERCOFTAC ADA Pilot Centre Meeting*, Maribor (Slovenia), November 7, 2014.

† Presentation speaker.
‡ Poster speaker.

B.3 HPC Projects

P3 **Simulation of Geological Carbon Dioxide Sequestration**, Vienna Scientific Cluster - Project ID: 70894, VSC3 (Tier 0), Vienna (Austria), 2016.

P2 **Simulation of geological CARbon DIOxide Sequestration - CARDIOS**, Italian Supercomputing Resource Allocation - Project ID: ISCRA B HP10BT2CCX, CINECA Supercomputing Centre, Marconi (Tier 0), Bologna (Italy), 2015.

P3 **Numerical simulations of GEological CO2 Sequestration - GECOS**, Italian Supercomputing Resource Allocation - Project ID: ISCRA C HP10C7M9MV, CINECA Supercomputing Centre, Fermi (Tier 0), Bologna (Italy), 2016.

B.4 Advanced Courses

A9 **Argonne Training Program on Extreme Scale Computing 2016**, Argnonne National Lab., Chicago, Illinois (USA), August, 2016. Coordinated by: Dr. M. Garcia Martinez (Argonne National Lab., USA).

A8 **Simulation of dispersed flows at the particle level**, University of Udine, Udine (Italy), December, 2015. Coordinated by: Prof. J. Derksen (University of Aberdeen, United Kingdom).

A7 **Mixing and Dispersion in Flows Dominated by Rotation and Buoyancy**, International Centre for Mechanical Sciences (CISM), Udine (Italy), July, 2015. Coordinated by: Prof. H. Clercx (Eindhoven University of Technology, The Netherlands) and Prof. G. J. van Heijst (Eindhoven University of Technology, The Netherlands).

A6 **International HPC Summer School 2015 - Toronto**, PRACE, XSEDE, Compute Canada, RIKEN, Toronto (ON, Canada), June, 2015. Coordinated by: Prof. H. Lederer (PRACE), S. Lathrop (XSEDE), J. Ferland (Compute Canada), M. Sato (RIKEN).

A5 **Dynamic of Bubbly flows**, International Centre for Mechanical Sciences (CISM), Udine (Italy), June, 2015. Coordinated by: Prof. F. Risso (CNRS and Université de Toulouse, France) and Prof. C. Sun (University of Twente, The Netherlands).

A4 **Advanced CFD techniques for turbulent flows: theory and applications**, Universiyt of Udine, Udine (Italy), May, 2015. Coordinated by: Prof. U. Piomelli (Queen's University, Canada).

A3 **Summer School on Parallel Computing**, SuperComputing Applications and Innovation (SCAI) CINECA, Rome (Italy), July, 2014. Coordinated by: G. Erbacci (CINECA, Bologna).

A2 **Collective particle dynamics: from viscous to turbulent flows**, International Centre for Mechanical Sciences (CISM), Udine (Italy), May, 2014. Coordinated by: Prof. C. Marchioli (University of Udine) and Prof. G. Bouchet (Aix-Marseille University and CNRS, France).

A1 **Fractal flow design: how to design bespoke turbulence and why**, International Centre for Mechanical Sciences (CISM), Udine

(Italy), September, 2013. Coordinated by: Prof. C. Vassilicos (Imperial College of London, United Kingdom).

Bibliography

Ascher, U. M., Ruuth, S. J., and Wetton, B. T. R. (1995). Implicit-explicit methods for time-dependent partial differential equations. *SIAM Journal on Numerical Analysis*, 32(3):797–823.

Backhaus, S., Turitsyn, K., and Ecke, R. (2011). Convective instability and mass transport of diffusion layers in a Hele-Shaw geometry. *Physical Review Letters*, 106(10):104501.

Bear, J. (2013). *Dynamics of fluids in porous media*. Courier Corporation.

Bickle, M., Chadwick, A., Huppert, H. E., Hallworth, M., and Lyle, S. (2007). Modelling carbon dioxide accumulation at Sleipner: Implications for underground carbon storage. *Earth and Planetary Science Letters*, 255(1):164–176.

Bielinski, A. (2007). *Numerical simulation of CO2 sequestration in geological formations*. PhD thesis, Institute fur Wasserbau der Universitat Stuttgart.

Boffetta, G. and Mazzino, A. (2017). Incompressible Rayleigh-Taylor turbulence. *Annual Review of Fluid Mechanics*, 49(1).

Bolster, D. (2014). The fluid mechanics of dissolution trapping in geologic storage of CO2. *Journal of Fluid Mechanics*, 740:1–4.

Boyd, J. P. (2001). *Chebyshev and Fourier spectral methods*. Courier Dover Publications.

Cabot, W. H. and Cook, A. W. (2006). Reynolds number effects on Rayleigh–Taylor instability with possible implications for type Ia supernovae. *Nature Physics*, 2(8):562–568.

Cahn, J. W. and Hilliard, J. E. (1958). Free energy of a nonuniform system. I. Interfacial free energy. *The Journal of Chemical Physics*, 28(2):258–267.

Celani, A., Mazzino, A., Muratore-Ginanneschi, P., and Vozella, L. (2009). Phase-field model for the Rayleigh–Taylor instability of immiscible fluids. *Journal of Fluid Mechanics*, 622:115–134.

Chen, C.-Y., Wang, L., and Meiburg, E. (2001). Miscible droplets in a porous medium and the effects of Korteweg stresses. *Physics of Fluids (1994-present)*, 13(9):2447–2456.

Chen, C.-Y. and Yan, P.-Y. (2015). A diffuse interface approach to injection-driven flow of different miscibility in heterogeneous porous media. *Physics of Fluids (1994-present)*, 27(8):083101.

Cheng, P., Bestehorn, M., and Firoozabadi, A. (2012). Effect of permeability anisotropy on buoyancy-driven flow for CO_2 sequestration in saline aquifers. *Water Resources Research*, 48(9).

Ching, E. S., Guo, H., Shang, X.-D., Tong, P., and Xia, K.-Q. (2004). Extraction of plumes in turbulent thermal convection. *Physical Review Letters*, 93(12):124501.

Chini, G. P., Dianati, N., Zhang, Z., and Doering, C. R. (2011). Low-dimensional models from upper bound theory. *Physica D: Nonlinear Phenomena*, 240(2):241–248.

Chui, J. Y., de Anna, P., and Juanes, R. (2015). Interface evolution during radial miscible viscous fingering. *Physical Review E*, 92(4):041003.

Cook, A. W. and Dimotakis, P. E. (2001). Transition stages of Rayleigh–Taylor instability between miscible fluids. *Journal of Fluid Mechanics*, 443:69–99.

Cueto-Felgueroso, L. and Juanes, R. (2014). A phase-field model of two-phase Hele-Shaw flow. *Journal of Fluid Mechanics*, 758:522–552.

De Paoli, M., Zonta, F., and Soldati, A. (2016). Influence of anisotropic permeability on convection in porous media: Implications for geological CO2 sequestration. *Physics of Fluids (1994-present)*, 28(5):056601.

De Paoli, M., Zonta, F., and Soldati, A. (2017). Dissolution in anisotropic porous media: Modelling convection regimes from onset to shutdown. *Physics of Fluids (1994-present)*, 29(2).

De Wit, A. (2001). Fingering of chemical fronts in porous media. *Physical Review Letters*, 87(5):054502.

De Wit, A. (2004). Miscible density fingering of chemical fronts in porous media: Nonlinear simulations. *Physics of Fluids (1994-present)*, 16(1):163–175.

Ennis-King, J., Preston, I., and Paterson, L. (2005). Onset of convection in anisotropic porous media subject to a rapid change in boundary conditions. *Physics of Fluids (1994-present)*, 17(8):084107.

Fermi, E. and Von Neumann, J. (1953). *Taylor instability of incompressible liquids*, volume 2979. United States Atomic Energy Commission, Technical Information Service.

Fernandez, J., Kurowski, P., Petitjeans, P., and Meiburg, E. (2002). Density-driven unstable flows of miscible fluids in a Hele-Shaw cell. *Journal of Fluid Mechanics*, 451:239–260.

Friedmann, S. J. (2007). Geological carbon dioxide sequestration. *Elements*, 3(3):179–184.

Gasda, S. E., Nordbotten, J. M., and Celia, M. A. (2011). Vertically averaged approaches for CO2 migration with solubility trapping. *Water Resources Research*, 47(5).

Glasner, K. (2002). A diffuse interface approach to Hele–Shaw flow. *Nonlinearity*, 16(1):49.

Golub, G. H. and Van Loan, C. F. (2012). *Matrix computations*, volume 3. JHU Press.

Graham, M. D. and Steen, P. H. (1994). Plume formation and resonant bifurcations in porous-media convection. *Journal of Fluid Mechanics*, 272:67–90.

Green, C. P. and Ennis-King, J. (2014). Steady dissolution rate due to convective mixing in anisotropic porous media. *Advances in Water Resources*, 73:65–73.

Gunton, J., San Miguel, M., Sahni, P. S., Domb, C., and Lebowitz, J. (1983). *Phase transitions and critical phenomena*. Academic, New York.

Gurtin, M. E., Polignone, D., and Viñals, J. (1996). Two-phase binary fluids and immiscible fluids described by an order parameter. *Mathematical Models and Methods in Applied Sciences*, 6(06):815–831.

Hesse, M. A. (2008). *Mathematical modeling and multiscale simulation for CO2 storage in saline aquifers*. PhD thesis, Department of Energy Resources Engineering, Stanford University.

Hewitt, D. R., Neufeld, J. A., and Lister, J. R. (2012). Ultimate regime of high Rayleigh number convection in a porous medium. *Physical Review Letters*, 108(22):224503.

Hewitt, D. R., Neufeld, J. A., and Lister, J. R. (2013a). Convective shutdown in a porous medium at high Rayleigh number. *Journal of Fluid Mechanics*, 719:551–586.

Hewitt, D. R., Neufeld, J. A., and Lister, J. R. (2013b). Stability of columnar convection in a porous medium. *Journal of Fluid Mechanics*, 737:205–231.

Hewitt, D. R., Neufeld, J. A., and Lister, J. R. (2014). High Rayleigh number convection in a three-dimensional porous medium. *Journal of Fluid Mechanics*, 748:879–895.

Hidalgo, J. J., Fe, J., Cueto-Felgueroso, L., and Juanes, R. (2012). Scaling of convective mixing in porous media. *Physical Review Letters*, 109(26):264503.

Hirt, C. W. and Nichols, B. D. (1981). Volume of fluid (VOF) method for the dynamics of free boundaries. *Journal of Computational Physics*, 39(1):201–225.

Homsy, G. M. (1987). Viscous fingering in porous media. *Annual Review of Fluid Mechanics*, 19(1):271–311.

Horton, C. and Rogers Jr, F. (1945). Convection currents in a porous medium. *Journal of Applied Physics*, 16(6):367–370.

Huppert, H. E. and Neufeld, J. A. (2014). The fluid mechanics of carbon dioxide sequestration. *Annual Review of Fluid Mechanics*, 46:255–272.

Kalisch, H., Mitrovic, D., and Nordbotten, J. (2016). Rayleigh–Taylor instability of immiscible fluids in porous media. *Continuum Mechanics and Thermodynamics*, 28(3):721–731.

Lamorgese, A. and Mauri, R. (2015). Buoyancy-driven detachment of a wall-bound pendant drop: Interface shape at pinchoff and nonequilibrium surface tension. *Physical Review E*, 92(3):032401.

Lamorgese, A. G., Molin, D., and Mauri, R. (2011). Phase field approach to multiphase flow modeling. *Milan Journal of Mathematics*, 79(2):597–642.

Landman, A. J. and Schotting, R. J. (2007). Heat and brine transport in porous media: The Oberbeck-Boussinesq approximation revisited. *Transport in Porous Media*, 70(3):355–373.

Lapwood, E. (1948). Convection of a fluid in a porous medium. *Proceedings of the Cambridge*, 44:508–521.

Lassila, T., Manzoni, A., Quarteroni, A., and Rozza, G. (2014). Model order reduction in fluid dynamics: Challenges and perspectives. In *Reduced Order Methods for modeling and computational reduction*, pages 235–273. Springer.

Lee, H.-G., Lowengrub, J., and Goodman, J. (2002). Modeling pinchoff and reconnection in a Hele-Shaw cell. I. The models and their calibration. *Physics of Fluids (1994-present)*, 14(2):492–513.

Loodts, V., Thomas, C., Rongy, L., and De Wit, A. (2014). Control of convective dissolution by chemical reactions: General classification and application to CO2 dissolution in reactive aqueous solutions. *Physical Review Letters*, 113(11):114501.

MacMinn, C., Szulczewski, M., and Juanes, R. (2011). CO2 migration in saline aquifers. Part 2. Capillary and solubility trapping. *Journal of Fluid Mechanics*, 688:321–351.

MacMinn, C. W., Neufeld, J. A., Hesse, M. A., and Huppert, H. E. (2012). Spreading and convective dissolution of carbon dioxide in vertically confined, horizontal aquifers. *Water Resources Research*, 48(11).

Magaletti, F., Picano, F., Chinappi, M., Marino, L., and Casciola, C. M. (2013). The sharp-interface limit of the Cahn–Hilliard/Navier–Stokes model for binary fluids. *Journal of Fluid Mechanics*, 714:95–126.

Mauri, R., Shinnar, R., and Triantafyllou, G. (1996). Spinodal decomposition in binary mixtures. *Physical Review E*, 53(3):2613.

Metz, B., Davidson, O., de Coninck, H., Loos, M., Meyer, L., et al. (2005). Carbon dioxide capture and storage: Special report of the IPCC.

Neufeld, J. A., Hesse, M. A., Riaz, A., Hallworth, M. A., Tchelepi, H. A., and Huppert, H. E. (2010). Convective dissolution of carbon dioxide in saline aquifers. *Geophysical Research Letters*, 37(22).

Otero, J., Dontcheva, L. A., Johnston, H., Worthing, R. A., Kurganov, A., Petrova, G., and Doering, C. R. (2004). High-Rayleigh number convection in a fluid-saturated porous layer. *Journal of Fluid Mechanics*, 500:263–281.

Paparella, F. and von Hardenberg, J. (2012). Clustering of salt fingers in double-diffusive convection leads to staircaselike stratification. *Physical Review Letters*, 109(1):014502.

Pau, G. S., Bell, J. B., Pruess, K., Almgren, A. S., Lijewski, M. J., and Zhang, K. (2010). High-resolution simulation and characterization of density-driven flow in CO2 storage in saline aquifers. *Advances in Water Resources*, 33(4):443–455.

Puragliesi, R. and Leriche, E. (2012). Proper orthogonal decomposition of a fully confined cubical differentially heated cavity flow at Rayleigh number Ra= 10^9. *Computers & Fluids*, 61:14–20.

Riaz, A., Hesse, M., Tchelepi, H., and Orr, F. (2006). Onset of convection in a gravitationally unstable diffusive boundary layer in porous media. *Journal of Fluid Mechanics*, 548:87–111.

Saffman, P. G. and Taylor, G. (1958). The penetration of a fluid into a porous medium or Hele-Shaw cell containing a more viscous liquid. In *Proceedings of the Royal Society of London A: Mathematical, Physical and Engineering Sciences*, volume 245, pages 312–329. The Royal Society.

Schmuck, M., Pavliotis, G. A., and Kalliadasis, S. (2014). Effective macroscopic interfacial transport equations in strongly heterogeneous environments for general homogeneous free energies. *Applied Mathematics Letters*, 35:12–17.

Schmuck, M., Pradas, M., Pavliotis, G. A., and Kalliadasis, S. (2012). Upscaled phase-field models for interfacial dynamics in strongly heterogeneous domains. In *Proc. R. Soc. A*, volume 478, pages 3705–3724. The Royal Society.

Schmuck, M., Pradas, M., Pavliotis, G. A., and Kalliadasis, S. (2013). Derivation of effective macroscopic Stokes–Cahn–Hilliard equations for periodic immiscible flows in porous media. *Nonlinearity*, 26(12):3259.

Schrag, D. P. (2007). Preparing to capture carbon. *Science*, 315(5813):812–813.

Schumacher, J. (2009). Lagrangian studies in convective turbulence. *Physical Review E*, 79(5):056301.

Siade, A. J., Putti, M., and Yeh, W. W.-G. (2010). Snapshot selection for groundwater model reduction using proper orthogonal decomposition. *Water Resources Research*, 46(8).

Slim, A. C. (2014). Solutal-convection regimes in a two-dimensional porous medium. *Journal of Fluid Mechanics*, 741:461–491.

Slim, A. C., Bandi, M., Miller, J. C., and Mahadevan, L. (2013). Dissolution-driven convection in a Hele–Shaw cell. *Physics of Fluids (1994-present)*, 25(2):024101.

Slim, A. C. and Ramakrishnan, T. (2010). Onset and cessation of time-dependent, dissolution-driven convection in porous media. *Physics of Fluids (1994-present)*, 22(12):124103.

Szulczewski, M., Hesse, M., and Juanes, R. (2013). Carbon dioxide dissolution in structural and stratigraphic traps. *Journal of Fluid Mechanics*, 736:287–315.

van der Poel, E. P., Verzicco, R., Grossmann, S., and Lohse, D. (2015). Plume emission statistics in turbulent Rayleigh–Bénard convection. *Journal of Fluid Mechanics*, 772:5–15.

Weir, G. J., White, S. P., and Kissling, W. M. (1996). Reservoir storage and containment of greenhouse gases. *Transport in porous media*, 23(1):37–60.

Wen, B., Chini, G. P., Dianati, N., and Doering, C. R. (2013). Computational approaches to aspect-ratio-dependent upper bounds and heat flux in porous medium convection. *Physics Letters A*, 377(41):2931–2938.

Wen, B., Dianati, N., Lunasin, E., Chini, G. P., and Doering, C. R. (2012). New upper bounds and reduced dynamical modeling for Rayleigh–Bénard convection in a fluid saturated porous layer. *Communications in Nonlinear Science and Numerical Simulation*, 17(5):2191–2199.

Whitaker, S. (1998). *The method of volume averaging*, volume 13. Springer Science & Business Media.

Wooding, R. A. (1969). Growth of fingers at an unstable diffusing interface in a porous medium or Hele-Shaw cell. *Journal of Fluid Mechanics*, 39(03):477–495.

Wylock, C., Pradas, M., Haut, B., Colinet, P., and Kalliadasis, S. (2012). Disorder-induced hysteresis and nonlocality of contact line motion in chemically heterogeneous microchannels. *Physics of Fluids (1994-present)*, 24(3):032108.

Xu, X., Chen, S., and Zhang, D. (2006). Convective stability analysis of the long-term storage of carbon dioxide in deep saline aquifers. *Advances in Water Resources*, 29(3):397–407.

Yue, P., Feng, J. J., Liu, C., and Shen, J. (2004). A diffuse-interface method for simulating two-phase flows of complex fluids. *Journal of Fluid Mechanics*, 515:293–317.

Zimmerman, W. and Homsy, G. (1991). Nonlinear viscous fingering in miscible displacement with anisotropic dispersion. *Physics of Fluids A: Fluid Dynamics (1989-1993)*, 3(8):1859–1872.